REPORT DOCUMENTATION PAGE

Form Approved
OMB No. 0704-0188

1. REPORT DATE *(DD-MM-YYYY)*	**2. REPORT TYPE**	**3. DATES COVERED** *(From - To)*
21-05-2010	Thesis for Master of Science Degree	

4. TITLE AND SUBTITLE

Measurements versus Predictions for a Hybrid (Hydrostatic Plus Hydrodynamic) Thrust Bearing for a Range of Orifice Diameters

5a. CONTRACT NUMBER
FA9300-04-C-0016

5b. GRANT NUMBER

5c. PROGRAM ELEMENT NUMBER

6. AUTHOR(S)
Paul Robert Esser (Texas A&M University/Northrop Grumman)

5d. PROJECT NUMBER

5e. TASK NUMBER

5f. WORK UNIT NUMBER
502603BY

7. PERFORMING ORGANIZATION NAME(S) AND ADDRESS(ES)

Northrop Grumman
One Space Park
Redondo Beach CA 90278

8. PERFORMING ORGANIZATION REPORT NUMBER

AFRL-RZ-ED-TP-2010-263

9. SPONSORING / MONITORING AGENCY NAME(S) AND ADDRESS(ES)

Air Force Research Laboratory (AFMC)
AFRL/RZS
5 Pollux Drive
Edwards AFB CA 93524-7048

10. SPONSOR/MONITOR'S ACRONYM(S)

11. SPONSOR/MONITOR'S NUMBER(S)
AFRL-RZ-ED-TP-2010-263

12. DISTRIBUTION / AVAILABILITY STATEMENT

Approved for public release; distribution unlimited (PA #10270).

13. SUPPLEMENTARY NOTES
For submission to Texas A&M University.

14. ABSTRACT

A fixed geometry hybrid thrust bearing is investigated with three different supply orifice diameters. The test rig uses a face-to-face thrust bearing design, with the test bearing acting as the rotor loading mechanism. A hydraulic shaker applies the static axial load, which is reacted by a second thrust bearing. The rotor is supported radially by two water-lubricated fluid film journal bearings and is attached to a 30,600 rpm motor via a high speed coupling with very low axial stiffness. Thrust bearings with three different orifice diameters (1.63, 1.80, and 1.93 mm) are tested for a range of supply pressures, fluid film thicknesses, and rotational speeds. The water-lubricated test bearings have eight pockets, with feed orifices located centrally in each pocket. Comparisons are presented for the experimental results to predictions found using bulk flow model HYDROTHRUST®. Analysis of the data reveals generally good agreements between predictions and measurements. Thrust-bearing inlet supply and inner radius flow rates all decreased with decreasing orifice diameters and bearing axial clearances. In most cases, the bearings with larger orifice diameters exhibit higher recess pressure ratios, operating clearances, and flow rates. The largest orifice bearing does not display higher recess pressure ratios or operating clearances at high speeds for some supply pressures, but it does continue to require additional lubricant flow rate compared to the smaller orifice bearings.

15. SUBJECT TERMS

16. SECURITY CLASSIFICATION OF:			**17. LIMITATION OF ABSTRACT**	**18. NUMBER OF PAGES**	**19a. NAME OF RESPONSIBLE PERSON**
					Mr. Alan Sutton
a. REPORT	**b. ABSTRACT**	**c. THIS PAGE**			**19b. TELEPHONE NUMBER** *(include area code)*
Unclassified	**Unclassified**	**Unclassified**	SAR	120	N/A

MEASUREMENTS VERSUS PREDICTIONS FOR A HYBRID (HYDROSTATIC PLUS HYDRODYNAMIC) THRUST BEARING FOR A RANGE OF ORIFICE DIAMETERS

A Thesis

by

PAUL ROBERT ESSER

Submitted to the Office of Graduate Studies of
Texas A&M University
in partial fulfillment of the requirements for the degree of

MASTER OF SCIENCE

May 2010

Major Subject: Mechanical Engineering

MEASUREMENTS VERSUS PREDICTIONS FOR A HYBRID (HYDROSTATIC PLUS HYDRODYNAMIC) THRUST BEARING FOR A RANGE OF ORIFICE DIAMETERS

A Thesis

by

PAUL ROBERT ESSER

Submitted to the Office of Graduate Studies of
Texas A&M University
in partial fulfillment of the requirements for the degree of

MASTER OF SCIENCE

Approved by:

Chair of Committee,	Dara W. Childs
Committee Members,	Gerald Morrison
	James R. Morgan
Head of Department,	Dennis L. O'Neal

May 2010

Major Subject: Mechanical Engineering

ABSTRACT

Measurements versus Predictions for a Hybrid (Hydrostatic plus Hydrodynamic) Thrust Bearing for a Range of Orifice Diameters (May 2010)

Paul R. Esser, B. S., Texas Christian University

Chair of Advisory Committee: Dr. Dara W. Childs

A fixed geometry hybrid thrust bearing is investigated with three different supply orifice diameters. The test rig uses a face-to-face thrust bearing design, with the test bearing acting as the rotor loading mechanism. A hydraulic shaker applies the static axial load, which is reacted by a second thrust bearing. The rotor is supported radially by two water-lubricated fluid film journal bearings and is attached to a 30,600 rpm motor via a high speed coupling with very low axial stiffness. Thrust bearings with three different orifice diameters (1.63, 1.80, and 1.93 mm) are tested for a range of supply pressures, fluid film thicknesses, and rotational speeds. The water-lubricated test bearings have eight pockets, with feed orifices located centrally in each pocket. Comparisons are presented for the experimental results to predictions found using bulk flow model HYDROTHRUST®.

Analysis of the data reveals generally good agreements between predictions and measurements. Thrust-bearing inlet supply and inner radius flow rates all decreased with decreasing orifice diameters and bearing axial clearances. In most cases, the bearings with larger orifice diameters exhibit higher recess pressure ratios, operating

clearances, and flow rates. The largest orifice bearing does not display higher recess pressure ratios or operating clearances at high speeds for some supply pressures, but it does continue to require additional lubricant flow rate compared to the smaller orifice bearings. In these cases, the results are not reflected in predictions, which otherwise correlate very well with experimental measurements. Estimations of static loading axial stiffness are obtained using experimental results.

DEDICATION

To my family, who have always supported me.

ACKNOWLEDGEMENTS

I would like to thank my committee chair Dr. Childs for providing me with the opportunity to work on this project, and for is continued guidance and support over the course of this research.

Thanks also to Mike Forsberg and Fernando Ramirez for their prior effort on the test rig. I also thank David Klooster, Scott Wilson, and the rest of my coworkers at the Turbomachinery Laboratory. I would also like to thank Stephen Phillips and Eddie Denk for all the support and assistance.

Finally, I would like to thank my parents for their love and ongoing patience.

NOMENCLATURE

A_0	Orifice cross-sectional area	[mm^2]
C_d	Orifice discharge coefficient	
D_o	Orifice diameter	[mm]
$E_{dF/dZ}$	Overall uncertainty	
E_N	Uncertainty associated with term "N"	
F_z	Load on the bearing face	[N]
K_{mn}	Stiffness coefficient for "m" direction from the "n" variable	[$^{N}/_{m}$]
M_1	Thrust bearing horizontal misalignment	[$^{mm}/_{mm}$]
M_2	Thrust bearing vertical misalignment	[$^{mm}/_{mm}$]
P_e, P_r, P_s	Exhaust, recess, and supply pressures	[bar]
p_{ratio}	Recess pressure ratio	
Q_0	Flow rate through an orifice	[LPM]
V_o	Fluid velocity through the orifice	[m/s]
Z_1, Z_2, Z_3	Gap reading from proximity probes 1, 2, and 3, respectively	[mm]
z	Thrust bearing clearance	
Φ_b	Misalignment angle about axis "b"	[radians]
ρ	Fluid density	[kg/m^3]
μ	Fluid dynamic viscosity	[$N*s/m^3$]

TABLE OF CONTENTS

Page

LIST OF FIGURES

LIST OF TABLES

Page

1. INTRODUCTION

Hybrid (combination hydrostatic and hydrodynamic) bearings are of particular interest in high speed cryogenic turbomachinery. These bearings utilize externally pressurized process fluids to develop reaction loads. Radial hybrid bearings provide exceedingly low wear and no DN (diameter times speed) life limit, high direct stiffness and damping coefficients, and accurate rotor position control. These features allow for smaller, lighter, and lower part count turbomachines with increased efficiency [1], [2], [3].

Hydrostatic bearings rely on externally pressurized fluid for load capacity. This pressurized fluid flows first into an annulus at the back of the bearing before passing through an orifice into a pocket or recess on the bearing face. From the recesses, the fluid flows over the land regions to the edges of the bearing, where it exits to a lower ambient pressure. The orifice restrictor causes a pressure drop, which leads to a pressure ratio between the recess and the supply. The pressure developed in the recesses generates the force to counteract an applied load. For a thrust bearing, the reaction force is in the direction of the rotor's longitudinal axis. When the rotor is rotating, the bearing performance parameters may alter due to the hydrodynamic effects of the rotating fluid, especially at high rotational speeds. Therefore a bearing with significant rotational effects is referred to as a hybrid bearing due to the need to include both the hydrostatic and hydrodynamic effects for analysis and performance predictions. Thrust bearing

---

This thesis follows the style of *ASME Journal of Tribology*.

performance is dependent on the size, number, and geometry of the recesses, the land area, supply orifices, bearing clearance, fluid properties, fluid supply pressure, and the rotational speed of the rotor. The test thrust bearing used here is depicted in Figure 1.

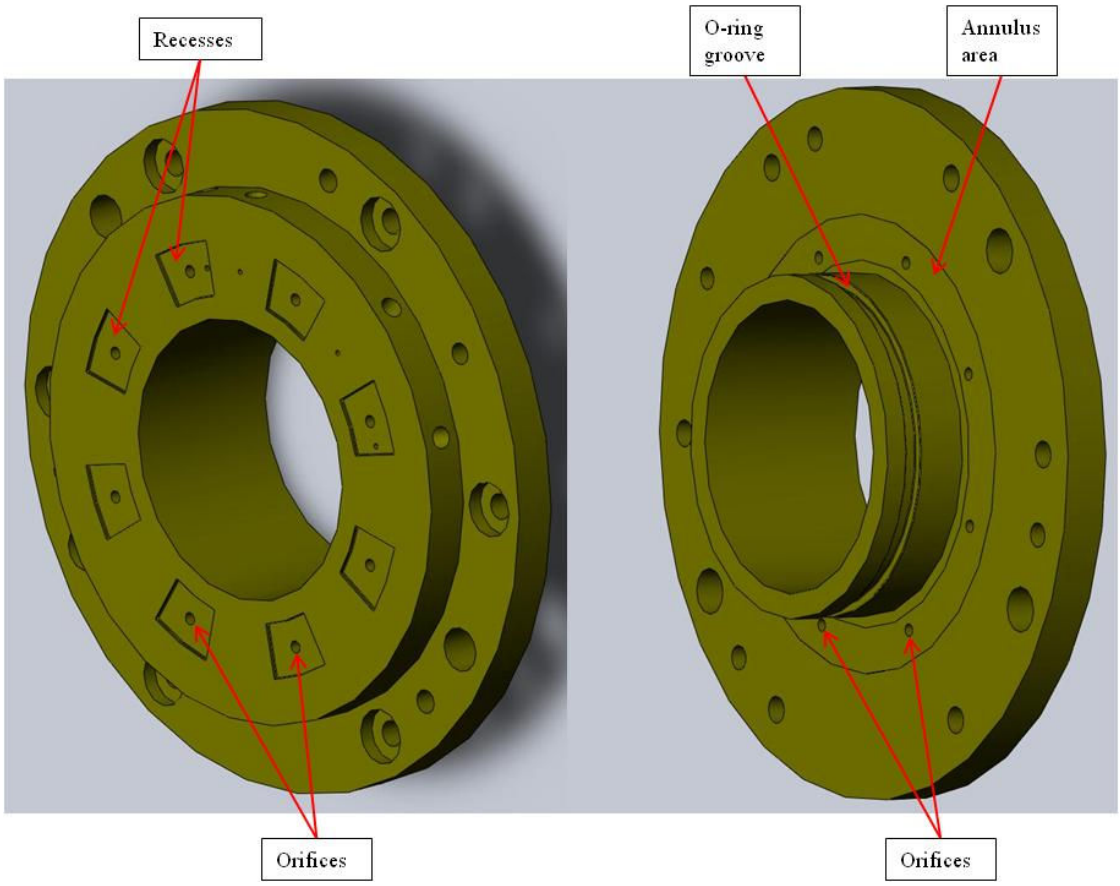

Figure 1: Test thrust bearing front and back

Hybrid bearing performance also depends on the recess pressure ratio P_{ratio} defined as the ratio of recess pressure to supply pressure at a given clearance,

$$P_{ratio} = \frac{p_r - p_e}{p_s - p_e}, \quad (1)$$

where p_e, p_r, and p_s are the exhaust, recess, and supply pressures, respectively. Sparse experimental data exists for hybrid thrust bearings and verification of analytical predictions. Mosher and Childs [4] investigated the effects of pressure ratio on the performance of a hybrid journal bearing for high speed, high pressure applications including theory and experimental data. The authors point out differences in optimum concentric recess pressure ratios in theory and experiments and from the typical value (~0.5 for radial bearings). To date, no such investigation exists for hybrid thrust bearings. This research comprises an experimental investigation of the influence of orifice diameters on recess pressure ratio and the performance parameters of orifice-compensated, water-lubricated, hybrid thrust bearings. Comparisons of measured results are made at varying rotational speeds, supply pressures, and axial clearances using a thrust bearing with three different orifice diameters.

2. PREVIOUS THURST BEARING TEST RIGS AND RESEARCH

Fluid film thrust bearings are not a new area of study in turbomachinery, but hybrid thrust bearings have had much more limited research, especially experimentally. Significant theoretical advancements have been made by a number of authors. The effects of centrifugal fluid inertia in hydrodynamic bearings are studied by Pinkus and Lund [5] and Hashimoto [6]. Additionally, Safar [7] provides a modified Reynolds number analysis on hydrostatic thrust bearing performance parameters including the effects of tilt. Finally, San Andrés [2] presents a computational bulk flow model, HYDROTHRUST®, as a predictive tool for hybrid thrust bearing performance that includes fluid inertia, flow turbulence, and fluid compressibility. Predictions from this tool showed the possibility of "starvation" at high rotational speeds in hybrid thrust bearings due to large centrifugal fluid inertial forces of the fluid causing sub-ambient pressures at the inner radius of the thrust bearing. This outcome could result in a loss in load capacity and subsequent collapse of the bearing. San Andrés [3] further expands this study to include the effects of misalignment, which most notably impacts flow rate, damping, and stiffness.

Thrust bearing test rigs described in the literature are categorized by two types: single thrust bearing test rigs with the load applied by moving the rotor against a stationary thrust bearing, and multiple thrust bearing test rigs where a thrust bearing is used as loading device and is reacted by a second bearing. Most test rigs involving

rotation cite a two-thrust-bearing test rig design, though the test bearings are generally hydrodynamic tilting pad type with mineral oil used as the lubricant. New [8] uses a test rig of this type, implementing a hydrostatic thrust bearing as the loading device, and Gregory [9], Neal [10], Horner et al. [11] describe similar rigs.

Harada et al. [12] present a multiple-thrust-bearing design, again using a hydrostatic thrust bearing as the loading device. The Harada test rig implements gas bearings to support the loading shaft and bearing with ball bearings used to react the load. The authors also use three eddy current proximity probes located 120° apart on the test thrust bearing for detailed clearance measurements. Wang and Yamaguchi [13] use a similar hydrostatic thrust bearing test rig with a hydraulic loading mechanism and an additional thrust bearing to transfer the load to the test bearing to prevent misalignment and allow accurate torque measurements.

Gardner [14] and Glavatskih [15] use similar back-to-back style thrust bearing rigs which have thrust collars located on the outside of the thrust bearings. Glavatskih also utilizes the test thrust bearing as the loading device via hydraulic loading pistons. The load is then transmitted through the rotor before being reacted by the second bearing. These test rigs also provided hydrostatic support to allow for torque measurements on the test thrust bearing with the use of a load cell. Forsberg [16] and Ramirez [17] used the test rig employed in this study and provide further detailed descriptions of prior thrust bearing test rigs.

3. TEST RIG DESCRIPTION AND INSTRUMENTATION

This research takes advantage of a preexisting test rig described in detail by Forsberg [16] and Ramirez [17]. The thrust bearing test rig is the identical structure and configuration described by Ramirez.

3.1 Rig Description

Figure 2 shows a schematic of the test rig, which is similar in layout to the back-to-back designs of Gardner [14] and Glavatiskih [15], but locates the thrust bearings on the outside of the rotor thrust collars. This face-to-face configuration allows a single-piece test thrust bearing design rather than split type and reduces the weight of the loading mechanism. On the non-drive-end of the test rig, a hydraulic loading cylinder generates the static load and is connected to the test thrust bearing via a shaft supported on two hydrostatic air bearings. The test bearing is then used to load the rotor axially, transmitting the load along its length before equally loading the opposing thrust bearing (slave bearing). The slave bearing reacts the applied load and is located at the drive end of the rotor housing, opposite from the test bearing. The test rig load path is illustrated in Figure 3. High pressure water is supplied from a single 6.89 MPa (1000 psig) pump to both journal bearings, slave thrust bearing, and test thrust bearing. Independent control valves individually throttle and control flow rates to each of the three sections.

An electric motor drives the rotor through a FLEXXOR® coupling at the slave thrust bearing end of the test rig.

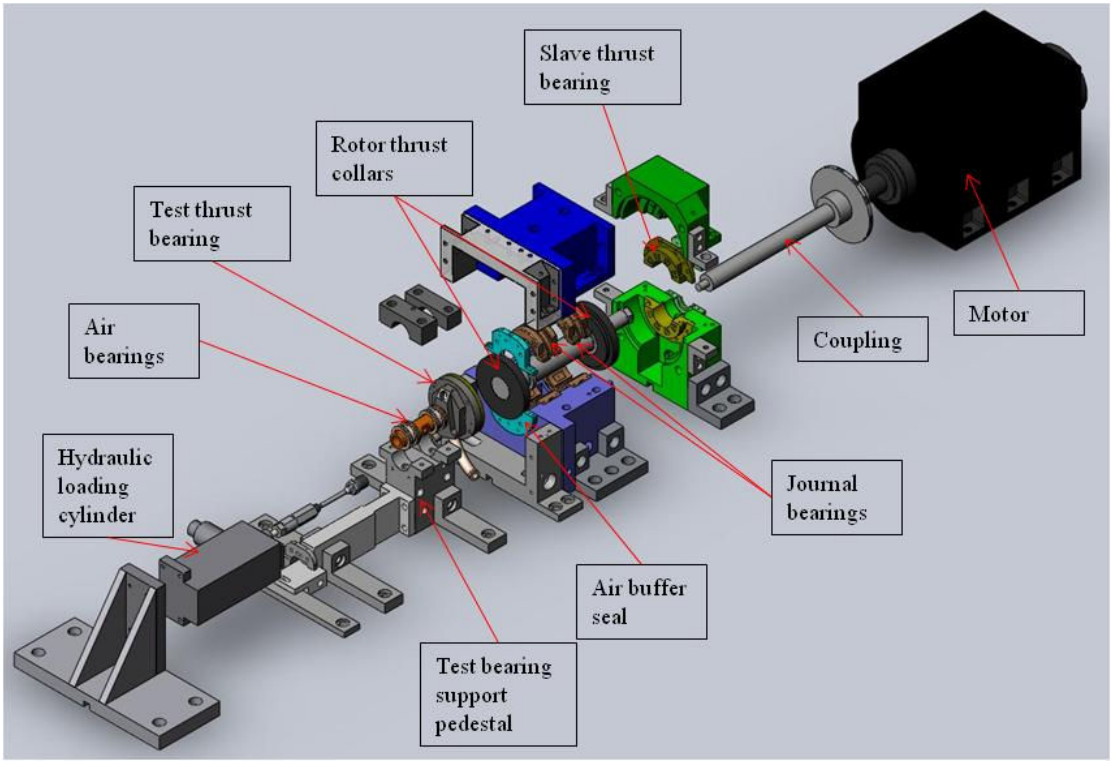

Figure 2: Test rig schematic

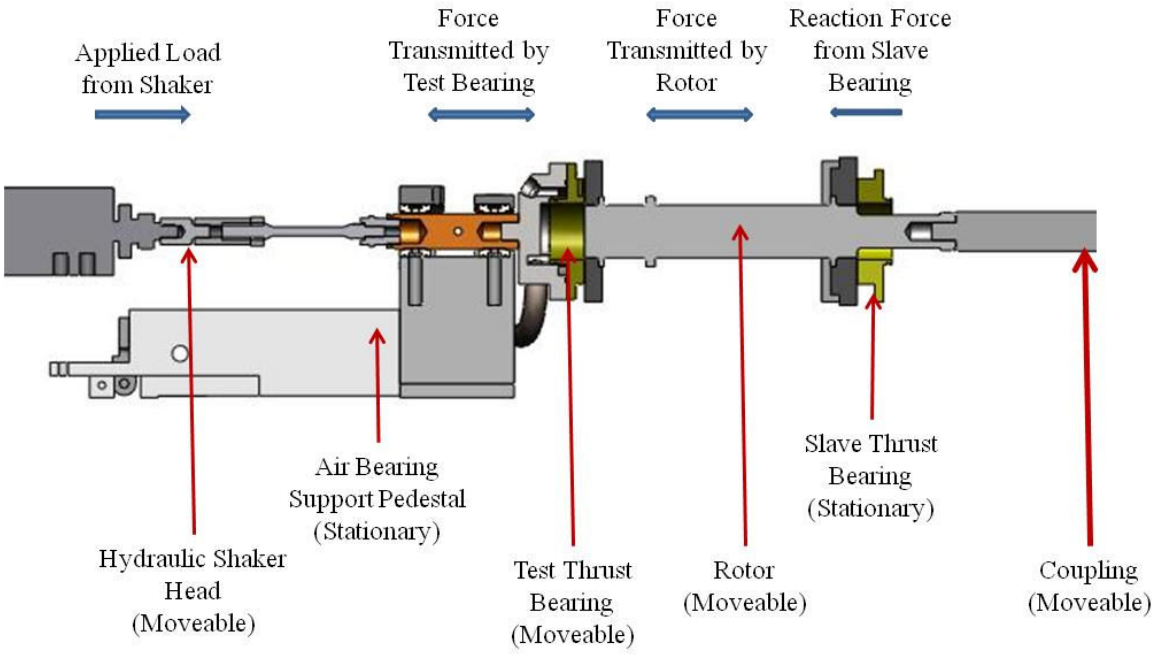

Figure 3: Test rig load path

The loading mechanism comprises a hydraulic loading cylinder connected to a shaft that is supported on two hydrostatic journal bearings. These aerostatic bearings are supplied with filtered 10.34 bar (shop) air. The test thrust bearing is then attached to the end of the support shaft opposite the hydraulic cylinder. This design allows free axial travel and rotation of the loading shaft, which provide accurate applied load measurements to the test thrust bearing. A moment arm attached to the support shaft between the air bearings acts on a strain gage load cell to allow measurement of test bearing frictional torque. The entire support is mounted on a pedestal that is designed to allow for horizontal adjustments of thrust bearing alignment to the rotor thrust face through the use of a micrometer and setscrew positioned on either side of the keyway in the test rig base. Figure 4 provides a detail view of the support pedestal with the

hydraulic loader disconnected to show alignment adjusters and the load cell used for torque measurements.

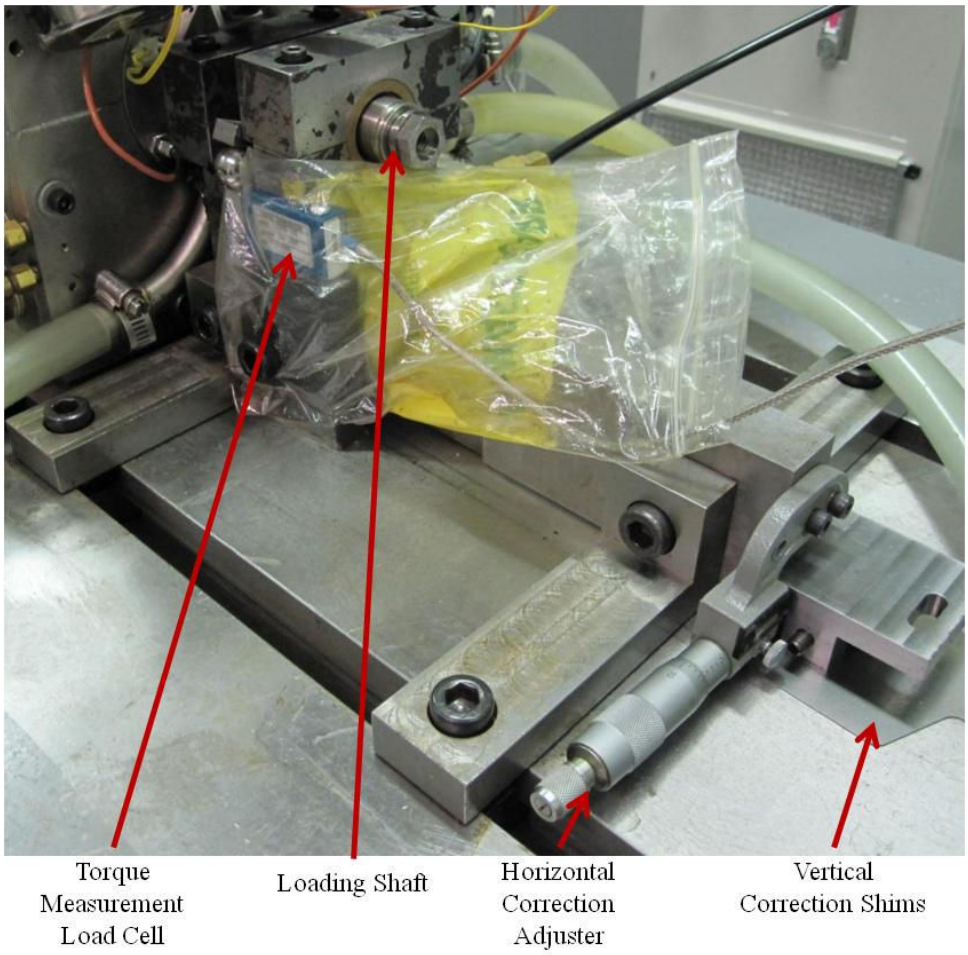

Figure 4: Test thrust bearing support pedestal and loading shaft

Test thrust bearing air seals and water flow paths are shown in Figure 5. Water is supplied to the top of an annulus at the back of the test thrust bearing before flowing through orifices and into the recesses. The water then flows radially across the land region of the bearing face to either the inner or outer radius where it is discharged. A

pneumatic control valve provides precise control of the flow of water into the test bearing.

The large air seal isolates water in the test thrust bearing housing by preventing leakage contamination from the journal bearing section of the test rig. Additionally, the main air buffer seal prevents leakage out of the test rig from around the outer radius of the test bearing. This isolation ensures proper test lubricant measurements. A similar air buffer seal is located on the rotor shaft at the drive end of the test rig to prevent water leakage from the slave bearing.

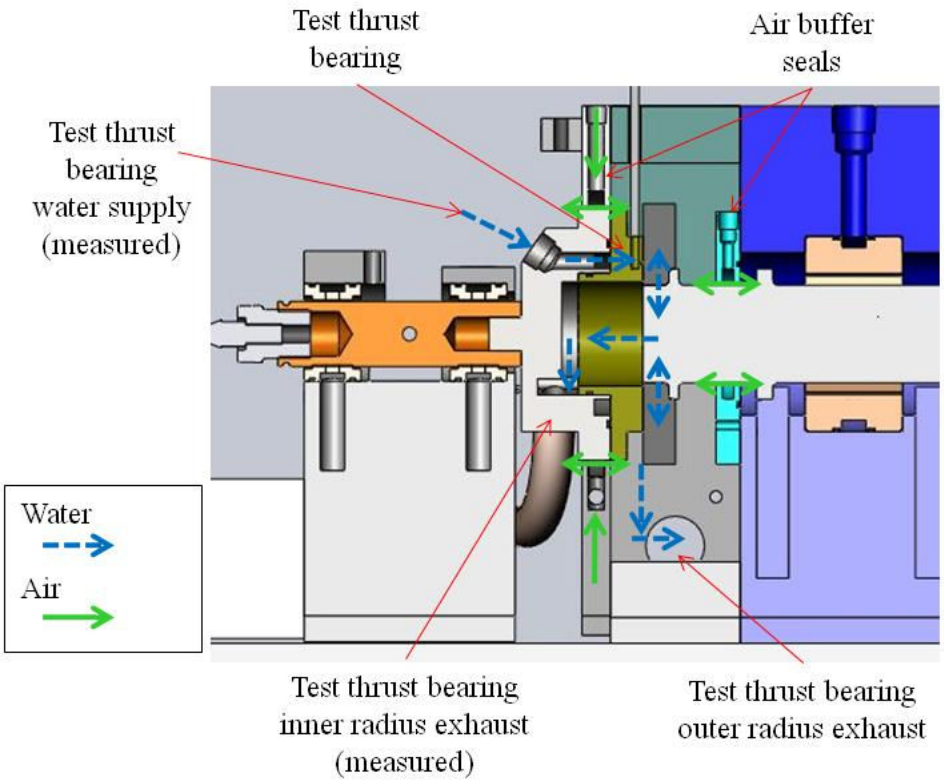

Figure 5: Test thrust bearing water and air flow

In this research, an eight pocket orifice-compensated thrust bearing is tested. The only bearing parameter changed is the orifice diameters, which are varied to investigate the effects on hybrid thrust bearing performance. The bearing measures 76.2 mm (3 in) at the outer diameter and has an inner diameter of 40.64 mm (1 in). Additional relevant thrust bearing parameters are shown in Table 1.

The rotor is 268.30 mm (10.56 in) in length and is supported radially by two flexure-pivot-pad type hybrid journal bearings spaced 63.5 mm (2.5 in) apart between the two thrust collars. The rotor diameter is 38.10 mm (1.5 in) at the journal bearing locations, and the thrust collars are machined to 0.00508 mm (0.0002 in) flatness. The non-drive-end thrust collar is loaded by the test bearing while the drive-end collar loads the slave thrust bearing. The test rotor can be rotated at speeds up to 30,600 rpm via a 22 kW variable frequency drive motor. The motor-to-shaft coupling is a FLEXXOR® element and quill shaft providing very low axial stiffness (3.5 N/mm) in addition to a permissible axial travel of 0.61 to 1.22 mm. These properties allow isolation of the rotor and bearings from the motor to ensure good test measurements.

The slave thrust bearing is identical to the test bearing, with orifice diameters of 1.80 mm, but is a split design. This feature allows for ease of installation due to the rotor passing through the bearing inner radius. The slave bearing also has a different flange design but still provides three proximity probes to monitor the bearing axial clearance.

Table 1: Test thrust bearing dimensions and parameters

Thrust Face	Outer Diameter	76.2 mm (3 in)
	Inner Diameter	40.64 mm (1.6 in)
	Machined Flatness	0.00254 mm (0.0001 in)
Recesses	Number of Recesses	8
	Arc Length	20°
	Depth	5.08 mm (0.020 in)
	Mean Diameter	54.86 mm (2.16 mm)
	Radial Length	8.13 mm (0.32 in)
	Recess/wetted land ratio	0.19
	Recess to land loss coefficient	0.20
Orifices	Diameters (three configurations)	1.63, 1.80, 1.93 mm (0.064, 0.071, 0.0765 in)
One per recess	Radial Location	27.43 (1.08 in)
	Orifice Length	12.7 mm (0.5 in)

3.2 Instrumentation

The thrust bearing test rig is fully instrumented for static measurements. Eddy current proximity probes verify clearance (fluid film thickness) and alignment of the thrust bearing face and rotor thrust collar. Three probes are used for each thrust bearing. The three on the test thrust bearing are displayed in Figure 6, labeled as "Probes." Two additional proximity probes are located radially 90° apart at each rotor thrust collar to monitor radial movement of the rotor and its orbits. Ten proximity probes are used in all, providing exact positioning and alignment of the test thrust bearing and rotor both axially and radially.

Five static pressure transducers are used to monitor lubricant pressure in the test bearing. One transducer measures water inlet pressure at the thrust bearing annulus, two measure pressures in two different recesses, and the final two transducers are used for measurements on the land region. The four pressure measurements on the test thrust bearing face are shown in Figure 6, and are labeled as "Pockets" and "Lands." The holes shown on the bearing face intersect with perpendicular holes drilled radially from the edge of the bearing. The transducers are connected to these pressure taps with flexible tubing. Four additional pressure transducers monitor inlet pressures to the two journal bearings and top and bottom inlet pressures of the split slave thrust bearing.

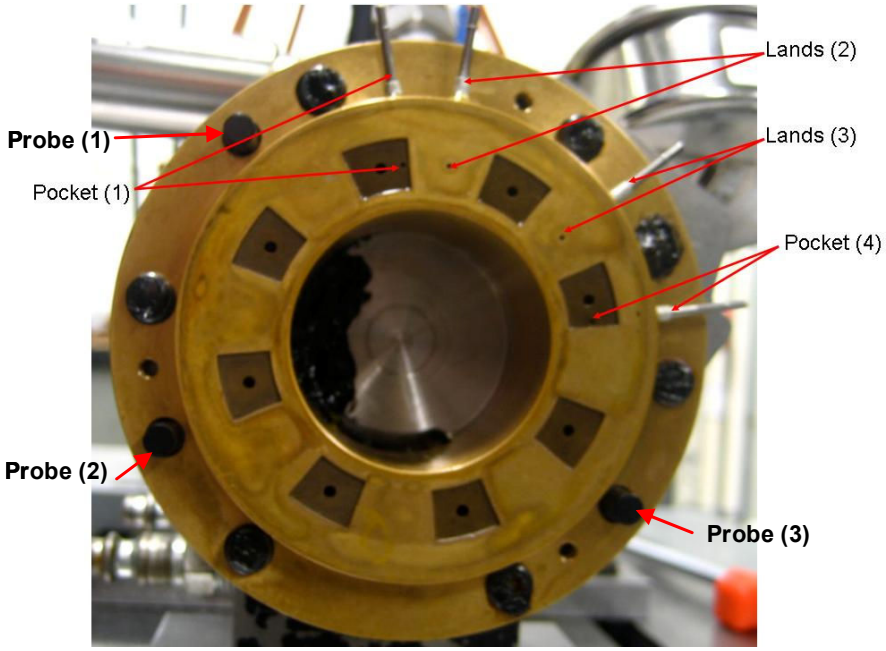

Figure 6: Test thrust bearing instrumentation [16]

Two turbine flow meters monitor the water flow rate into the test bearing and the exhaust flow rate through its inner radius. Two additional turbine flow meters are used for the inlets of the slave thrust bearing and journal bearings. All four flow meter outputs are connected signal linearizers before being wired to the DAQ.

Three plug style type K thermocouples are used for temperature measurements at the test thrust, slave thrust, and journal bearing supply inlets. Two additional type K thermocouples are positioned at the inner and outer radii on the test thrust bearing for exhaust temperature measurements.

Static data collection is achieved using a National Instruments PCI-6225 DAQ board. Sensor outputs are displayed real time using a NI LabVIEW virtual instrument front panel previously used by Forsberg [16] and Ramirez [17]. Included in this front panel view are all proximity probe outputs, load cell, pressure transducer, flow meter, and thermocouple values, as well as the average axial clearance and minimum individual values of the axial proximity probes on the test thrust bearing. A summary of specifications for the PCI-6225 board is supplied in Table 2. The fully instrumented test rig allows precise control and monitoring during operation in addition to allowing quality test thrust bearing performance comparisons. Further details on the sensors and data acquisition system may be found in Appendix C and have been previously documented by Forsberg [16] and Ramirez [17].

Table 2: PCI DAQ board specifications

Board Type	Number of Channels	Sampling Rate [K samples/s]	Resolution [bits]	Signal Range [V]	Signal Type	Connection
PCI-6225	80	250	16	±10	Analog/Digital Input/Output Analog Input Used	2 Pole wire through SCB-68 Connector Block

4. TEST PROCEDURE

Three hybrid thrust bearings with different orifice diameters (1.63, 1.80, and 1.93 mm) were individually tested at statically loaded, steady state conditions at three supply pressures (5.17 bar, 10.34 bar, and 17.24 bar) and four speeds (0 rpm, 7500 rpm, 12,500 rpm, and 17,500 rpm) over a range of axial clearances. Table 3 provides an overview of the test matrix for each bearing.

Table 3: Test conditions

Speed	7500, 12500, 17500 rpm
Supply (Annulus) Pressure	5.17, 10.34, 17.24 bar (75, 150, 250 psi)
Calculated Axial Clearance	0.05 to 0.1 mm (0.002 to 0.004 in)

4.1 Alignment

Thrust bearing face-to-rotor thrust collar alignment is of particular importance due to its influence on thrust bearing performance, but achieving adequate alignment presented difficulties throughout data collection. This problem was resolved vertically by using shims under the test thrust bearing support pedestal and shaker support and horizontally adjusted via micrometer and spring set screw in the thrust bearing support pedestal. Both horizontal and vertical adjustment mechanisms are shown on the thrust bearing support pedestal detailed previously in Figure 4. Shims under the shaker support

ensured a directly horizontal loading action perpendicular to the vertical axis and were set at the beginning of alignment process and were not changed throughout testing.

Misalignment is quantified in this research by describing it as a slope of deviation from parallel over a radial length across the bearing face [$^{mm}/_{mm}$]. Alignment was systematically corrected before each test and checked for discrepancies immediately afterwards. Prior to each test, a baseline is conducted followed by an alignment assessment (both non-rotating). The baseline values of the proximity probes are taken as zero clearance and are subtracted from those found with the bearings pressurized resulting in calculated axial clearance and misalignment figures. Baseline readings are obtained by pressurizing the journal bearings to 17.24 bar to ensure a centered position and applying increasingly high loads to the non-pressurized thrust bearings. Without a fluid film between the thrust bearing faces and rotor thrust collar, the applied load forces flush mating between the two faces. After the baseline is established, an alignment assessment is conducted by pressurizing the thrust bearings to the desired test condition and applying a wide range of loads (exceeding the maximum and minimum for the test).

From the alignment tests, the misalignment across the bearing faces is obtained through evaluation of the three proximity probe values. Forsberg [16] derives Equations (2) and (3) which are used to quantify the misalignment for the test thrust bearing in the horizontal (M_1) and vertical (M_2) directions. These values are subsequently used to find the amount of shim required to correct it. The misalignments are calculated to be

$$M_1 = 0.00194(Z_2 - Z_3)\ [^{mm}/_{mm}] \quad (2)$$

$$M_2 = (-0.00294 * Z_1 + 0.00277 * Z_2 + 0.00017 * Z_3)\ [^{mm}/_{mm}] \quad (3)$$

where Z_1, Z_2, and Z_3 are the gap readings from test thrust bearing proximity probes 1, 2, and 3, respectively. Figure 7 gives an illustration of test thrust bearing misalignment and the proximity probe locations. Details of the derivation of these equations as well as those used for the slave thrust bearing misalignment are provided by Forsberg [16] and Ramirez [17].

Alignment corrections are then conducted in both the vertical and horizontal directions. In the vertical direction, shims are added or removed from the thrust bearing support pedestal while the micrometer adjuster allows misalignment correction in the horizontal direction. In both cases, the required adjustment is obtained by multiplying the previously obtained M_1 and M_2 values by the length of the test thrust bearing support pedestal. This process is repeated until the maximum misalignment of the thrust faces to the rotor thrust collars in both horizontal and vertical directions are less than or equal to 0.013 mm, and has been verified by a second test.

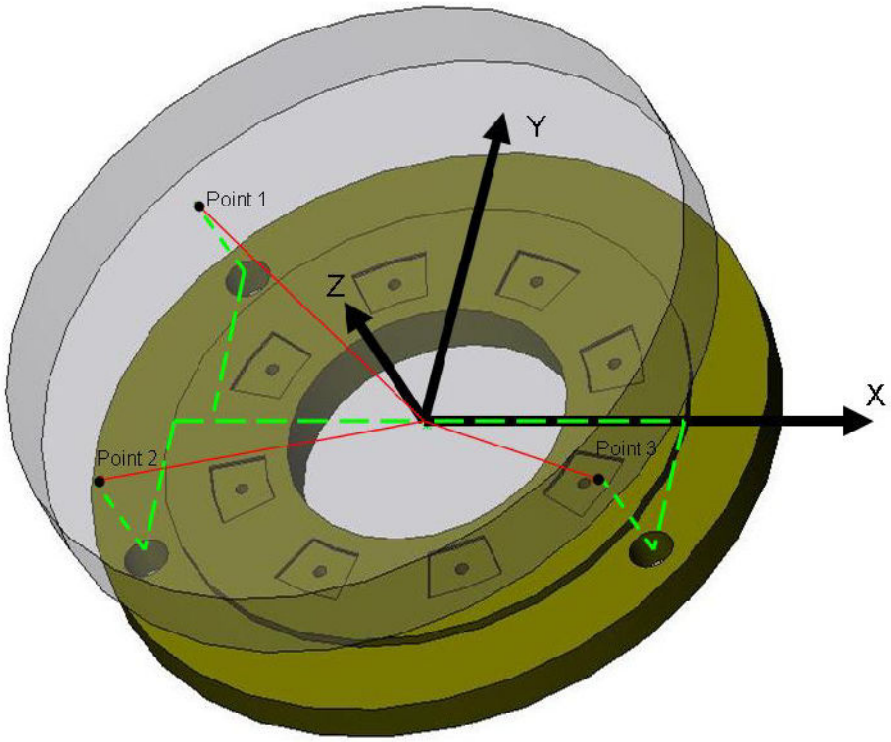

Figure 7: Misalignment illustration and proximity probe locations on the test thrust bearing [16]

4.2 Test Procedure

The hydraulic shaker is used to apply the axial load through the test thrust bearing and can be controlled by two possible internal control loops or by an external reference. During a baseline test or alignment assessment, an internal control loop utilizing the load cell mounted in the shaker head is utilized. This "load control" configuration allows testing at specific applied loads without regard to the clearance

between the test thrust bearing and rotor collar, therefore allowing a wide range of loads including a zero clearance or mated condition required for a baseline.

Alternatively, the shaker can be placed in stroke control mode, which references the length that the cylinder's actuator is extended, instead of the applied load. This configuration also allows an external reference instead of the internal monitoring of the actuator. During regular testing, an axial proximity probe on the test thrust bearing is used as the external reference, which enables the operator to set and maintain a given clearance between the test thrust bearing and the rotor thrust collar. This "displacement control" configuration not only aids in setting precise test conditions, but additionally acts as a safety measure in the case of thrust bearing fluid film collapse under high applied loads.

Under normal test conditions, the journal bearings are initially pressurized to 17.24 bar, while the thrust bearings are pressurized to the desired condition and held constant. A relatively large displacement is then set between the test thrust bearing and the rotor thrust collar using the hydraulic shaker controller in "displacement control." A minimum-load steady-state condition is confirmed by ensuring a minimum (and constant) P_{ratio} of 0.1 and that the shaker maintains a constant load via real time data displays. Testing would then commence for the zero speed case, incrementally decreasing the displacement to a minimum at 50.8 μm while adjusting the thrust bearing supply pressures to keep them constant for the entire test. This process is then repeated at three constant rotational speeds and for all three supply pressures. Outputs of all

sensors are recorded with the data acquisition system with 20 readings for each case. Uncertainty calculations for measured data are shown in Appendix B.

5. TEST RESULTS AND PREDICTIONS

This research aims to investigate the results of varying orifice diameters on the performance of fixed geometry, water-lubricated hybrid thrust bearings. Bearing parameters of particular interest are recess pressure ratio, operating clearances, inlet and exhaust flow rates, and static axial stiffness. The following sections show results for a bearing with three different orifice diameters tested at a number of test conditions versus predictions. Optimum thrust bearing features include larger minimum film thickness for an applied load, reduced flow rates, and larger axial stiffness with a stable positive stiffness across the expected range of axial clearances. Tests are conducted to show how these variables change as the recess pressure ratio is changed.

Some data presented are for a bearing with an orifice diameter of 1.80 mm, which was presented by Forsberg [16] for non-rotating cases and Ramirez [17] for cases with the rotor spinning. These data were obtained using the same test rig as the present analysis, and a number of test cases of their results were repeated by the author with very good agreement. Therefore, their prior work is reproduced here with confidence and provides the third orifice size for comparisons.

Forsberg and Ramirez provide test data for the test bearing with the 1.80 mm orifice diameter at supply pressures of 3.45, 10.34, and 17.24 bar. However, the two new orifice diameters (1.63 and 1.93 mm) of the test bearing were tested at supply pressures of 5.17, 10.34, and 17.24 bar. This change of the lowest supply pressure from 3.45 to 5.17 was due to difficulties experienced maintaining bearing clearances (fluid

film thickness) at that lowest pressure. Comparisons are consequently presented for only the 1.63 mm and 1.93 mm orifice diameter bearings at the 5.17 bar supply pressure.

All test parameters are functions of fluid properties, operating (rotational) speed, supply pressure, and applied load. Experimental data are compared to show both the influence of orifice diameters on bearing performance parameters and the accuracy of HYDROTHRUST® predictions. Comparisons are made at all three rotational speeds and varying supply pressures. Note that the non-equal differences between the orifice diameter values are due to size limitations of the drill bits used to make the orifices.

HYDROTHRUST® requires physical properties and test conditions as well as relaxation and loss coefficients for analysis. Input parameters include bearing geometry (bearing face inner and outer diameters, axial clearance, surface roughness, land and recess dimensions, number of recesses, and orifice diameters), thrust collar rotational speed, bearing face static misalignment, fluid properties, fluid supply and exit pressures, entrance loss and orifice discharge coefficients, and solution convergence factors. The values used for these additional input parameters used for the predictions presented are given in Table 4.

Table 4: Input parameters used for HYDROTHRUST® predictions

Max Iterations - film lands	99	Frequency Analysis Type:	Synchronous
Momentum Relaxation Factor	0.8	Thermal Analysis Option:	Isothermal fluid film
Pressure Relaxation Factor	0.5	Analysis Type:	Fixed Clearance
Temperature Relaxation Factor	0.9		
		CONVERGENCE	
Collar Relative Roughness	0.001	PARAMETERS	error criteria
Stator Relative Roughness	0.001	Pressure film lands	0.0001
Moody's Coef Amod	0.001375	Pressure recess	0.01
Moody's Coef Bmod	500000	Mass flow - lands	0.01
Moody's Coef Expo	0.3333	Mass flow - recesses	0.006
No. of Grid Points per Pocket		Supply Temperature	43° C
No. Circ. Grid Points	9	Fluid	Water
No. Radial Grid Points	5		

The orifice discharge coefficient, C_d, is required as an input in HYDROTHRUST® predictions and is used to model the pressure drop from the supply pressure to the recess pressure. The orifice discharge coefficients are found utilizing the following equation [3] for turbulent flow through an orifice,

$$C_d = \frac{Q_0}{A_0\sqrt{\frac{2}{\rho}(P_s - P_r)}} \tag{4}$$

Here, Q_0 is the flow rate through an orifice, A_0 is the cross-sectional area of the orifice, and ρ is the fluid density. Additionally, P_s and P_r are the supply and recess pressures, respectively. The use of the above equation assumes equal fluid flow through each of the bearing orifices and equal recess pressures across the bearing face.

For the predictions presented here, estimates of C_d are obtained from the available experimental data. Experimentally determined orifice discharge coefficients are presented in Table 5. Note the decreasing C_d values with decreasing orifice diameter, but relatively constant values over the range of tested supply pressures. C_d values also decrease very slightly with increasing load (decreasing clearance and flow rate) in experimental results for all bearing configurations and test conditions (less than 5% over entire clearance range). The average uncertainty for the obtained C_d values is 1.95%, with an average maximum uncertainty of 3.65%. The predictions use C_d values obtained using this empirical analysis.

Table 5: Average orifice discharge coefficients used for HYDROTHRUST® predictions

Orifice Diameter	Supply Pressure		
	5.17 bar	10.34 bar	17.24 bar
	Average Cd		
1.93 mm	0.648	0.666	0.648
1.80 mm	-	0.599	0.586
1.63 mm	0.555	0.542	0.531

A final input requirement for HYDROTHRUST® is the static misalignment of the thrust bearing face (in radians). These misalignments were found using Equations 2 and 3 for all test conditions. The slopes (in $^{mm}/_{mm}$) from these equations are converted to radians by taking the inverse tangent. Figure 8 shows thrust face misalignment for all three bearing orifice diameters at a supply pressure of 17.24 bar and 17.5 krpm.

Misalignments are presented as an axial distance (a product of the misalignment angle and the outer diameter of the bearing face, 76.2 mm). All tests for this case (and nearly all others) show misalignment within the desired limits of ±0.013 mm, as indicated by the marker lines. Additional misalignment figures are found in Appendix D.

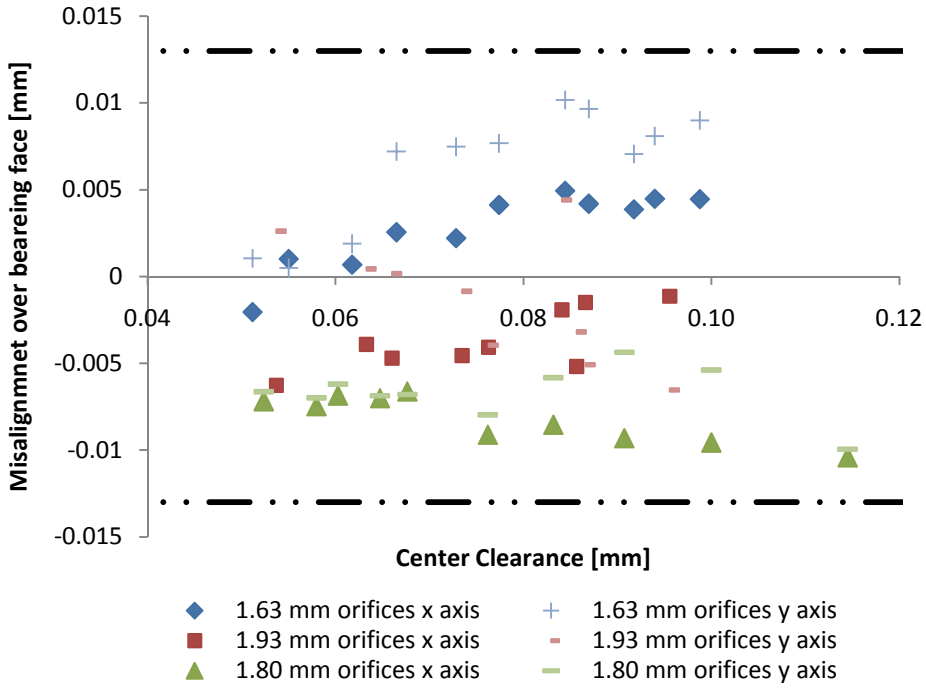

Figure 8: Misalignment over the bearing face about the x and y axis versus center clearance at 17.24 bar and 17.5 krpm. Lines note desired misalignment limits (±0.013 mm)

Relevant comparisons between the various test results and predictions are presented here. Comparisons are made over a range of operating conditions, drawing on the influence of the orifice diameters and the recess pressure ratios on the bearing

parameters. Measurement uncertainties are included on all plots of experimental data in the form of error bars. Percent errors between the experimental data and predictions for all of the results presented are calculated the following equation.

$$\% \, Error = \frac{|Measured \, Value - Predicted \, Value|}{Measured \, Value} * 100 \qquad (5)$$

5.1 Inlet Flow Rate

Bearing inlet flow rate plots are shown in Figure 9 for the 10.34 bar supply pressure case and in Figure 10 for the 17.24 supply pressure case at 7.5 and 12.5 krpm, respectively. The figures display very similar trends when comparing the three orifice diameters, with all three tending toward convergence at the lowest clearances (highest loads). The smaller axial clearance limits the flow rate though the bearing. Inlet flow rate requirements are nearly constant for all three orifice configurations and supply pressures.

Comparisons are also depicted for fluid inlet flow rate predictions in the same figures. Very good agreement is seen in Figure 9 between measurements and predictions for both the 1.80 mm and 1.93 mm orifice diameter bearings, while the smaller, 1.63 mm orifice diameter bearing predictions show a larger error. Note the best agreement is achieved at the lower clearances (high applied loads) for all three orifice diameter configurations and test conditions. Similar results are displayed in Figure 9, with

slightly better agreement for the 1.93 mm orifice diameter case. The maximum average error between measurements and predictions was 17.0% for the 1.63 mm orifice diameter case, but average percent errors lower than 3% are seen for the larger orifice bearings. The 1.80 mm orifice diameter data matches nearly exactly with predictions for both cases, especially at the lowest clearances. The results presented for inlet flow rate show a good representation of the remaining data, and flow rate predictions tend to correlate very well with the measured data.

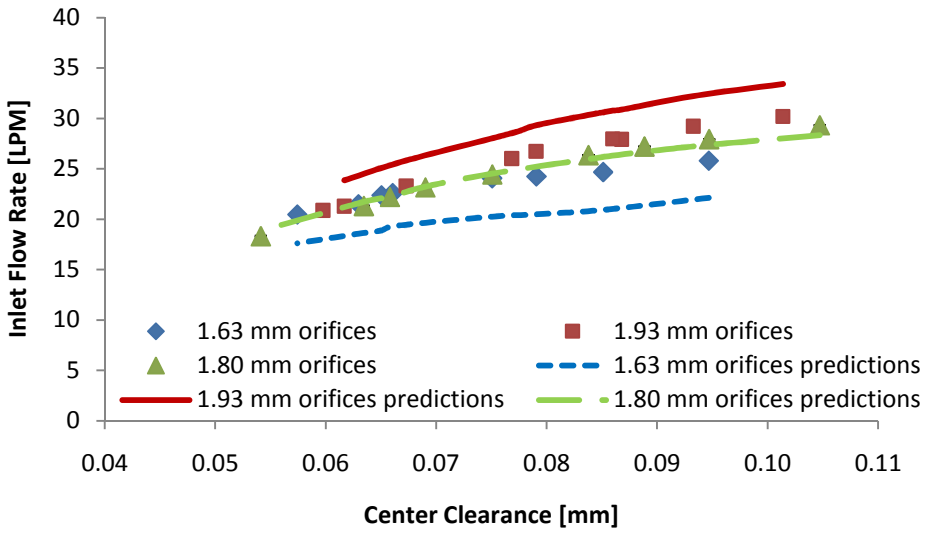

Figure 9: Measured and predicted [3] inlet flow rate versus center clearance at 10.34 bar and 12.5 krpm

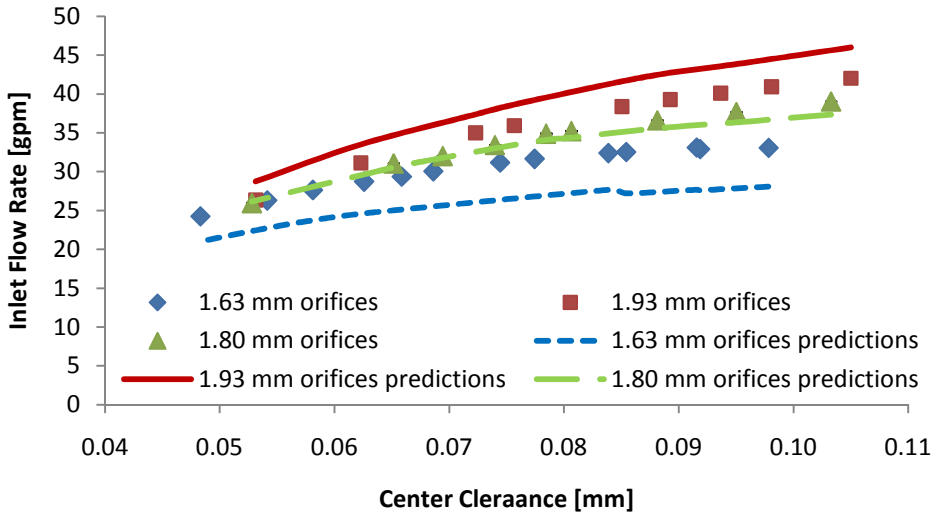

Figure 10: Measured and predicted [3] inlet flow rate versus clearance at 17.24 bar and 7.5 krpm

Figure 11 displays the measured flow rates versus predictions for the lowest (5.17 bar) supply pressure and at the non-rotating condition. Note the particularly good agreement at the lowest clearances for both orifice diameters and near exact match for the 1.93 mm diameter case. These low supply pressure plots consistently reflect excellent correlation with predictions for all rotational speeds, and are significantly improved over the higher supply pressure data.

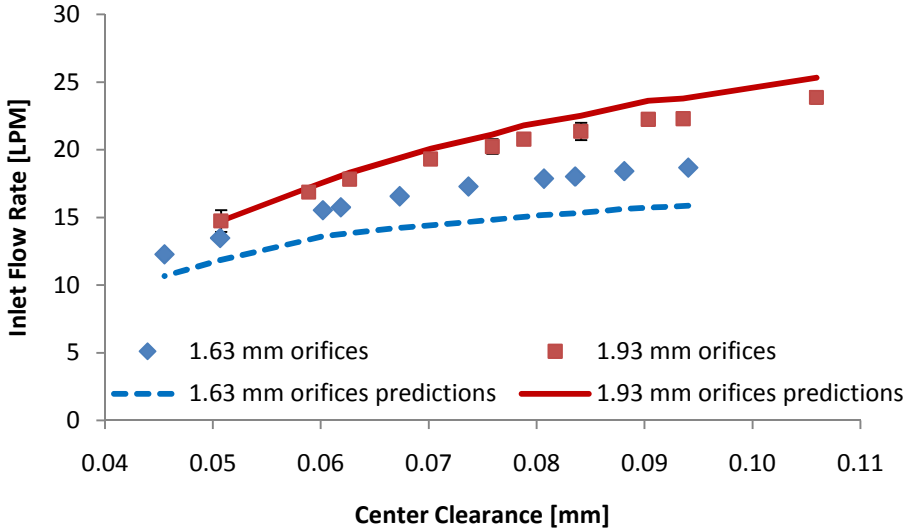

Figure 11: Inlet flow rate versus center clearance at 5.17 bar and 0 rpm

5.2 Recess Pressure Ratio

The following plots display how the various diameters affect the recess pressure ratios for the three supply pressure conditions, found by taking the average of the pressure measurements in the two recesses (pockets) on the bearings for each case. The two measured recess pressures for each bearing were generally in good agreement, which verifies adequate bearing face alignment and uniform flow across the bearing face. Plots presented correspond to the same test conditions as the figures shown with inlet flow rate measurements (Figures 9-11). Figure 12 shows the relationship of the recess pressure ratios between the three bearings for the middle (10.34 bar) supply pressure at 12.5 krpm. This trend is consistent for all speeds at the 10.34 supply pressure

case and for the slowest speeds of the low (5.17 bar) and high (17.24 bar) supply pressures. Note that in Figure 9 the closest agreement between measurements and predictions for inlet flow rates is shown for the 1.80 mm orifice diameter while the 1.63 mm orifice displays the best agreement for recess pressure ratios (Figure 12).

The 17.24 and 5.17 bar supply pressures display similar results to the 10.34 bar case at 7.5 and 0 krpm, as depicted in Figures 13 and 14. Neither plot provides agreements with predictions that match those shown in the inlet flow rate figures at the same test condition given previously (Figures 10 and 11). In fact, while the 1.63 mm orifice diameter provides better agreement than the other two orifice configurations in Figure 13. In contrast, Figure 10 shows better agreement for the larger two orifice configurations with the closest matches occurring at the smallest clearances. The 1.63 mm orifice diameter case again shows the better agreement in Figure 14, but the corresponding inlet flow rate figure shows best agreement with the 1.93 mm orifice diameter.

In general, predictions show reasonable agreement with the recess pressure measurements, especially for the 1.63 mm and 1.80 mm orifice diameter cases. Note that the smallest (1.63 mm) orifice configuration provides best agreement with predictions for the clearance versus recess pressure ratio plots. Recall that for the inlet flow rate figures both the 1.93 mm and 1.80 mm orifice diameters showed better agreement with predictions. Additionally, inlet flow rate plots correlated especially well at the lowest clearances, with the 1.80 mm orifice diameter data providing near exact matches with predictions. The recess pressure ratio data does tend to show notably

better agreement at either low or high clearances, and they do not correspondingly match predictions in the same manner as the inlet flow rate data. There is no obvious correlation between the ability of HYDROTHRUST® to predict inlet flow rates and recess pressures, although adequate results are produced for both.

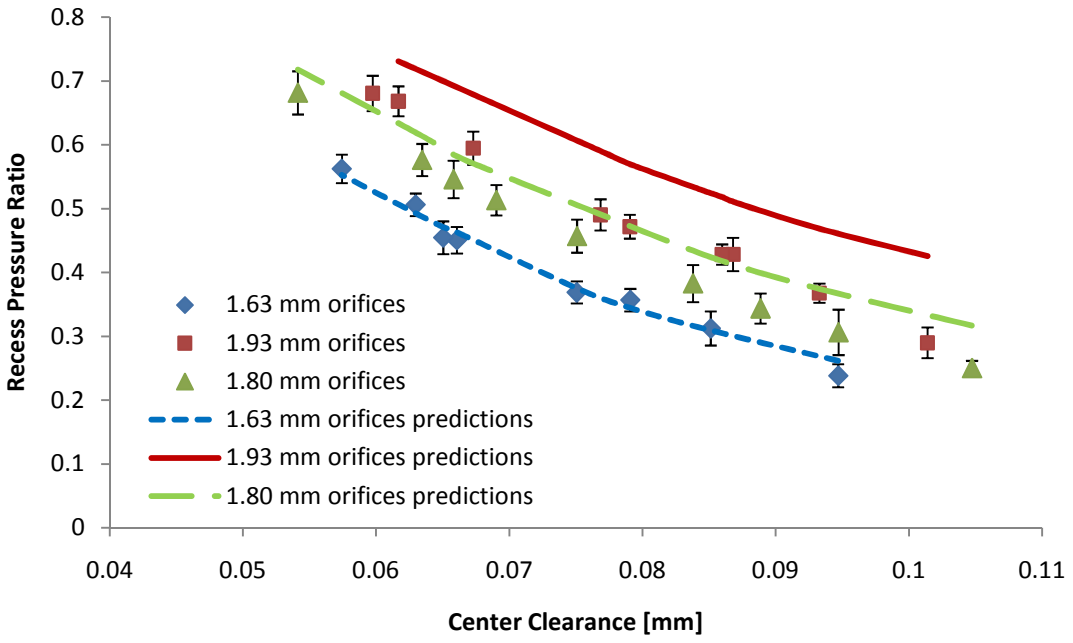

Figure 12: Measured and predicted [3] recess pressure ratio versus clearance at 10.34 bar supply and 12.5 krpm

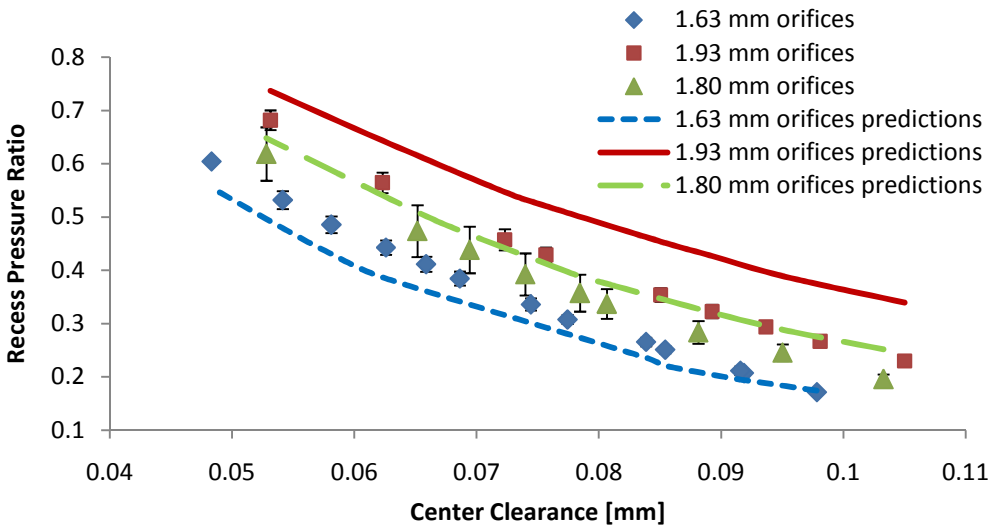

Figure 13: Measured and predicted [3] recess pressure ratio versus clearance at 17.24 bar supply and 7.5 krpm

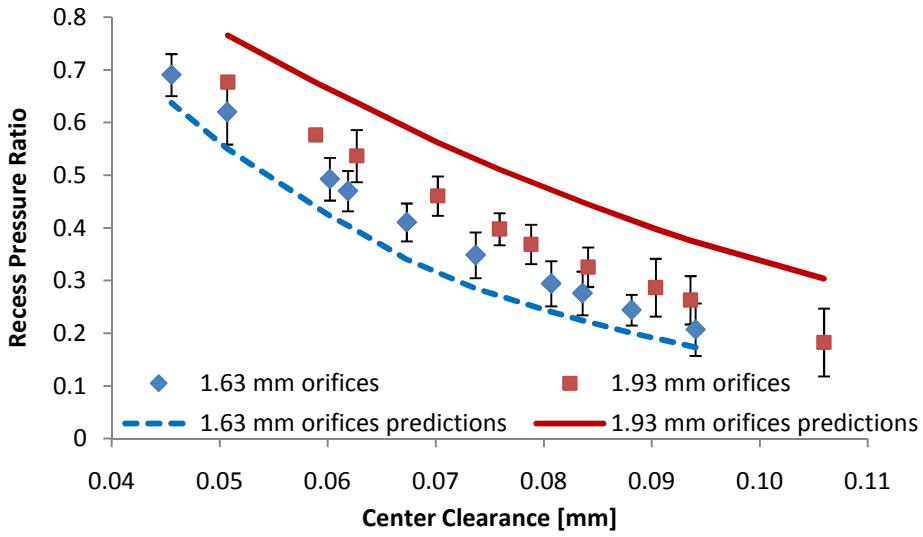

Figure 14: Measured and predicted [3] recess pressure ratio versus clearance at 5.17 bar supply and 0 rpm

Data for the largest (1.93 mm) orifice diameter at the highest speeds for both the 5.17 and 17.24 bar supply pressures do not follow the same trend as the previous test conditions. Figure 15 shows that at 17.5 krpm the recess pressure ratio in the largest (1.93 mm) orifice configuration is very similar to what is seen in smallest (1.63 mm) orifice diameter. This is also true for the 17.24 bar case as displayed in Figure 16. This plot also shows that the medium (1.80 mm) diameter orifice recess pressure ratio remains similarly larger than the 1.63 mm configuration as before. Overall, the experimental results for the largest (1.93 mm) orifice diameter tested display a strong dependence on both supply pressure and speed not seen in either of the other two orifice diameters nor any of the HYDROTHRUST® predictions. Also, these results do not correspond to inlet flow rate results, which were similar for all test conditions, and likewise showed similarly good agreement with predictions. This is an unexpected and interesting result that does not yet have an explanation. The other remaining bearing performance parameters including inner radius exhaust flow rate, operating clearances, and estimated axial stiffnesses are investigated for possible causes or clarification.

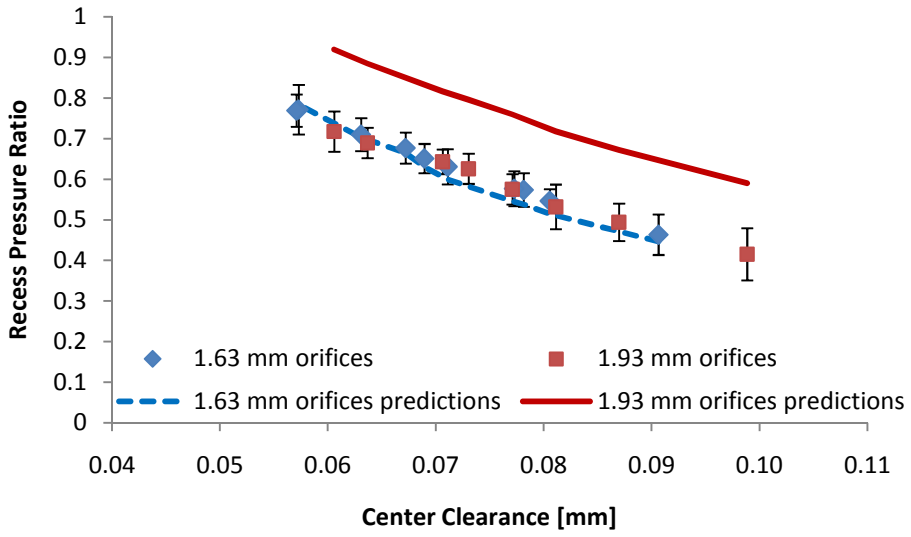

Figure 15: Measured and predicted [3] clearance versus recess pressure ratio at 5.17 bar supply and 17.5 krpm

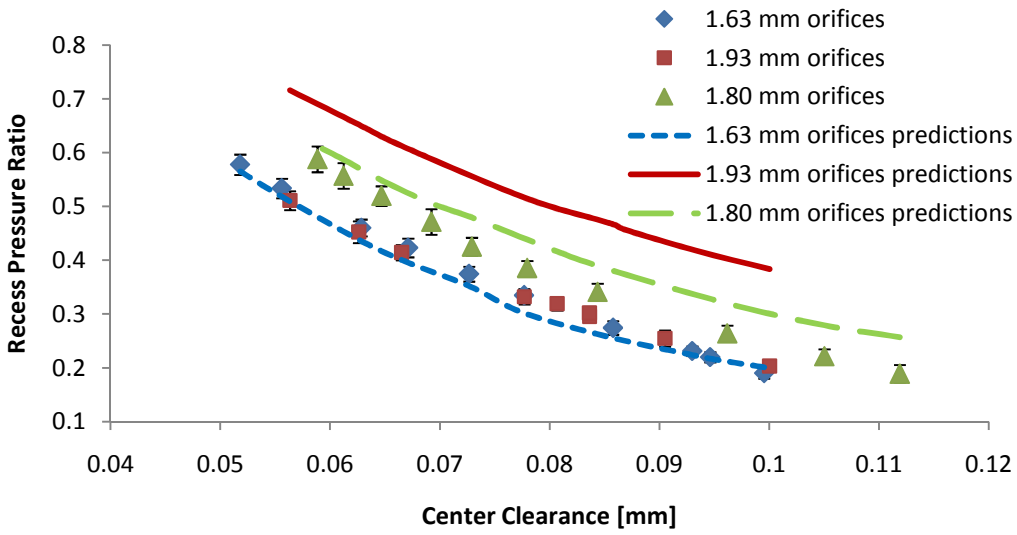

Figure 16: Measured and predicted [3] clearance versus recess pressure ratio at 17.24 bar and 12.5 krpm

5.3 Inner Radius Exhaust Flow Rate

Inner radius discharge flow rates are depicted in the following figures. Figures 17 and 18 show reasonable agreement between predictions and measurements for all three orifice diameters at 12.5 krpm and supply pressures of 17.24 and 10.34 bar, respectively. While uncertainties are generally larger those shown for the bearing inlet flow rate measurements, due to the smaller flow rates measured, the predications exhibit even better agreement with measurements. Similar to the inlet-flow-rate experimental results, these data show increasing inner radius exhaust flow rates with increases in orifice diameter for all test cases. There is also no further indication as to what may cause the surprising recess pressure ratio results for the large (1.93 mm) orifice diameter case.

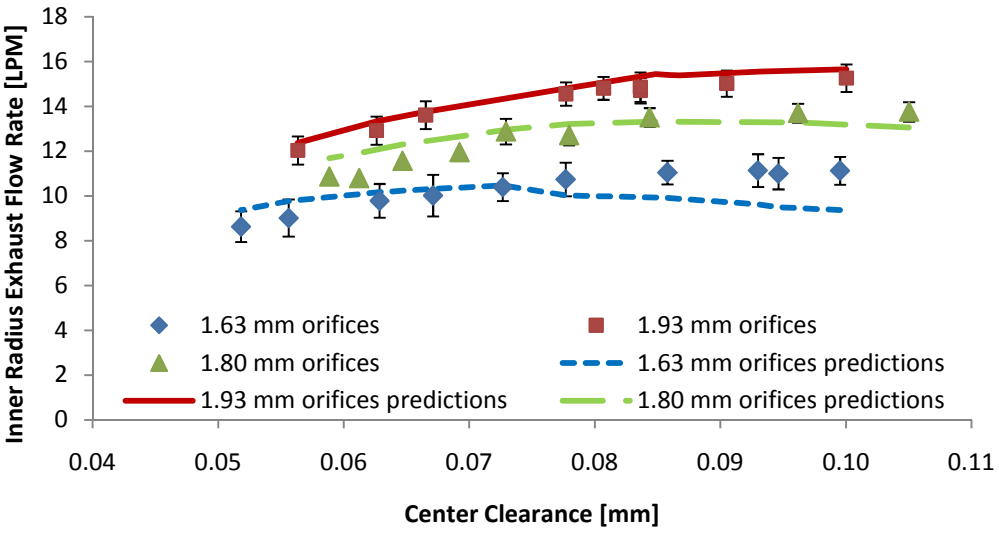

Figure 17: Measured and predicted [3] inner radius exhaust flow rate versus center clearance at 17.24 bar and 12.5 krpm

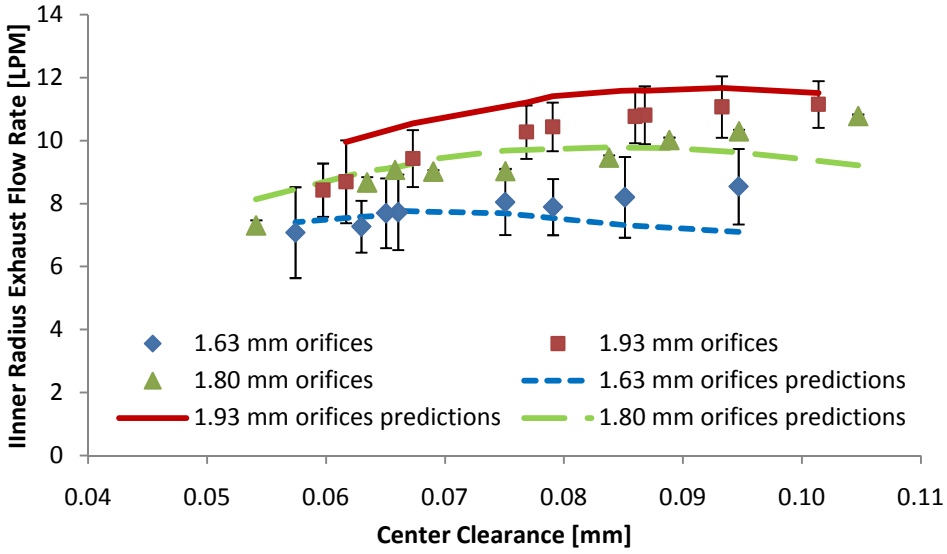

Figure 18: Measured and predicted [3] inner radius exhaust flow rate versus center clearance at 10.34 bar and 12.5 krpm

The inner radius discharge flow rate for the lower supply pressure of 5.17 bar is shown in Figures 19 and 20 at the lowest and highest tested speeds of 0 and 17.5 krpm, respectively. While larger relative uncertainties are seen (once again due to the even smaller flow rates measured) the same trend is seen as in the higher supply pressures. Note the significantly lower flow rates for the high speed test compared to the non-rotating case in both the data and predictions due to rotational effects more water to flow to the bearing's outer radius and limiting exhaust flow through the inner radius.

These results are particularly useful to predict the destructive phenomenon of bearing fluid starvation in bearings used at high speeds and low loads, as previously shown by Ramirez [17]. These results reinforce the ability of the HYDROTHRUST® predictive tool to calculate starvation as these plots trend toward starvation at the described test conditions. While the 5.17 bar supply pressure is higher, Ramirez showed the 3.45 bar pressure to exhibit this phenomenon and the trend shown is obviously similar. Also, note that the exhaust flow rates through the inner radius of the bearing are less than half of the total flow rate through the bearing shown in the inlet flow rate plots (Appendix E) for all supply pressures and speeds, as expected by San Andrés et al. [18].

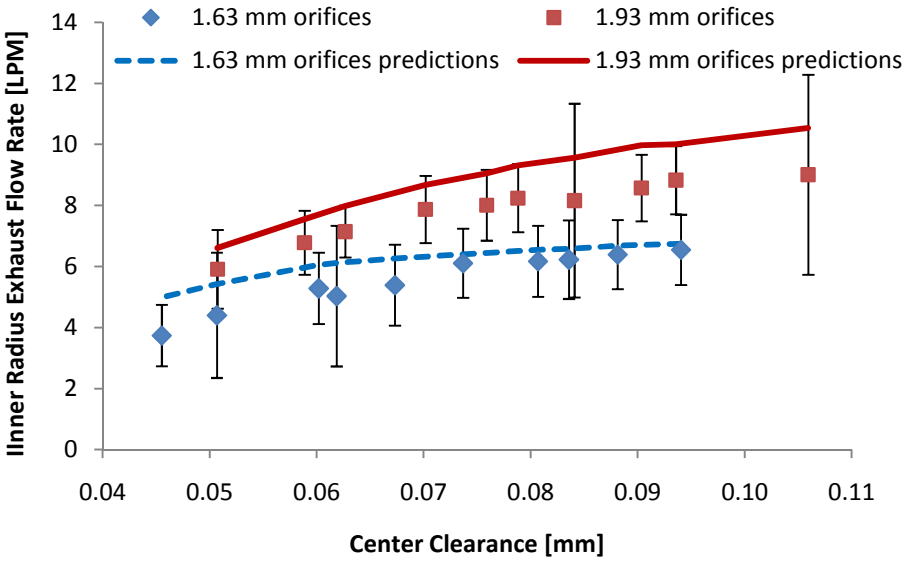

Figure 19: Measured and predicted [3] inner radius exhaust flow rate versus center clearance at 5.17 bar and 0 rpm

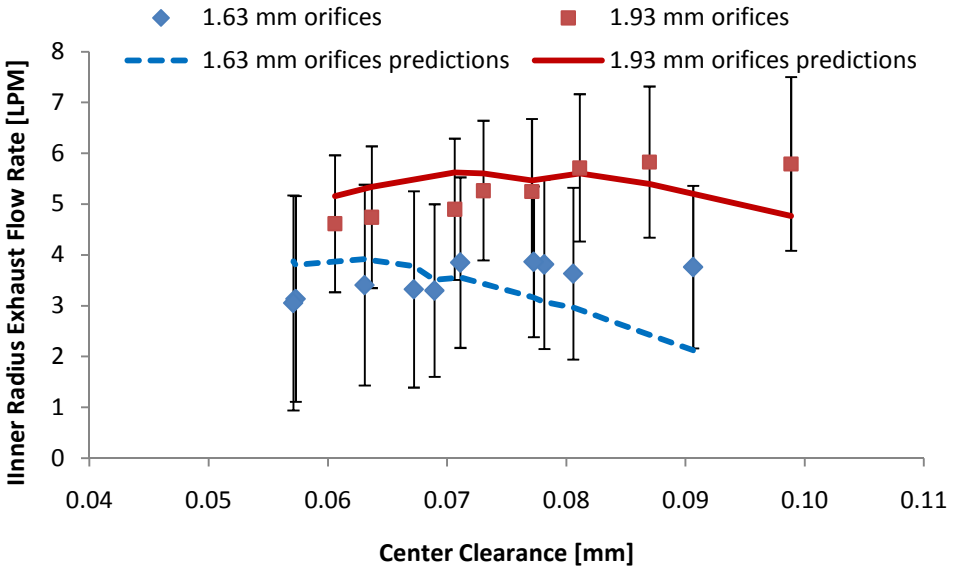

Figure 20: Measured and predicted [3] inner radius exhaust flow rate versus center clearance at 5.17 bar and 17.5 krpm

5.4 Operating Center Clearance

The measured axial clearance of a thrust bearing provides an indication of its fluid film thickness. An example of a center clearance versus load plot for individual thrust bearing proximity probes over an entire range of loads for a given supply pressure and speed test condition is displayed in Figure 21. The clearance-load behavior shown is similar for all three thrust bearings and all tests. Here, the output from the three proximity probes are plotted against the applied load for 1.63 mm orifice diameter bearing at a supply pressure of 17.24 bar and 7.5 krpm test condition. The misalignment discussed previously is mainly responsible for the discrepancies shown between the three proximity probes plotted. Also, note the prediction plotted is the bearing center clearance while the three proximity probes are located around the bearing flange. These variations between the three probes depicted are typical for all alignment measurements obtained. Note that the worst agreement between the probe outputs and prediction appears at low load conditions. The agreement between the three proximity probe measurements and predicted clearances also tends to improve as clearances get tighter. Additionally, the plot shows a similar trend to those presented by San Andrés [2], Wang and Yamaguchi [13], Forsberg [16], and Ramirez [17].

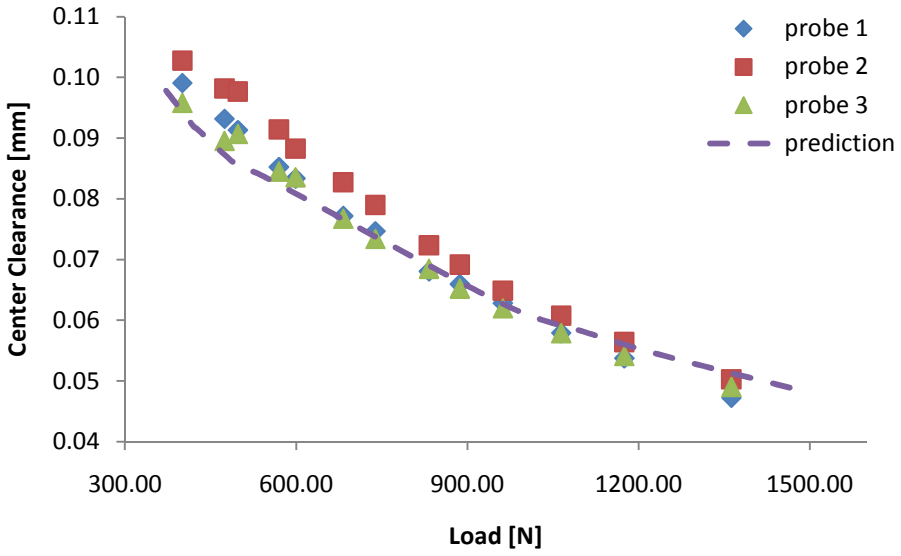

Figure 21: Measured and predicted [3] clearance versus load for 1.63 mm orifice bearing at 17.24 bar supply pressure and 7.5 krpm

The desired thrust bearing performance is a larger clearance for the same applied load. Figures 22 and 23 depict center clearance (fluid film thickness) versus load for the tested orifice diameters and predictions at 0 and 7.5 krpm and supply pressures of 5.17 and 10.34 bar, respectively. Both plots show similar results for the 1.63 mm and 1.93 mm orifice diameter bearings, with the larger orifice configuration displaying an increased operating clearance and therefore better performance. Also, predictions in the two plots show adequate agreement with measurements, especially for the 1.63 and 1.93 mm orifice diameter bearings. Figure 22 is representative of the 5.17 bar supply pressure data for all remaining speeds and predictions. Average measurement versus prediction error for clearance versus load data at this supply pressure are 11.7% and 14.2% for the small and large orifices, respectively.

Figure 23 shows a significantly lower operating clearance of the smallest diameter (1.63 mm) orifice bearing when compared to the two bearings with larger orifices diameters, which are surprising similar. The only small difference in center clearance is seen between the 1.80 mm and 1.93 mm orifice diameters at low loads. This difference diminishes at higher loads, as the two curves tend to converge. Figure 23 also shows that the 1.63 mm orifice diameter bearing consistently exhibits the lowest operating clearance at a given load when compared to the other two bearings over all speeds and supply pressures.

Also note there is virtually zero operating clearance increase gained by using the largest (1.93 mm) orifices compared to the medium diameter (1.80 mm) in the highest, 17.24 bar, supply pressure case, as shown in Figure 24. Experimental results suggest negligible differences in center clearances for the 1.80 mm and 1.93 mm orifice diameters over all supply pressures and speeds. However, both of these bearings display significant gains when compared to the smaller (1.63 mm) orifice diameter configuration. Again, the 1.80 mm and 1.93 mm orifice diameters provide best performance in terms of higher operating clearances. Clearance versus load results do not appear to aid in understanding the recess pressure measurements for the large orifice diameter bearing previously discussed.

Predictions for operating center clearance for both the small (1.63 mm) and large (1.93 mm) orifice diameters correlate well with experimental measurements. Comparisons with the middle diameter orifice bearing (1.80 mm) show reasonable agreement but generally slightly under predict clearances. All test cases show similar

agreement, with average percent differences between measured and predicted center clearances falling between 6.1% and 22.8%. This trend continues for the remaining data, at all supply pressures and speeds documented in Appendix H.

The clearance versus load data confirms that the larger orifice diameters, which generally have higher recess pressure ratios, also provide larger minimum clearances (fluid film thickness) for an applied load. In terms of operating clearance, larger orifices display the most desirable results. Additionally note that the larger clearances gained using the larger orifice diameters is offset by a higher flow rate requirement (discussed in Section 5.1) especially between the 1.93 mm and 1.63 mm orifice diameters. Obviously, higher flow rates would be expected through the larger orifice area provided by the larger orifice diameters (and larger C_d values).

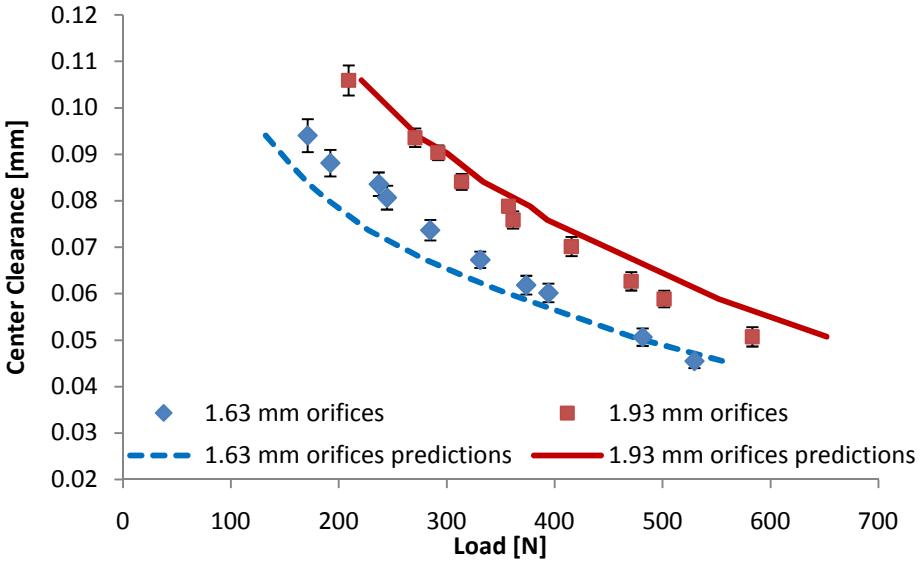

Figure 22: Measured and predicted [3] center clearance versus load at 5.17 bar supply and 0 rpm

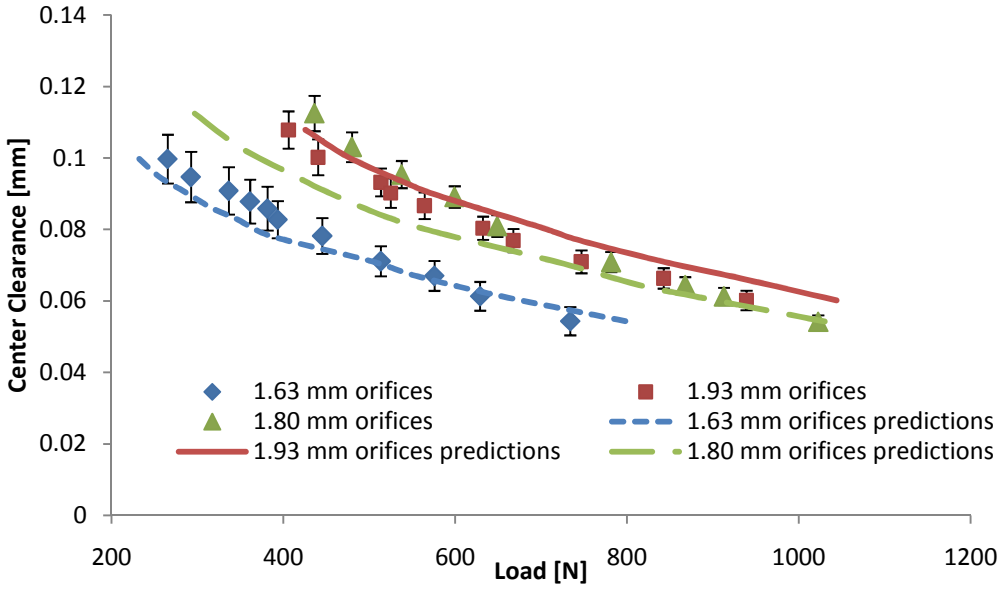

Figure 23: Measured and predicted [3] center clearance versus load at 10.34 bar supply and 7.5 krpm

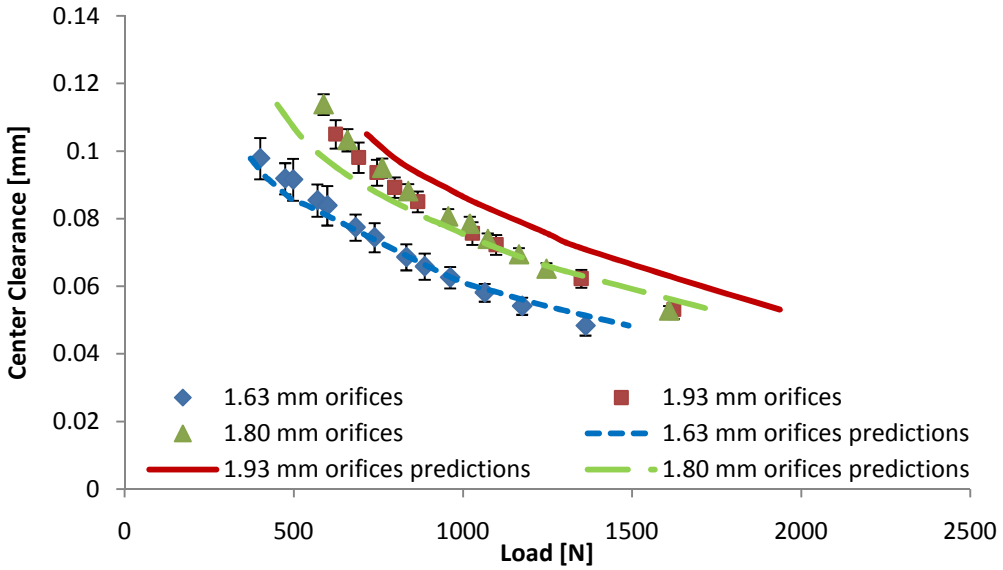

Figure 24: Measured and predicted [3] center clearance versus load at 17.24 bar supply and 7.5 krpm

Finally, Ramirez [17] found that the center clearance of this geometry bearing is not strongly influenced by shaft rotational speed (hydrodynamic effects) using the 1.80 mm orifice diameter bearing. The result is confirmed using the 1.63 mm and 1.93 mm orifice diameter bearings, with the 1.63 mm orifice diameter at 10.34 bar supply pressure data shown in Figure 25. The two larger orifices continue to have similar clearances for given loads and are not included in Figure 25 to limit its complexity. Similar results also occur for other supply pressures, albeit at increasing loads and clearances for increasing supply pressures. Supplemental figures for both of these results are found in Appendix H.

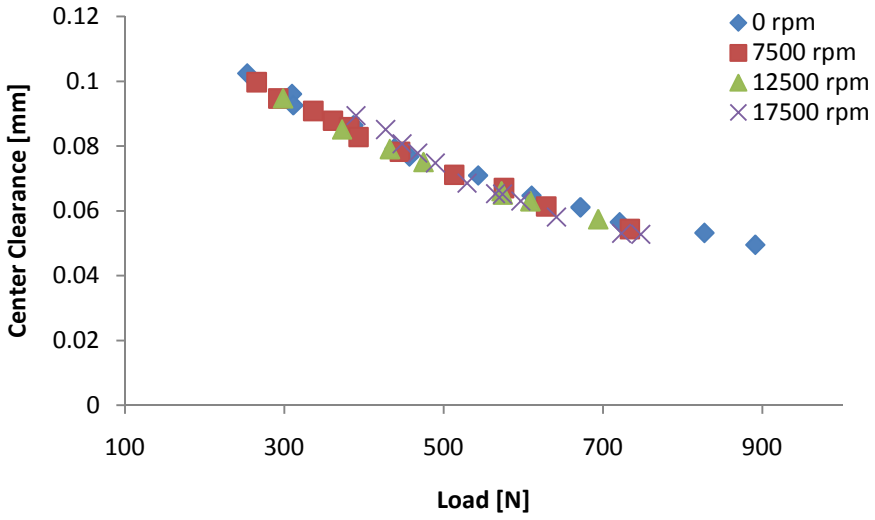

Figure 25: Measured and predicted [3] center clearance versus load at 10.34 bar supply and 1.63 mm orifice diameters for all speeds

5.5 Estimation of Axial Stiffness

Thrust bearing stiffnesses are vital performance characteristics, and the method used here to calculate the statically loaded axial stiffness is outlined in further detail by Forsberg [16] Stiffness predictions from HYDROTHRUST® are output in the matrix format

$$\begin{bmatrix} F_z \\ M_{\Phi_x} \\ M_{\Phi_y} \end{bmatrix} = \begin{bmatrix} K_{zz} & K_{z\Phi_x} & K_{z\Phi_y} \\ K_{\Phi_{xz}} & K_{\Phi_x\Phi_x} & K_{\Phi_x\Phi_y} \\ K_{\Phi_{yz}} & K_{\Phi_y\Phi_x} & K_{\Phi_y\Phi_y} \end{bmatrix} \begin{bmatrix} z \\ \Phi_x \\ \Phi_y \end{bmatrix} \tag{6}$$

Here, F_z is the load on the bearing face, M_a is the moment acting on the axis "a," $K_{mn}$is the stiffness coefficient for the "m" direction from the "n" variable, z is the thrust bearing clearance, and Φ_b is the misalignment angle about axis "b." Equation 6 leads to the following equation for axial force.

$$F_{zz} = K_{zz} * z + K_{z\Phi_x} * \Phi_x + K_{z\Phi_y} * \Phi_y \tag{7}$$

The data obtained here use static axial loading of the current thrust bearing rig and precludes direct comparisons between these predictions due to the inability to isolate a single stiffness term. However, an estimation of axial stiffness is obtained from the measurements by differentiating the clearance versus load curves.

This stiffness estimate is achieved by first curve fitting the clearance-versus-load data for each bearing and test condition. For both the 1.63 mm and 1.93 mm orifice data, a second order polynomial was used. For the 1.80 mm data, Forsberg [16] and Ramirez [17] use third and forth order fits respectively. In all cases, these are the lowest order polynomials that could follow the clearance versus load plot with reasonable error. The thrust bearing stiffness estimate is then found by differentiating the curve-fit equation.

This estimation method presents a significant uncertainty due to the differentiation function. This uncertainty is found using the following equation,

$$E_{dF/dZ} = \sqrt{E_A^2 + E_B^2 + E_C^2 + E_D^2} \tag{8}$$

The overall uncertainty is given as $E_{dF/dZ}$ and E_N is the uncertainty associated with the term N. The uncertainty of each term is found using TableCurve 2D software. This program provides a second method of curve fitting the data to check the previous one found using Excel, and produces uncertainties associated with each of the terms given. The overall uncertainties obtained for these results vary widely depending on the test condition, and generally range from less than 10% of the maximum value for the low speed, high pressure test conditions, to greater than 25% for high speed, low pressure conditions. As in other measurements, a decrease in speed (especially to zero) or increase in supply pressure causes a decrease in the uncertainties of the stiffness plots.

Thrust bearing stiffness is expected to increase with decreasing fluid film thickness. Plots of estimated stiffness follow. Estimated stiffness for the lowest supply pressure case of 5.17 bar is given in Figure 26 for the non-rotating case. Here, there is a small difference between the 1.63 mm and 1.93 mm orifice bearings.

Figure 27 provides a comparison of estimated stiffness for the three orifice diameters at 10.34 bar supply pressure and 7.5 krpm. For this case, the three bearings show similar stiffnesses at high clearances (low loads). As expected, the stiffness estimate increases for all three orifice diameters as the clearance decreases. In these reduced clearance conditions, the stiffness estimate increases with increasing bearing orifice diameter (and flow rates). The highest stiffness is the most desirable result as it provides increased rotor axial stability. Note that the maximum estimated stiffness appears at the minimum measured clearances for all three orifice diameters. Figure 28 shows an inverted version of the clearance-load data described previously and confirms the estimated stiffnesses correspond to the measured slopes. Here, the 1.93 mm orifice shows a steeper (larger) slope than the 1.80 mm orifice, which corresponds to the higher stiffness values shown.

Figure 29 shows the stiffness estimation results for the 17.24 bar supply pressure case. Here the estimated axial stiffness all three orifices have similar values, with slightly higher stiffness shown for increasing orifice diameters. The data does show a significant increase in stiffness for all three orifices with increasing supply pressure, as expected. Also, none of the three orifice diameters show significant changes in

estimated stiffness with changes in speed for any supply pressure. The trends shown in these figures continue for the remaining data found in Appendix I.

Note that the lowest operating clearance (shown in Figures 22 – 24 previously) for all test cases does not necessarily have the highest stiffness (preferred for better rotor axial stability). This indicates that orifice diameters providing the highest centering (reaction) forces on the rotor do not necessarily provide the highest stiffness. It will depend on the application to select a best configuration for these parameters.

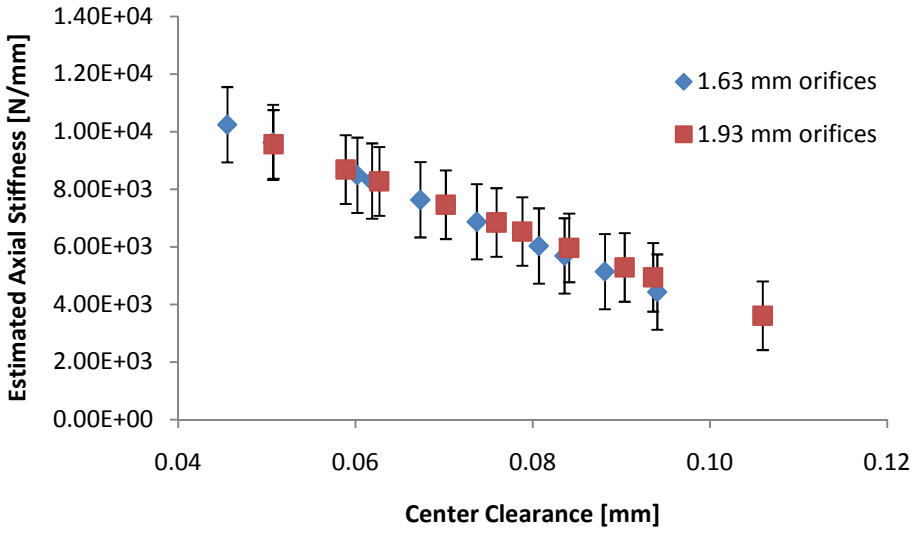

Figure 26: Estimated axial stiffness versus clearance at 5.17 bar and 0 rpm

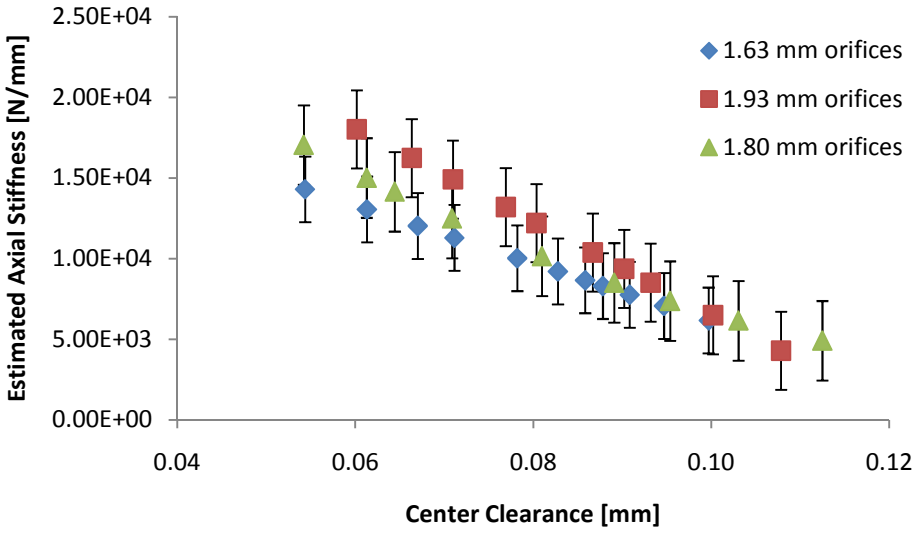

Figure 27: Estimated axial stiffness versus clearance at 10.34 bar and 7.5 krpm

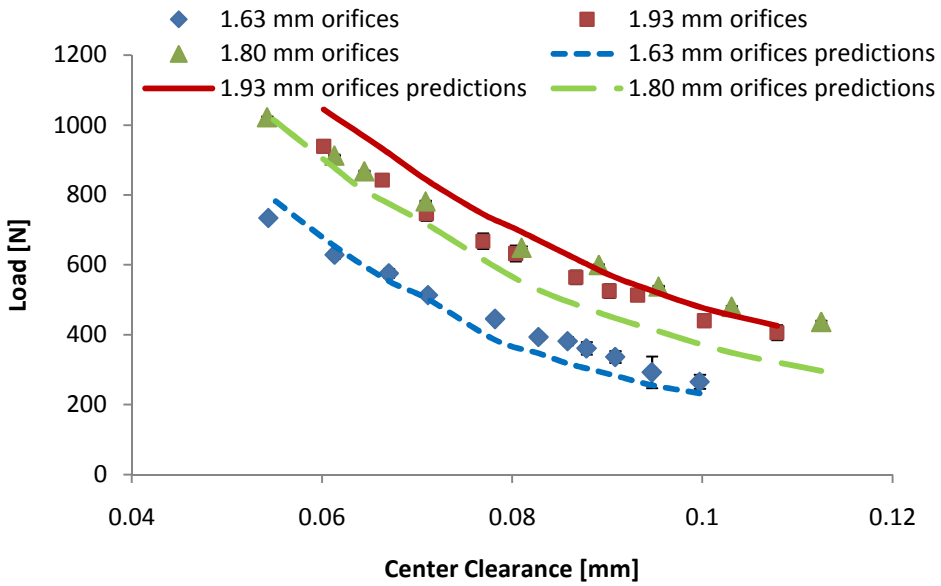

Figure 28: Measured and predicted [3] load versus center clearance at 10.34 bar and 7.5 krpm

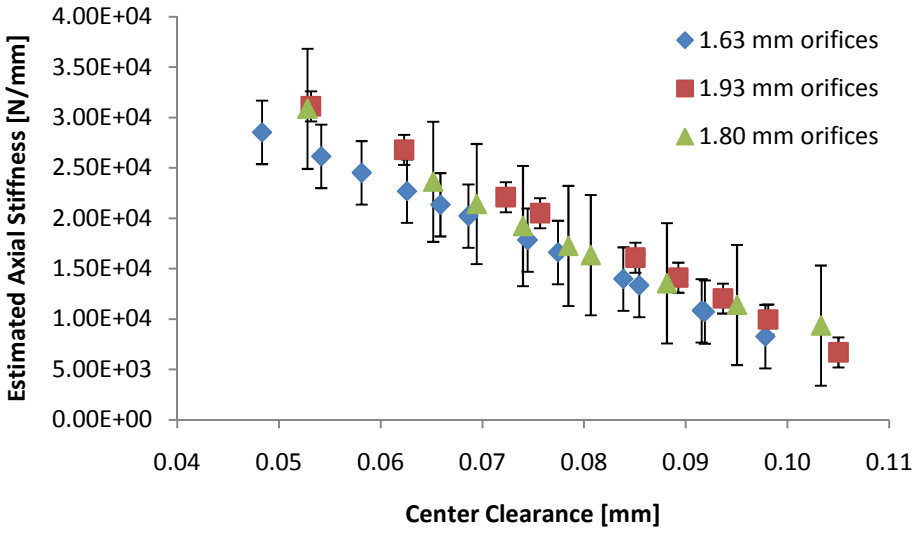

Figure 29: Estimated axial stiffness versus clearance at 17.24 bar and 7.5 krpm

6. SUMMARY AND CONCLUSIONS

A water-lubricated, hybrid thrust bearing was tested with three different orifice diameters using a face-to-face style test rig with supply pressures of 5.17, 10.34, and 17.24 bar, shaft rotational speeds of 0, 7.5, 12.5, and 17.5 krpm, and static loads from 125 to 1650 N. Experimental results were compared to predictions obtained using HYDROTHRUST® for recess pressure ratios, operating clearances, and inlet and exhaust flow rates. An estimation of axial stiffness was also presented.

Flow rate predictions for both the bearing inlet and inner radius exhaust tended to correlate very well with the data for all test conditions and configurations. Increasing orifice diameters showed an increase in flow rates for a given clearance, which also verifies that different orifice diameters were achieved. Average total differences between measurements and predictions were less than 10% for both flow rate measurements. The small (1.63 mm) orifice diameter bearing showed the lowest recess pressure ratios of the three bearings, with the middle (1.80 mm) orifice diameter bearing consistently being higher. Unexpected results were seen for the large (1.93 mm) orifice diameter bearing at both the low and high supply pressures where the bearing displayed similar recess pressures to the small orifice diameter bearing. Conversely, the large orifice diameter bearing had the highest recess pressure ratios at the 10.34 bar supply pressure. The cause of these results is unknown.

A limited increase in operating clearance for a given load was shown between the 1.80 mm and 1.93 mm orifice diameters, but both diameters exhibited an advantage over

the smallest, 1.63 mm orifice diameter configuration. Bearing inlet supply and inner radius exhaust flow rates increased with increasing orifice diameter for all test cases. Inner radius exhaust flow rates decreased with decreasing orifice diameter and supply pressure and increasing speed. As a matter of performance, limited operating clearance and estimated stiffness gains were seen over the test conditions through the use of the larger orifice diameter bearing, but it still required additional flow rates (and therefore additional loss in application), especially at higher supply pressures and low loads.

Predictions correlated well with recess pressure measurements for the medium, 10.34 bar, supply pressure condition for all three bearings configurations. Experimental results were lower than predictions for the largest (1.93 mm) orifice diameter bearing at both the low and high supply pressures (5.17 and 17.24 bar). Predictions for the other two smaller orifice diameter bearings continued to show adequate agreement with recess pressure measurements. Load predictions also showed adequate agreement with experimental data with a total percent difference near 13%. Exit flow rates displayed exceptionally good agreement with predictions for all three orifice diameters and all test conditions. Overall, HYDROTHRUST® continues to prove to be a powerful predictive tool.

It is difficult to suggest an optimum orifice diameter for hybrid thrust bearings. Larger orifices provide larger operating clearances and higher stiffnesses, but also require higher flow rates. A compromise between these parameters is obviously desired, and a desired axial clearance is often located in the middle of a bearing's load range to allow for some fluctuation. Additional data are needed to select an optimum orifice

diameter, and such a selection would undoubtedly depend on the desired operating characteristics of the bearing and its application.

Possible future work includes an investigation of stiffness and damping in hybrid thrust bearing performance. A further study of the effects of varying orifice diameters on both of these parameters would be a very useful tool and extension of this research. With few modifications, the same test rig used in obtaining data presented here could be utilized for dynamic (loading) testing of hybrid thrust bearings and to allow this data to be obtained, including direct stiffness and damping comparisons with predictions.

REFERENCES

[1] Minick, A. and Peery, S., 1998, "Design and Development of an Advanced Liquid Hydrogen Turbopump," *34th AIAA/ASME/SAE/ASEE Joint Propulsion Conference and Exhibit*, Cleveland, OH.

[2] San Andrés, L., 2000, "Bulk-Flow Analysis of Hybrid Thrust Bearings for Process Fluid Applications," *ASME Journal of Tribology*, 122 (1), pp. 170-180.

[3] San Andrés, L., 2002, "Effects of Misalignment on Turbulent Flow Hybrid Thrust Bearings," *ASME Journal of Tribology*, 124 (1), pp. 212-219.

[4] Mosher, P. and Childs, D.W., 1998, "Theory Versus Experiment for the Effects of Pressure Ratio on the Performance of an Orifice-Compensated Hybrid Bearing," *ASME Journal of Vibration and Acoustics*, 120 (4), pp. 930-936.

[5] Pinkus, O. and Lund, J.W., 1981, "Centrifugal Effects in Thrust Bearings and Seals Under Laminar Conditions," *ASME Journal of Lubrication Technology*, 103, pp. 126-136.

[6] Hashimoto, H., 1990, "The Effects of Fluid Inertia Forces on the Static Characteristics of Sector-Shaped High Speed Thrust Bearings in Turbulent Flow Regime," *ASME Journal of Tribology*, 111, pp. 406-411.

[7] Safar, Z.S., 1983, "Centrifugal Effects in Misaligned Hydrostatic Thrust Bearings," *ASME Journal of Lubrication Technology*, 105, pp. 621-624.

[8] New, N.H., 1974, "Experimental Comparison of Flooded, Directed, and Inlet Orifice Type of Lubrication for a Tilting Pad Thrust Bearing," *ASME Journal of Lubrication Technology*, 96 Ser F (1), pp. 22-27.

[9] Gregory, R.S., 1974, "Operating Characteristics of a Fluid-Film Thrust Bearing Subjected to High Shaft Speeds" *ASME Journal of Lubrication Technology*, 96 (1), pp. 7-14.

[10] Neal, P.B., 1982, "Heat Transfer in Pad Thrust Bearings," *Proceedings of the Institution of Mechanical Engineers 1847-1982 (vols 1-196)*, 1982, 196 (1982), pp. 217-228.

[11] Horner, D., Simmons, J.E.L. and Advani, S.D., 1986, "Measurements of Maximum Temperature in Tilting-Pad Thrust Bearings," *Technical Preprints - Presented at the ASLE 41st Annual Meeting.* (ASLE, Park Ridge, IL, USA, Toronto, Ont, Canada).

[12] Harada, M., Miyaji, R. and Anada, Y., 1987, "Turbulent Lubrication for a Hydrostatic Thrust Bearing with a Circular Recess: Vibration, Control Engineering, Engineering for Industry," *JSME International Journal: bulletin of the JSME*, 30 (269), pp. 1819-1825.

[13] Wang, X. and Yamaguchi, A., 2002, "Characteristics of Hydrostatic Bearing/Seal Parts for Water Hydraulic Pumps and Motors. Part 1: Experiment and Theory," *Tribology International*, 35 (7), pp. 425-433.

[14] Gardner, W.W., 1975, "Performance Tests on Six-Inch Tilting Pad Thrust Bearings," *ASME Journal of Lubrication Technology*, 97 ser F (3), pp. 460-438.

[15] Glavatskih, S.B., 2002, "Laboratory Research Facility for Testing Hydrodynamic Thrust Bearings," *Proceedings of the Institution of Mechanical Engineers -- Part J -- Journal of Engineering Tribology*, Professional Engineering Publishing, pp. 105-116.

[16] Forsberg, M., 2008, "Comparison Between Predictions and Experimental Measurements for an Eight Pocket Annular Hydrostatic Thrust Bearing," Texas A&M University, College Station, TX.

[17] Ramirez, F., 2008, "Comparison Between Predictions and Measurements of Performance Characteristics for an Eight Pocket Hybrid (Combination Hydrostatic/Hydrodynamic) Thrust Bearing, Texas A&M University, College Station, TX.

[18] San Andrés, L., Childs, D. and Phillips, S., 2008, "Static Load Performance of a Hybrid Thrust Bearing: Measurements and Validation of Predictive Tool," Texas A&M University, College Station, TX.

[19] Coleman, H.W. and Steele, G.W., 1988, *Experimentation and Uncertainty Analysis for Engineers*, John Wiley & Sons, Inc., New York.

APPENDIX A

RADIAL AND AEROSTATIC BEARING DETAIL

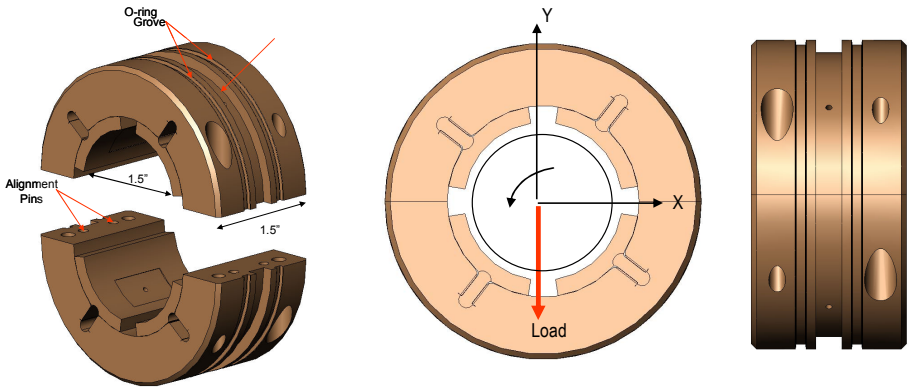

Figure A.1: Depiction of radial hybrid bearings [17]

Table A.1: Dimensions and physical parameters of hybrid radial bearings (flexure pivot type and made of bearing bronze) [17]

Nominal	Radial clearance	76.2 μm (3 mil)
Bearing	Inner Diameter	38.1 mm (1.5 inch)
	Outer Diameter	76.2 mm (3 inch)
	Length	38.1 mm (1.5 inch)
Pads	Number of pads	4
	Arc length	72 °
	Pivot offset (dim)	60% arc length
	Preload (dim)	0.20
	Flexure rotational stiffness	199.97 N-m/rad (1,770 lb_f-in/rad)
Pocket one per pad	Axial length	12.7 mm (0.50 inch)
	Arc length	24 °
	Depth	.508 mm (20 mil)
	Mean Diameter	54.864 mm (2.16 inch)
	Pocket/wetted area ratio	0.11
	Inlet coefficient from pocket to land	0.20
Orifice one per pocket	Diameter	1.702 mm (0.067 inch)
	Radial injection	50% of pocket length
	Entrance Loss Coefficient	0.80
Web	Radial width	3.56 mm (0.140 inch)
	Axial width	3.81 mm (0.150 inch)
	Length (radius-to-radius)	6.38 mm (0.251 inch)
	Radius	20.32 mm (0.80 inch)

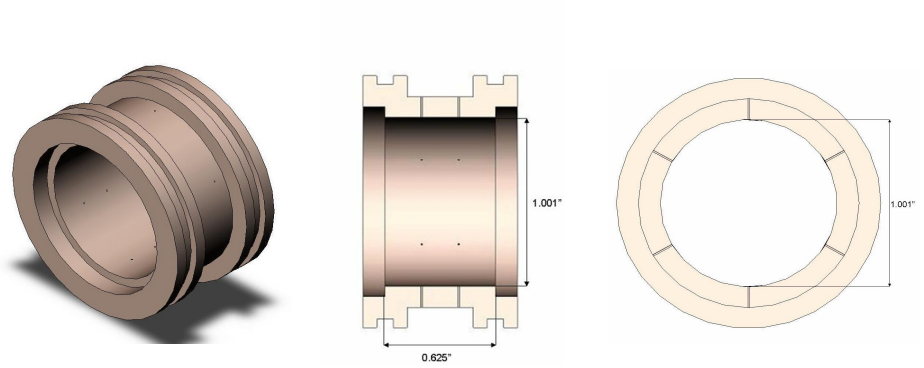

Figure A.2: View of aerostatic bearing (3d, side and front cross sections) [17]

Table A.2: Dimensions of aerostatic bearings, force coefficients and lateral natural frequencies of TB section and axial load shaft [17]

AEROSTATIC BEARINGS		**Supply Pressure: 6.89 bar (100 psig)**
Radial Clearance	12.7 μm (0.5 mil)	
Diameter	25.654 mm (1.01 inch)	
Axial Length	15.875 mm (0.625 inch)	
Number of holes	12	
Hole Diameter	.254 mm (0.010 inch)	C_d=0.86
Hole Pattern	Double Row, 6 per row	2.642 mm (0.104 inch) from midplane
	Left Bearing	**Right Bearing**
Static load	27.85 N (6.26 lb)	10.14 N (2.28 lb) (up)
Static displacement	2.794 μm (0.110 mil)	.99 μm (0.039 mil) (up)
Mass Flow	$1.25x10^{-4}$ kg/s ($2.76x10^{-4}$ lb/s)	$1.27x10^{-4}$ kg/s ($2.81x10^{-4}$ lb/s)
Pressure Ratio $(P_{max}-P_{atm})/(P_{supply}-P_{atm})$	0.77	0.50
Vertical motions		
Stiffness (K_{xx})	9911.7 N/mm (56.6 lb/mil)	10139.3 N/mm (57.9 lb/mil)
Damping (C_{xx})	518.35 N*s/m (2.96 lb*s/in)	351.99 N*s/m (2.01 lb*s/in)
Natural frequency &	196 Hz	1,000 Hz
Damping ratio	3.1%	16 %
Horizontal motions		
Stiffness (K_{yy})	10156.84 N/mm (58.0 lb/mil)	10191.87 N/mm (58.2 lb/mil)
Damping (C_{yy})	374.75 N/m (2.14 lb*s/in)	336.23 N/m (1.92 lb*s/in)
Natural frequency &	199 Hz	1,016 Hz
Damping ratio	2.3 %	11 %

XLTRC[2] used to predict lateral natural frequencies and damping ratios

APPENDIX B

UNCERTAINTY ANALYSIS OF EXPERIMENTAL MEASUREMENTS

Forsberg [16] and Ramirez [17] previously conducted an uncertainty analysis using the following method to estimate errors in experimental measurements and the validity of the data. Their method was simply repeated for the additional data obtained for this research. Errors can come from two sources (bias and precision). In this analysis, bias error is considered negligible and precision error is assumed to be the major error source. The precision error can come from several sources and must be propagated appropriately. To combine these errors the following equation is used [19].

$$E_N = \left[\Sigma \left(\frac{dF(X_1, X_2, ..., X_N)}{dX_N} * E_{XN} \right)^2 \right]^{1/2} \tag{B.1}$$

The overall error can be estimated with this equation as long as the function and individual variable errors are known. The measurement uncertainty (σ) can also be included into Equation (B.1) as one half of a summed squared term. Most of these individual errors are known from the error of the instrumentation; however, to determine the error from the calibration of the instrumentation Equation (B.2) must be introduced,

$$SEE = \left[\frac{\Sigma[Y_i - (aX_i - b)]^2}{M - 2} \right]^{1/2} \quad \text{(B.2)}$$

to determine the standard error of estimation (SEE) [19]. The SEE can then be used similarly to determine standard deviation of the error associated with a given curve fit parameter. The error derived from the SEE that is associated with a given variable is 2*SEE. This error band to either side of the calculated value will include approximately 95% of the possible points. The errors of the experimental measurements are defined with these two equations.

The flow rate is next found using the following equation.

$$FlowRate = A_{FlowMeter} * V - B_{FlowMeter} \quad \text{(B.3)}$$

Where

$A_{FlowMeter}$ = Linear calibration constant of the flow meter
$B_{FlowMeter}$ = Flow meter calibration offset
V = Flow meter output voltage

This equation can then be used with Equation (B.1) to find the expression for overall error.

$$E_{Flowrate} = \sqrt{(V * E_{AFlowMeter})^2 + (A_{FlowMeter} * E_V)^2 + (2 * \sigma_{Flow})^2} \quad \text{(B.4)}$$

Where

$E_{FlowMeter}$ = Flow meter error

$E_{AFlowMeter}$ = Error of $A_{FlowMeter}$ term

E_V = Error of flow meter voltage measurment

σ_{Flow} = Standard deviation of flow meter reading

This process can be repeated to find the error associated with the load measurement from

$$Load = A_{LoadCell} * V - B_{LoadCell} \quad \text{(B.5)}$$

Where

$A_{LoadCell}$ = Linear calibration constant of the load cell

$B_{LoadCell}$ = Load cell calibration offset

V = Load cell output voltage

Applying Equation (B.1) to Equation (B.5) the error expression is

$$E_{Load} = \sqrt{(A_{Load} * E_V)^2 + (2 * \sigma_{Load})^2} \quad \text{(B.6)}$$

Where

E_{Load} = Load cell error

E_V = Error of load cell voltage measurment

σ_{Load} = Standard deviation of flow meter reading

Finally the error associated with the differentiation estimation of the stiffness can be determined using

$$E_{dF/dZ} = \sqrt{E_A^2 + E_B^2 + E_C^2 + E_D^2} \tag{B.7}$$

Where

$Load = A * Z_C^4 + B * Z_C^3 + C * Z_C^2 + D * Z_C + E$

E_N = Error associated with term N

Z_C = Thrust bearing clearance

This equation requires that the error from each term is known; hence, the TableCurve2D software was utilized. This software calculates the error from each of the terms in the polynomial curve fit load expression. These errors were then substituted into Equation (B.7).

APPENDIX C

LABVIEW FRONT PANEL AND INSTRUMENTATION DETAIL

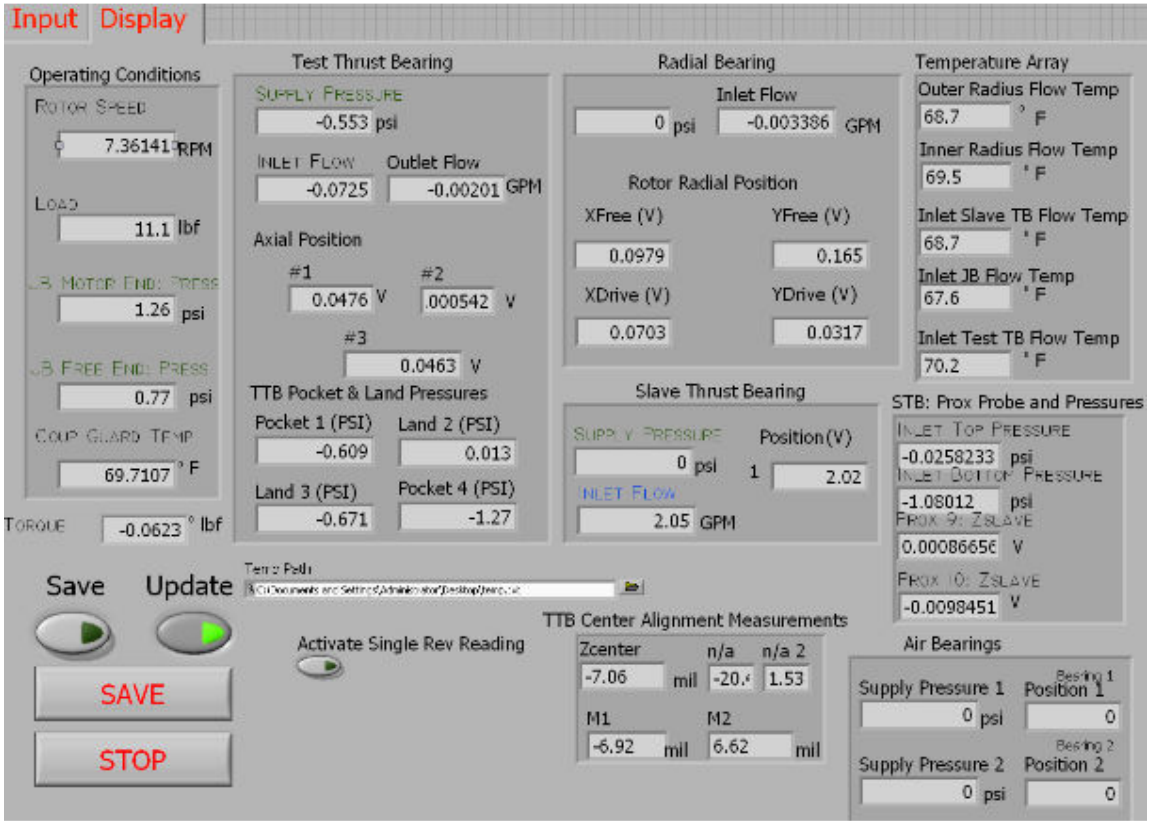

Figure C.1: LabVIEW VI Front Panel [17]

Table C.1: Instrumentation specifications [16]

Item description		Manufacturer's part number		Desired range	Sensor range	Power requirements	Output	Resolution
Vendor - SKF								
Drivers	CMSS 65 5mm Probe	CMSS 65-002-00-12-10	Test thrust bearing probe system driver	1-20 mil	10-90 mil	-24V at 15mA	0 to -13V	200 mV/mil
	CMSS 65 5mm Probe	CMSS 65-002-00-25-10	Radial probe system driver	5 mil	10-90 mil	-24V at 15mA	0 to -13V	200 mV/mil
Proximity Probes	CMSS 65 sensor	CMSS 365	Sensors for the drivers					
Extension Cables	7 meter extension cable		Extension cables for proximity probe system					
Vendor - FTI								
	FT 10	FT 10NEXW LES 2	Radial bearing inlet flow meter	8-15 GPM	0.3-15 GPM			
	FT6-6	FT6-6NEXW-LES-2	Test bearing inner radius discharge flow meter	0-4.75 GPM	0.16-7.5 GPM			
	FT-12	FT-12NEXW-LES-2	Test bearing inlet flow meter	0.27-13.45 GPM	0.25-20 GPM			
Digital Indicator	FTI Linear Link	BR30-2-C-4	Linearizes and outputs flowmeter reading ***All Flowmeters require one			24V at 300mW	4-20 mA	±0.1% of reading
Vendor - Omega								
Pressure Transducer	Omega FX209 Pressure Transducer	PX209-300G5V	Test thrust bearing lands/pocket pressure trancusers	0-250psi	0-300 psi	24V at 15mA		0.75 psi
	Omega FX209 Pressure Transducer	PX209-300G5V	Test thrust bearing inlet pressure trancducer	0-250psi	0-300 psi	24V at 15mA		0.75 psi
	Omega FX209 Pressure Transducer	PX209-300G5V	Journal bearing inlet pressure transducer	0-250psi	0-300 psi	24V at 15mA		0.75 psi
Transducer Displays	Signal display and output	DP253-E-A	Displays for pressure transducers			120Vac	±5V	0.02% of reading
	Signal display and output (Thermocouples)	DP253-TC-A	Displays for thermocouples			120Vac	±5V	0.5° C
Thermocouple wire	100 ft, Polyvinyl, 24 AWG, Type K	PR-K-24-100	Wire for thermocouples on outer and inner test thrust bearing radius					
Vendor - ENCORE								
Amplifier	Proximity sensor amplifier	Encore Model 619M-002				-24V to 24V		
Rack w/ Power Supply	Rack and power supply for amplifiers	Encore Model 4015-124				120Vac	24V to 24V	

APPENDIX D

MISALIGNMENT FIGURES

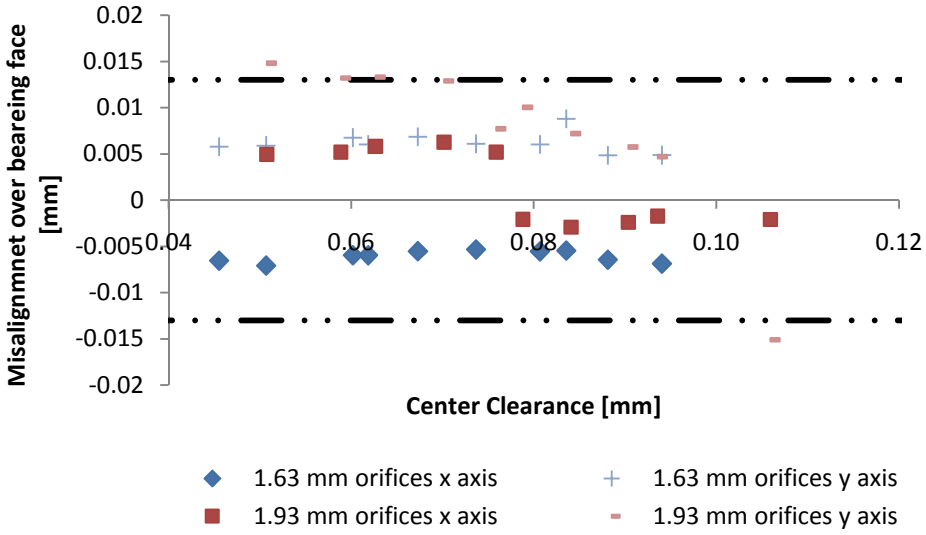

Figure D - 1: Misalignment over the bearing face about the x and y axis versus center clearance at 5.17 bar supply and 0 rpm

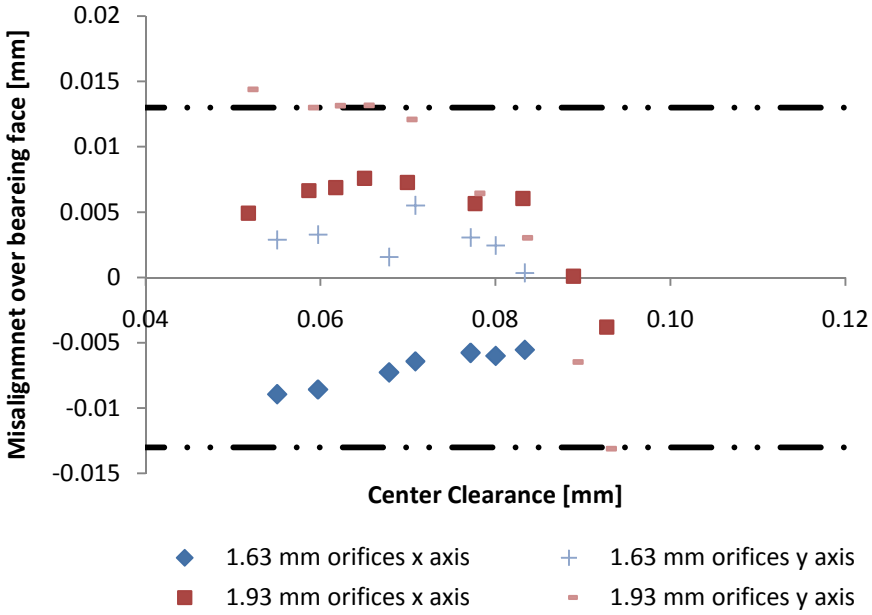

Figure D - 2: Misalignment over the bearing face about the x and y axis versus center clearance at 5.17 bar supply and 7.5 krpm

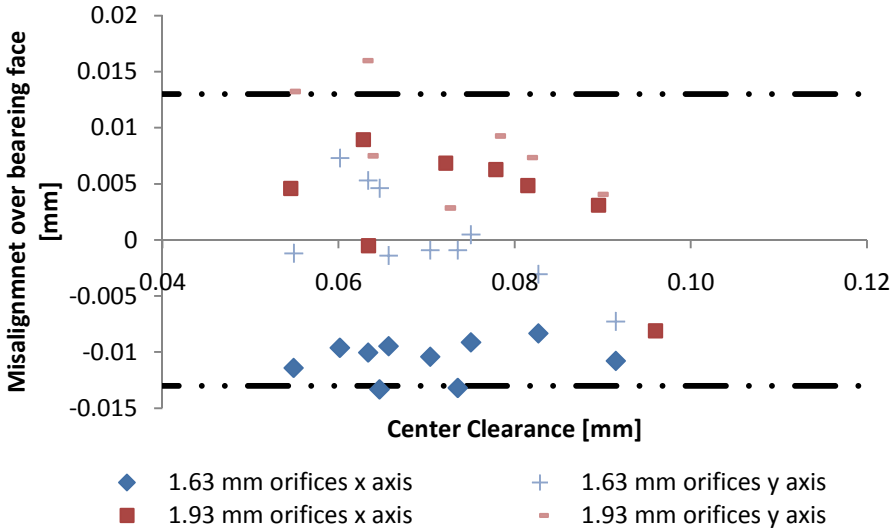

Figure D - 3: Misalignment over the bearing face about the x and y axis versus center clearance at 5.17 bar supply and 12.5 krpm

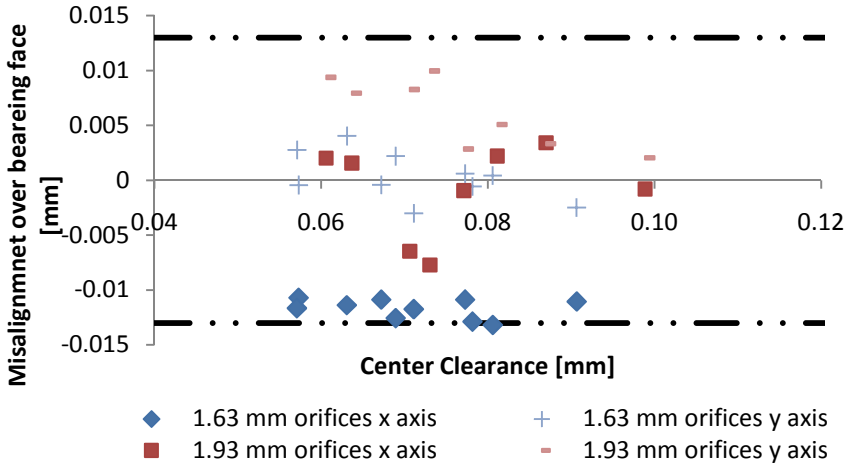

Figure D - 4: Misalignment over the bearing face about the x and y axis versus center clearance at 5.17 bar supply and 17.5 krpm

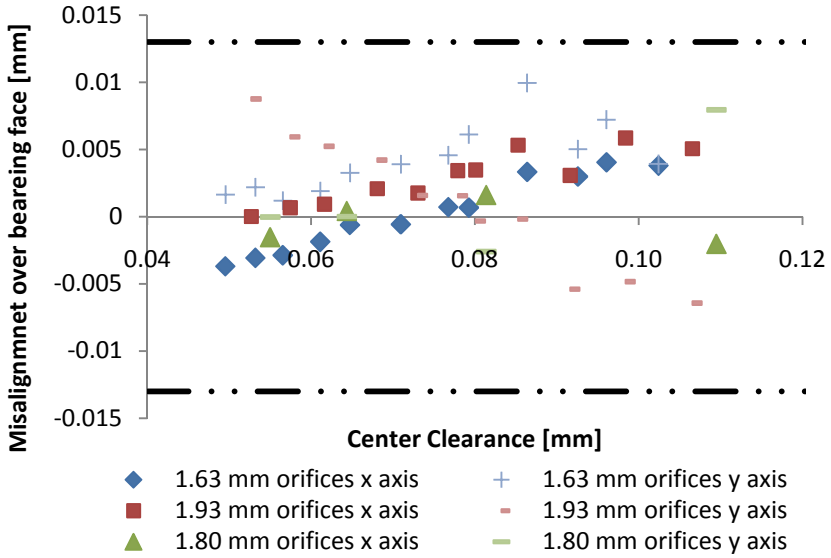

Figure D - 5: Misalignment over the bearing face about the x and y axis versus center clearance at 10.34 bar supply and 0 rpm

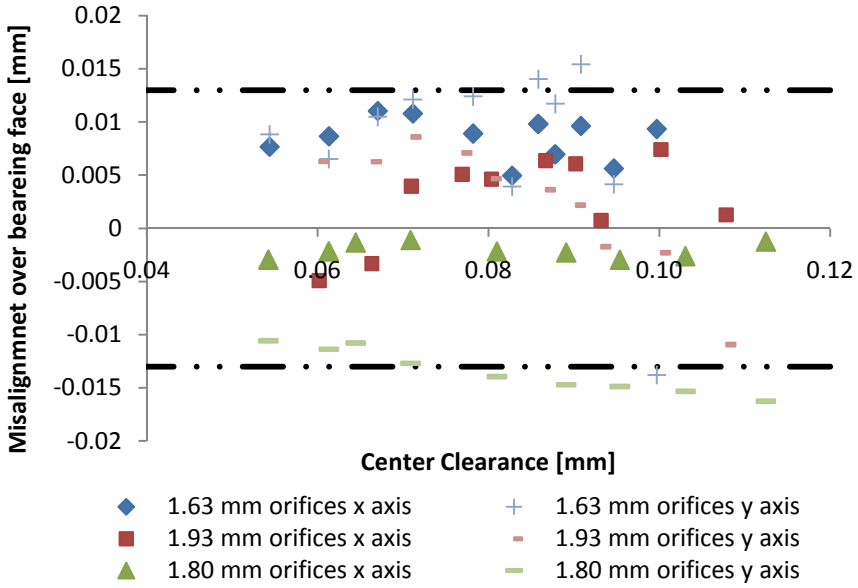

Figure D - 6: Misalignment over the bearing face about the x and y axis versus center clearance at 10.34 bar supply and 7.5 krpm

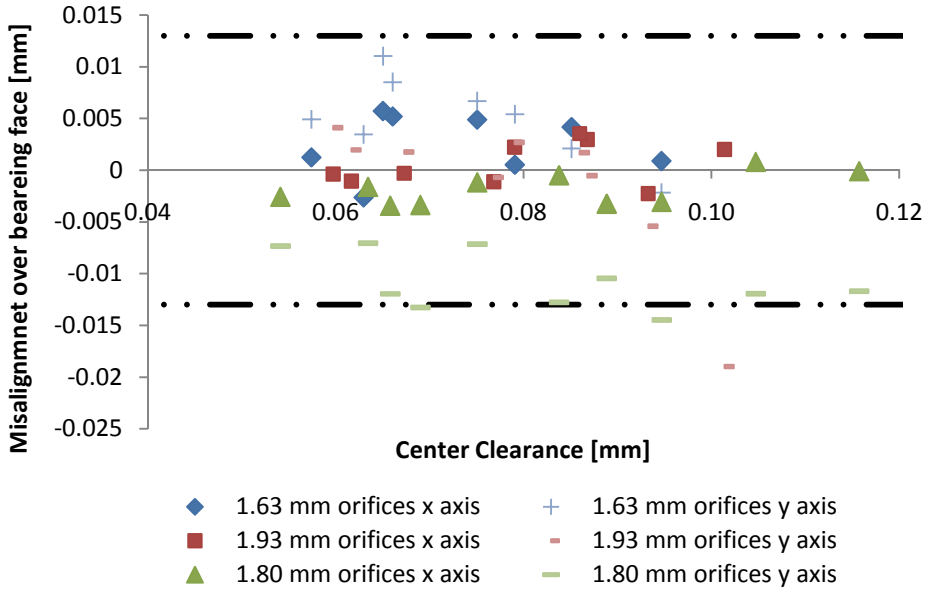

Figure D - 7: Misalignment over the bearing face about the x and y axis versus center clearance at 10.34 bar supply and 12.5 krpm

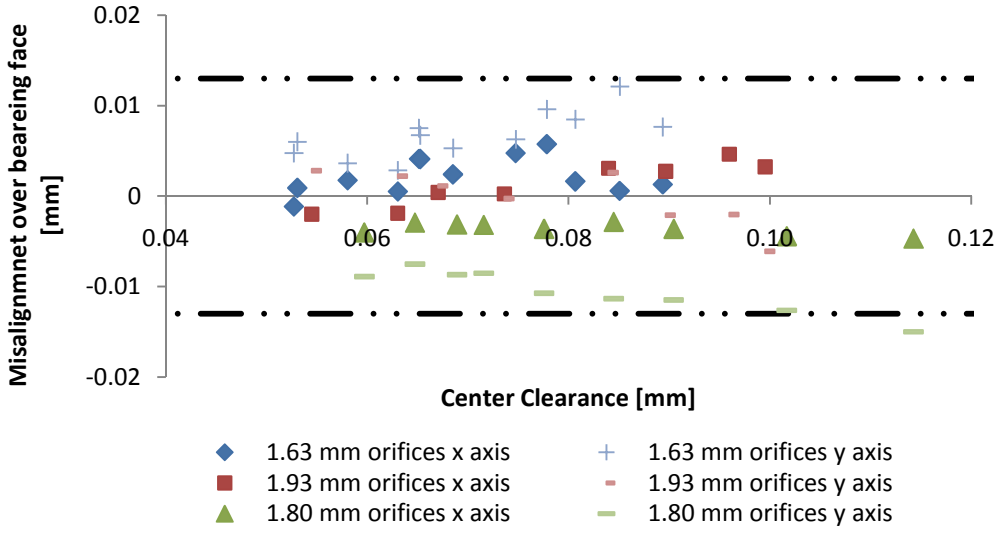

Figure D - 8: Misalignment over the bearing face about the x and y axis versus center clearance at 10.34 bar supply and 12.5 krpm

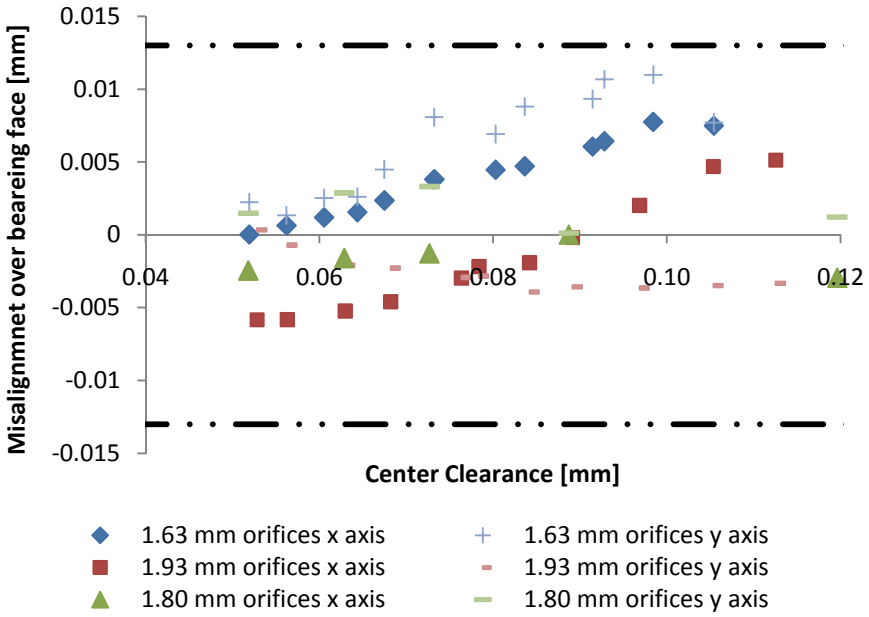

Figure D - 9: Misalignment over the bearing face about the x and y axis versus center clearance at 17.24 bar supply and 0 rpm

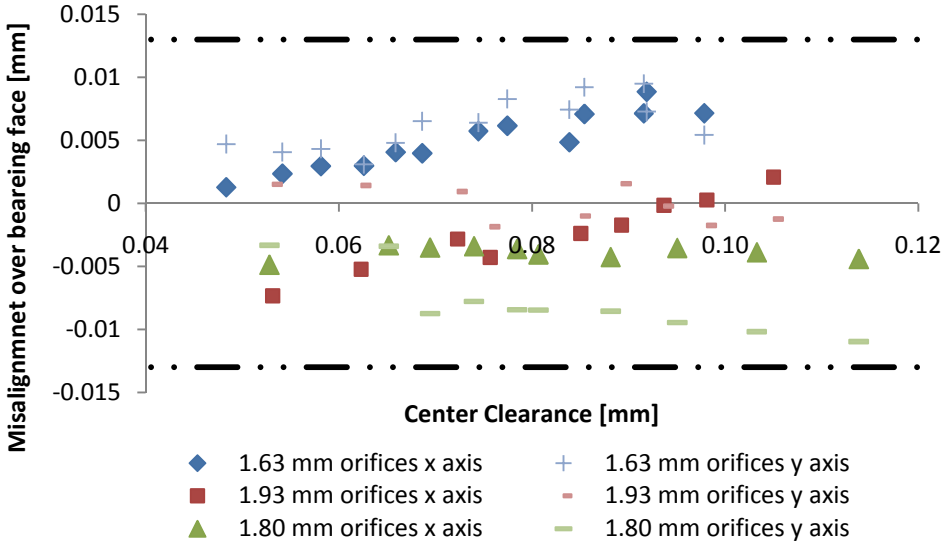

Figure D - 10: Misalignment over the bearing face about the x and y axis versus center clearance at 17.24 bar supply and 7.5 krpm

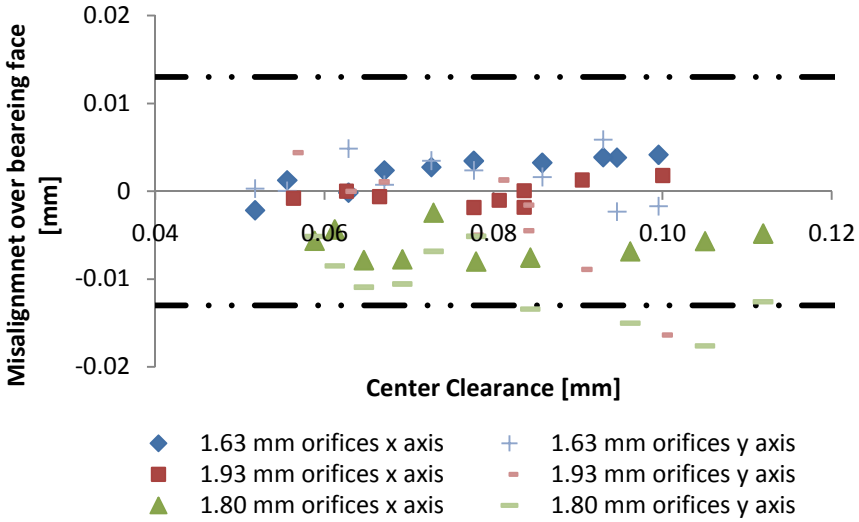

Figure D - 11: Misalignment over the bearing face about the x and y axis versus center clearance at 17.24 bar supply and 12.5 krpm

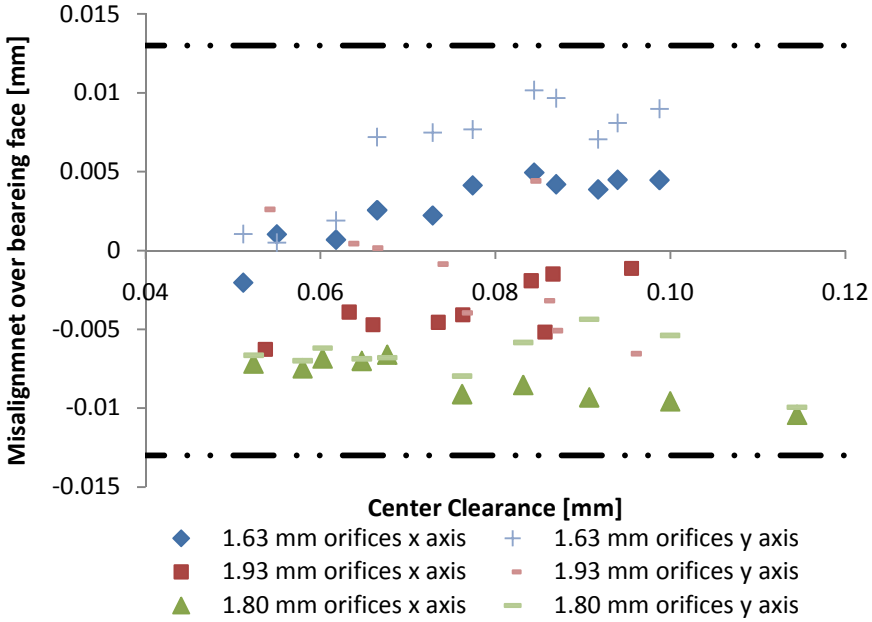

Figure D - 12: Misalignment over the bearing face about the x and y axis versus center clearance at 17.24 bar supply and 17.5 krpm

APPENDIX E

INLET FLOW RATE FIGURES

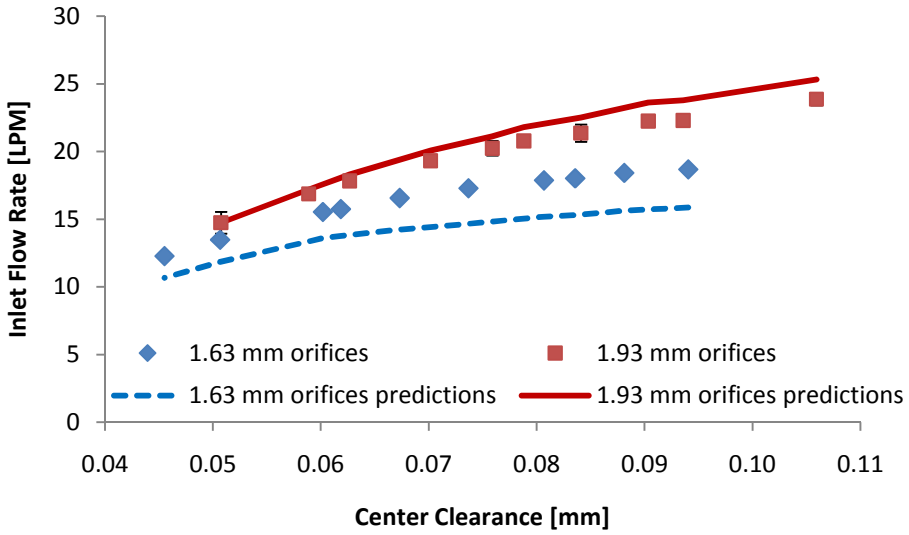

Figure E - 1: Measured and predicted [3] inlet flow rate versus clearance at 5.17 bar supply and 0 rpm

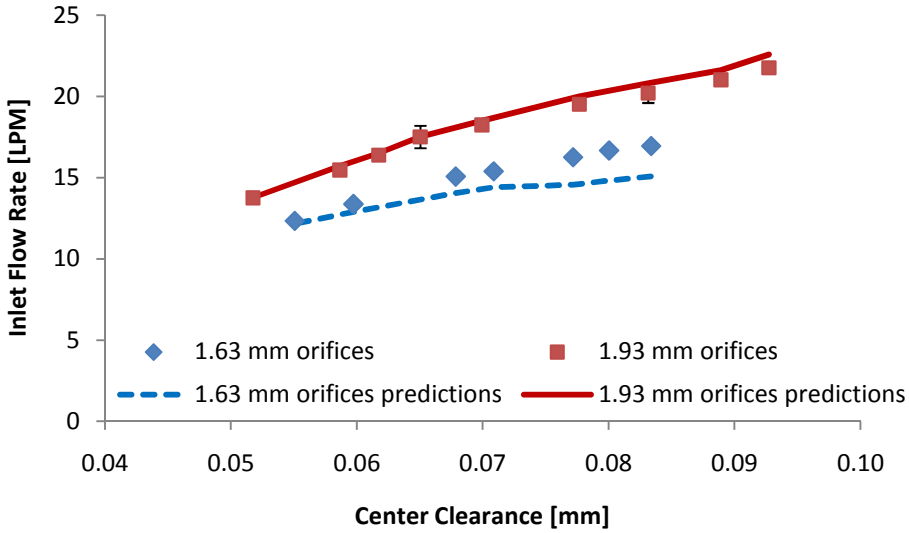

Figure E - 2: Measured and predicted [3] inlet flow rate versus clearance at 5.17 bar supply and 7.5 rpm

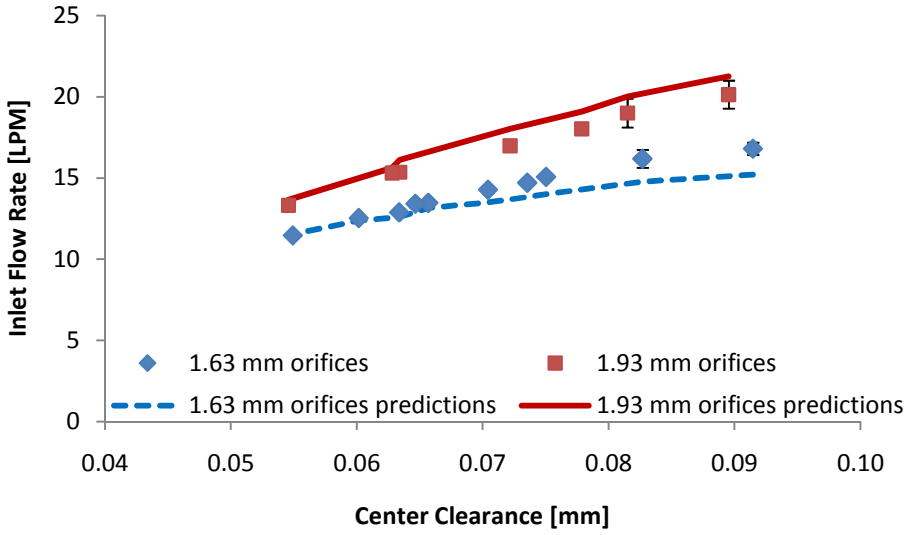

Figure E - 3: Measured and predicted [3] inlet flow rate versus clearance at 5.17 bar supply and 12.5 rpm

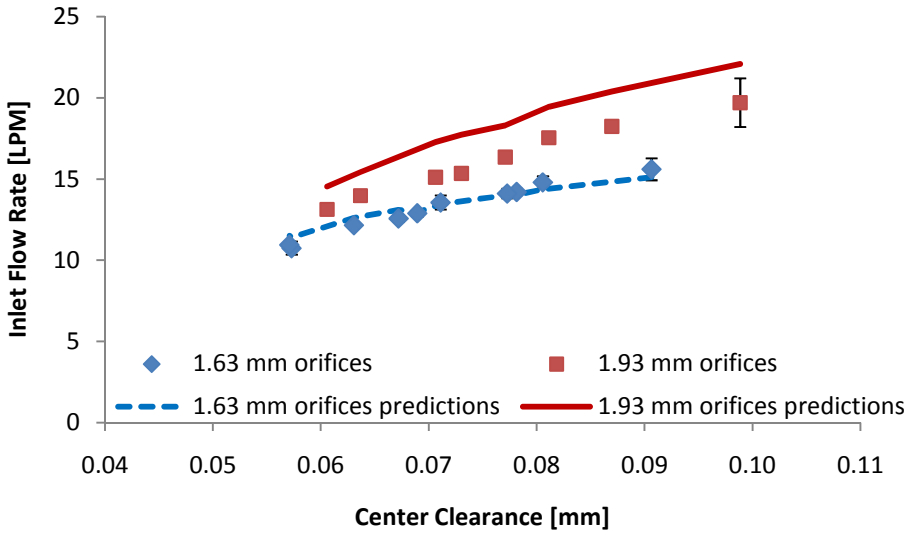

Figure E - 4: Measured and predicted [3] inlet flow rate versus clearance at 5.17 bar supply and 17.5 rpm

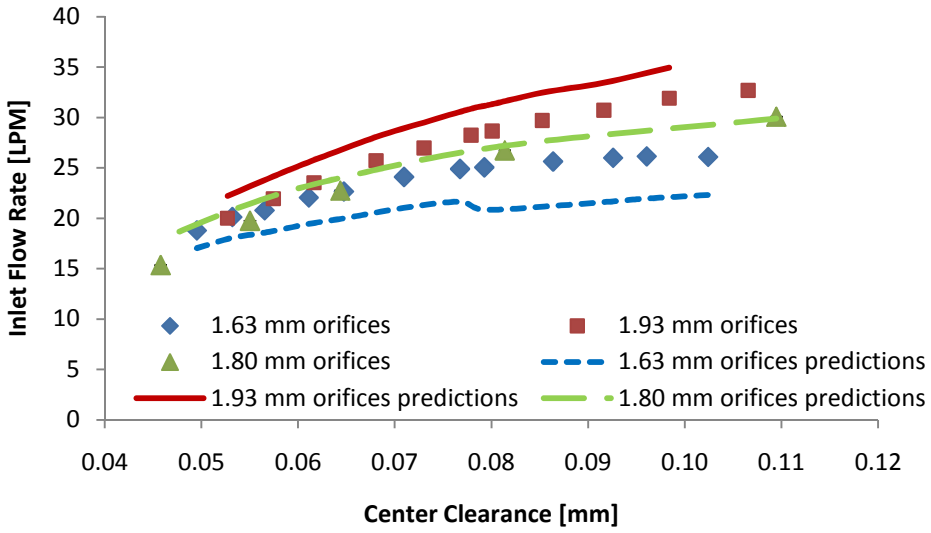

Figure E - 5: Measured and predicted [3] inlet flow rate versus clearance at 10.34 bar supply and 0 rpm

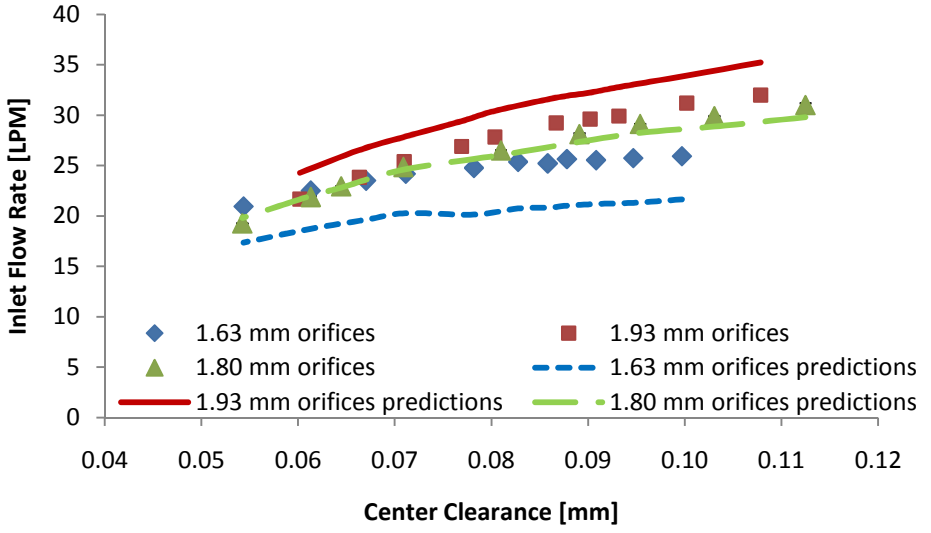

Figure E - 6: Measured and predicted [3] inlet flow rate versus clearance at 10.34 bar supply and 7.5 krpm

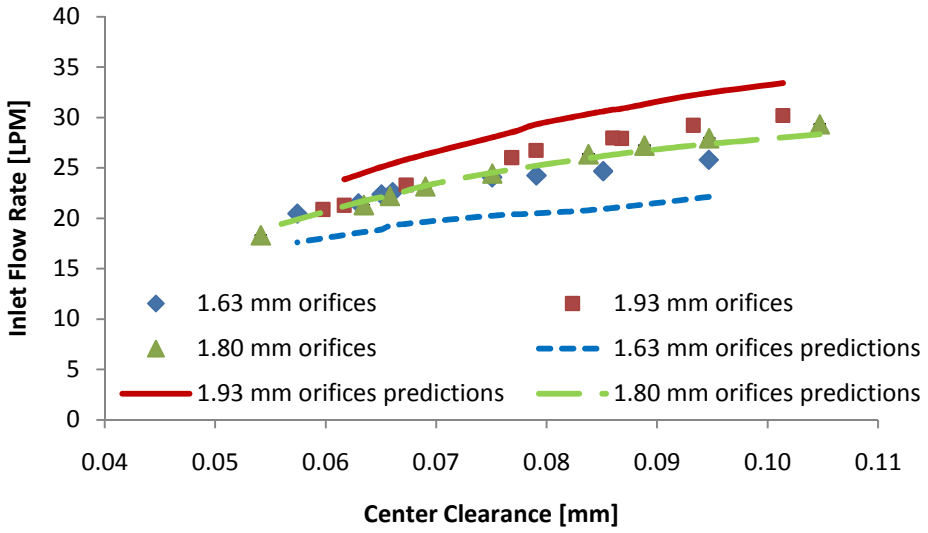

Figure E - 7: Measured and predicted [3] inlet flow rate versus clearance at 10.34 bar supply and 12.5 krpm

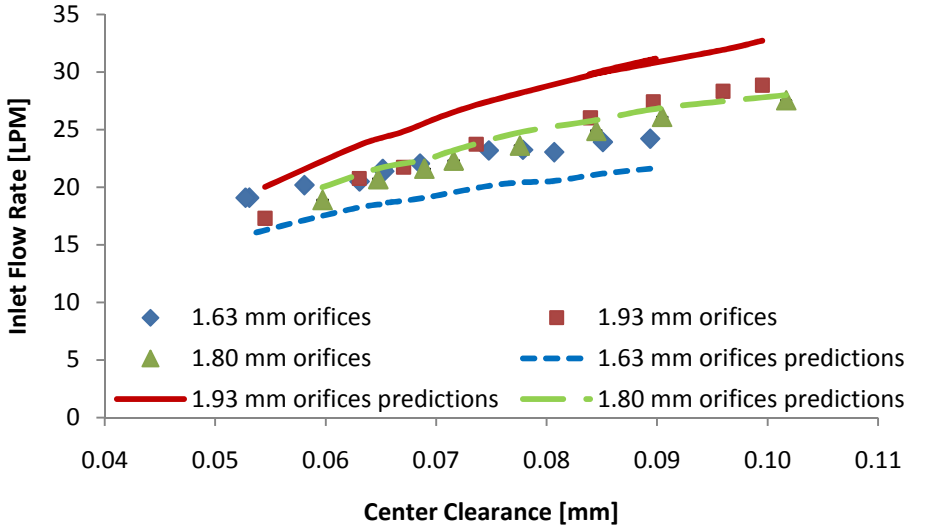

Figure E - 8: Measured and predicted [3] inlet flow rate versus clearance at 10.34 bar supply and 17.5 krpm

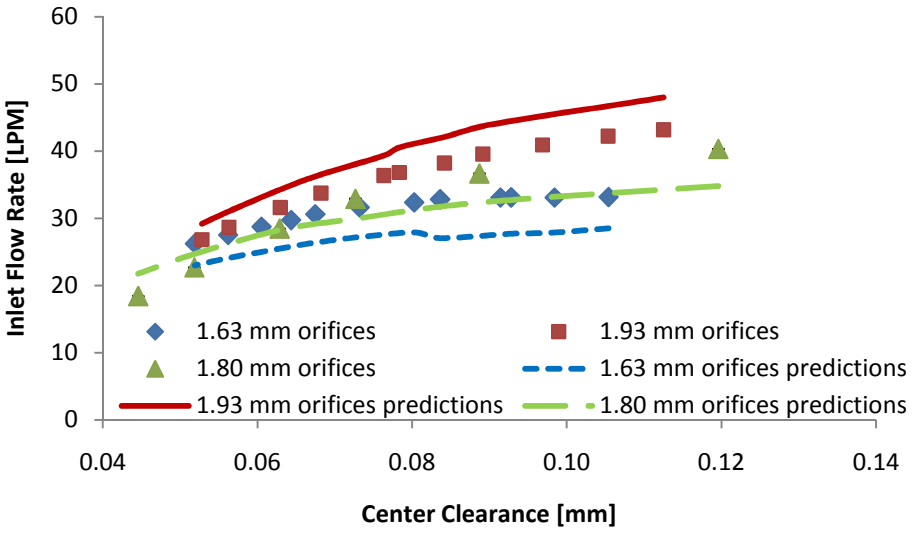

Figure E - 9: Measured and predicted [3] inlet flow rate versus clearance at 17.24 bar supply and 0 rpm

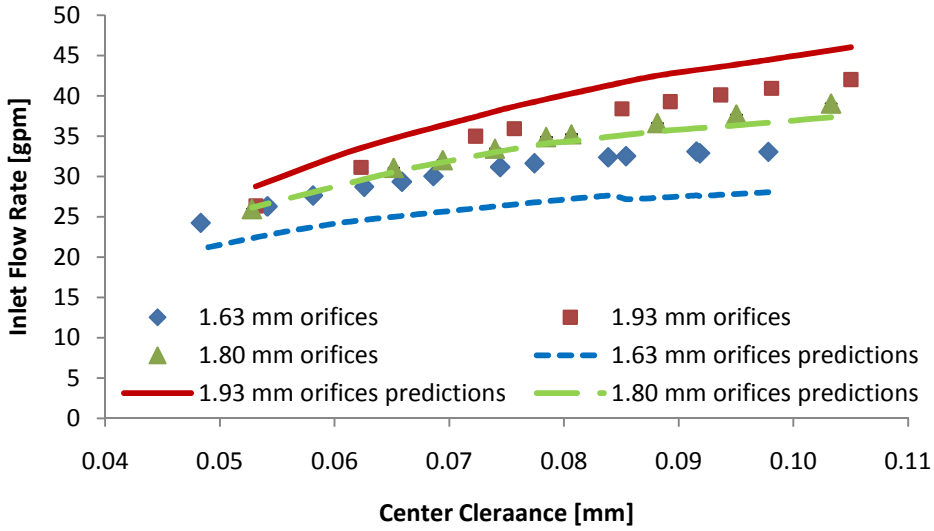

Figure E - 10: Measured and predicted [3] inlet flow rate versus clearance at 17.24 bar supply and 7.5 krpm

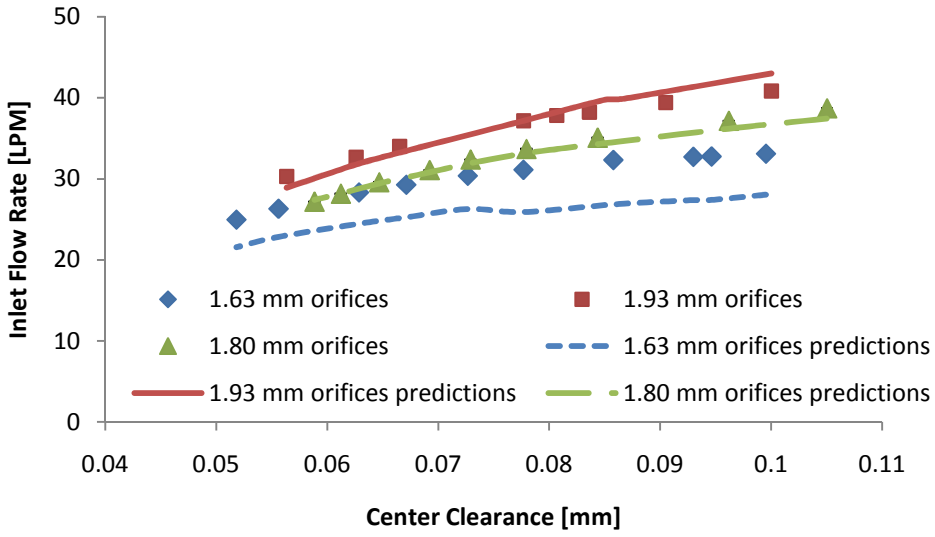

Figure E - 11: Measured and predicted [3] inlet flow rate versus clearance at 17.24 bar supply and 12.5 krpm

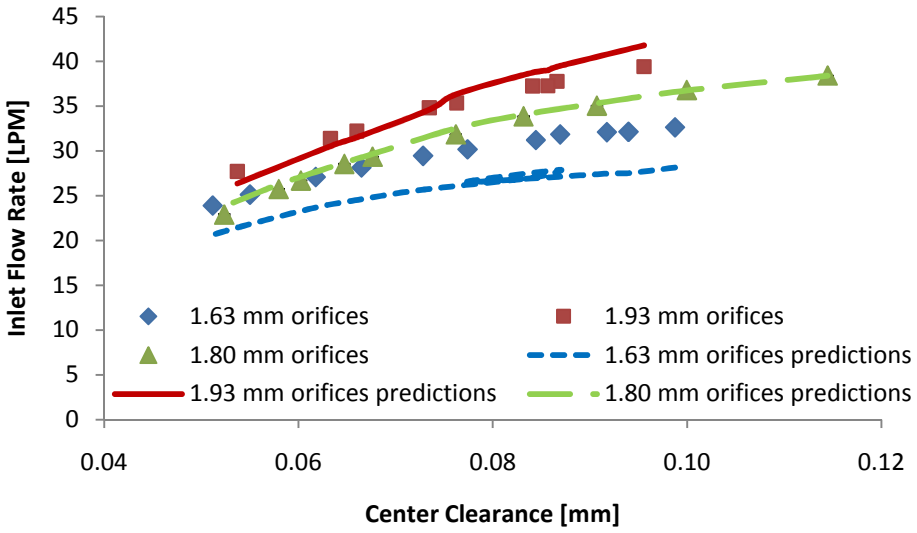

Figure E - 12: Measured and predicted [3] inlet flow rate versus clearance at 17.24 bar supply and 17.5 krpm

APPENDIX F

RECESS PRESSURE FIGURES

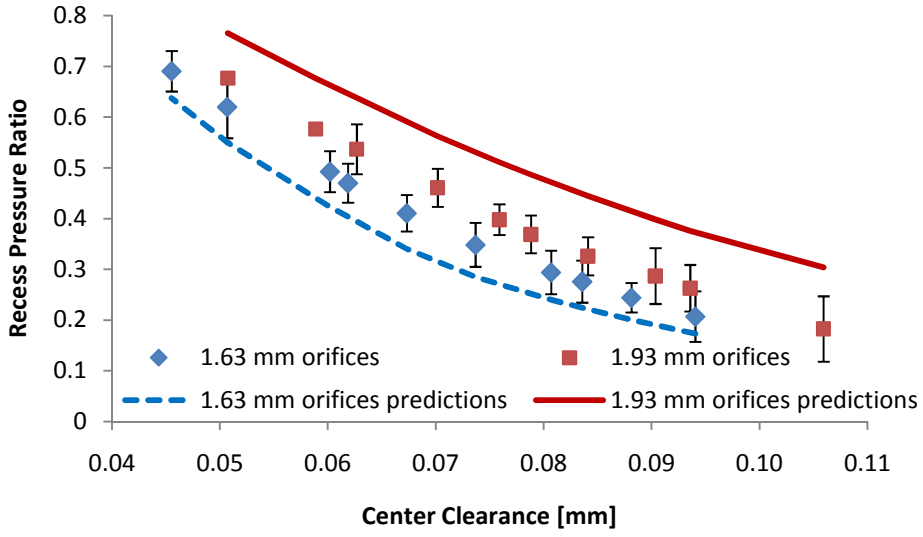

Figure F - 1: Measured and predicted [3] recess pressure ratio versus clearance at 5.17 bar supply and 0 rpm

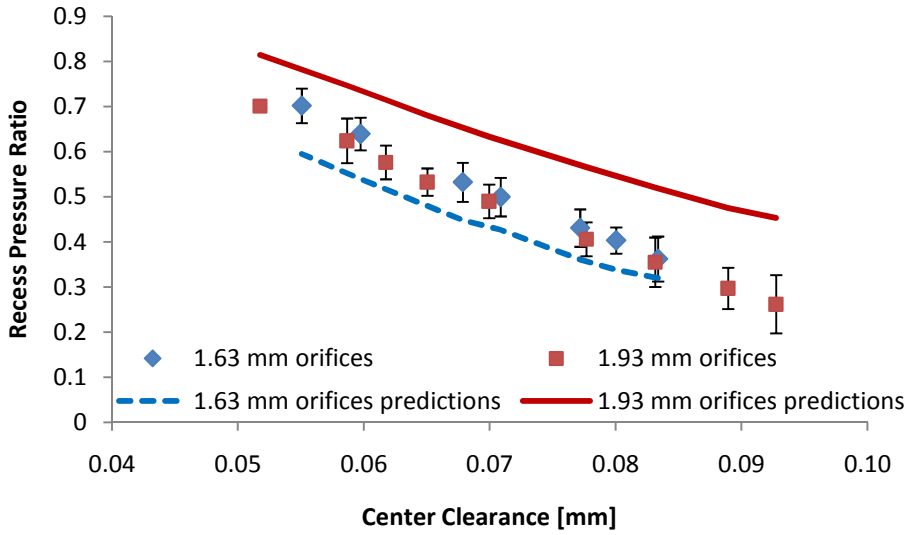

Figure F - 2: Measured and predicted [3] recess pressure ratio versus clearance at 5.17 bar supply and 7.5 krpm

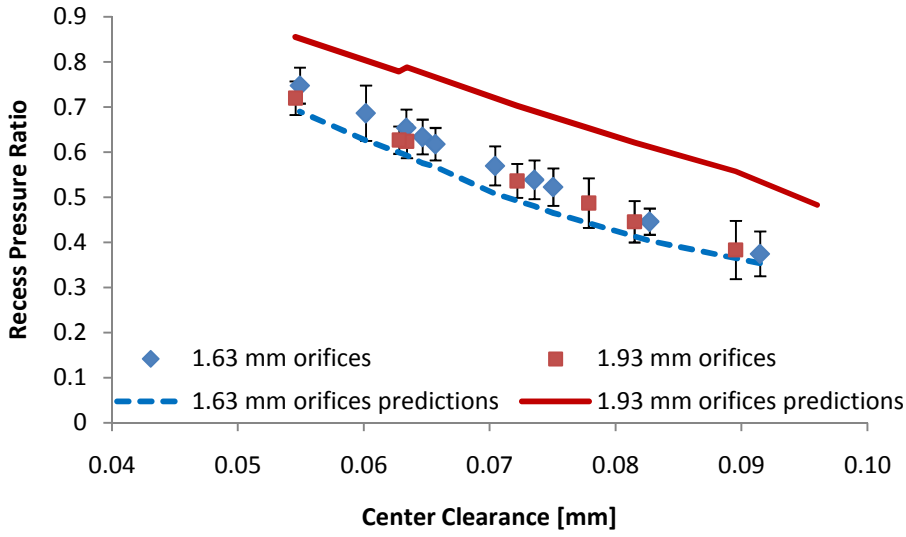

Figure F - 3: Measured and predicted [3] recess pressure ratio versus clearance at 5.17 bar supply and 12.5 krpm

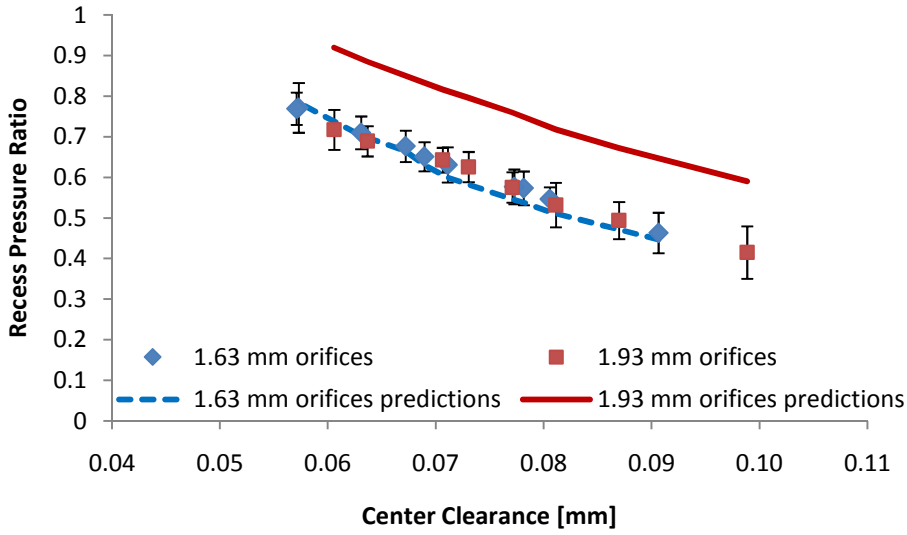

Figure F - 4: Measured and predicted [3] recess pressure ratio versus clearance at 5.17 bar supply and 17.5 krpm

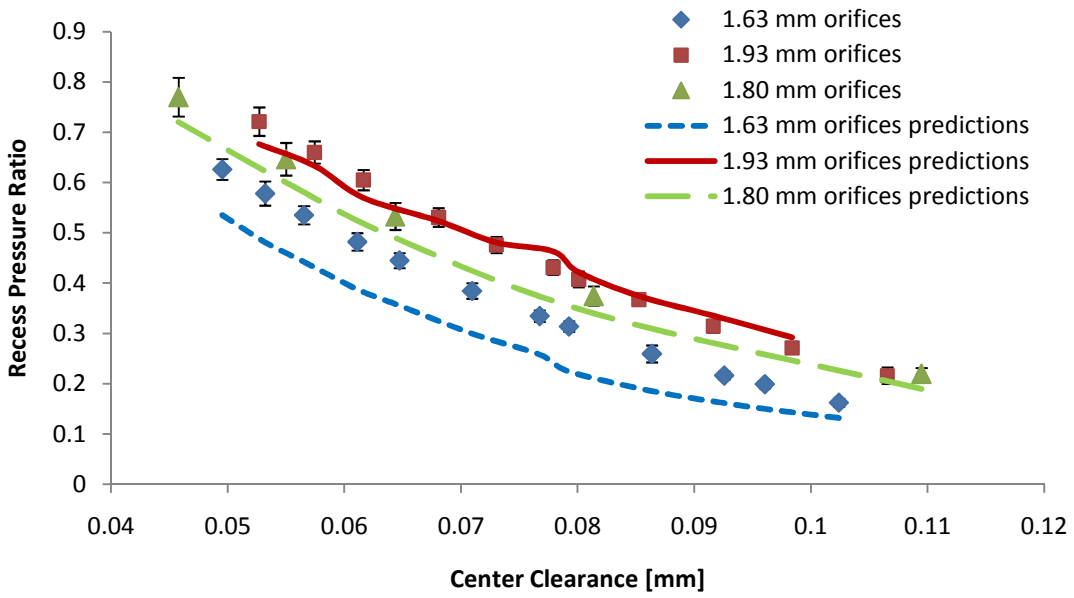

Figure F - 5: Measured and predicted [3] recess pressure ratio versus clearance at 10.34 bar supply and 0 rpm

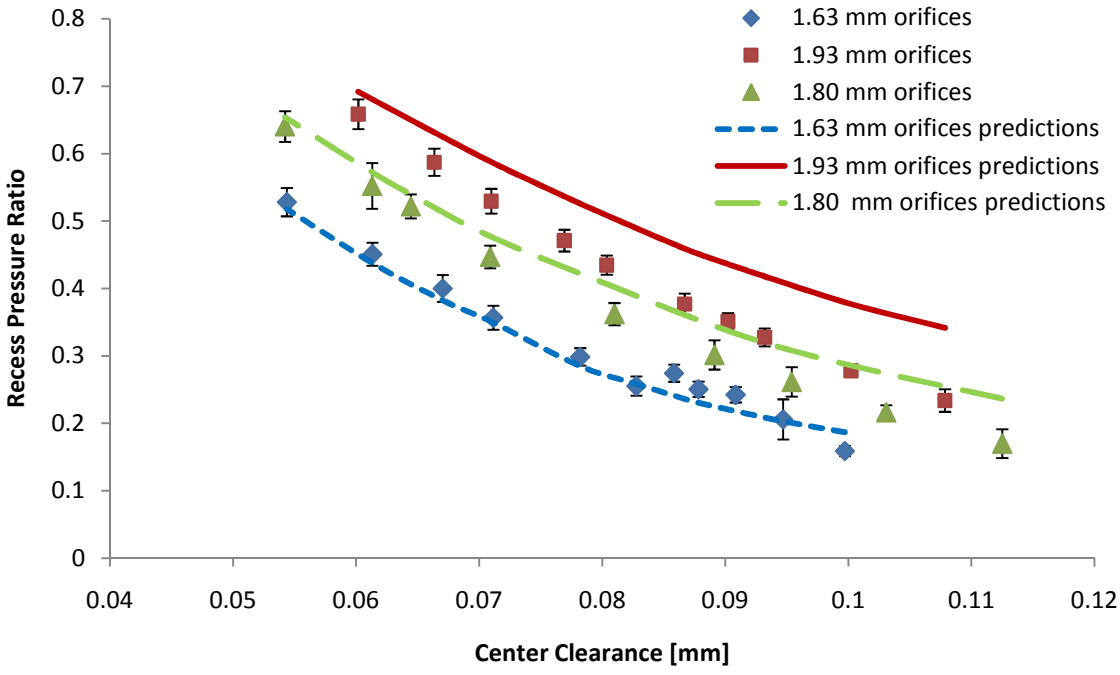

Figure F - 6: Measured and predicted [3] recess pressure ratio versus clearance at 10.34 bar supply and 7.5 krpm

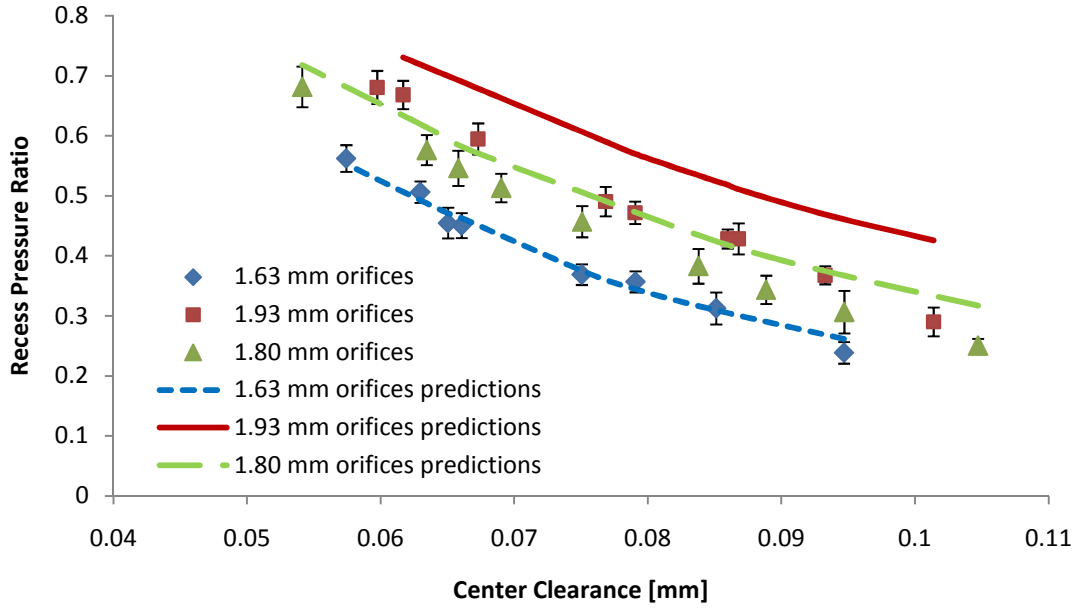

Figure F - 7: Measured and predicted [3] recess pressure ratio versus clearance at 10.34 bar supply and 12.5 krpm

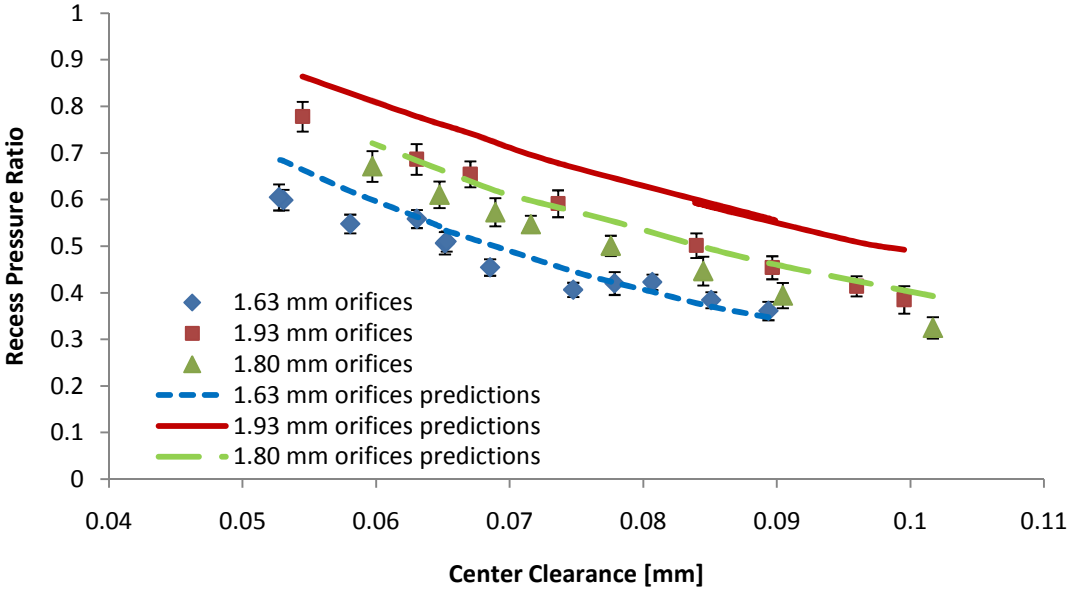

Figure F - 8: Measured and predicted [3] recess pressure ratio versus clearance at 10.34 bar supply and 17.5 krpm

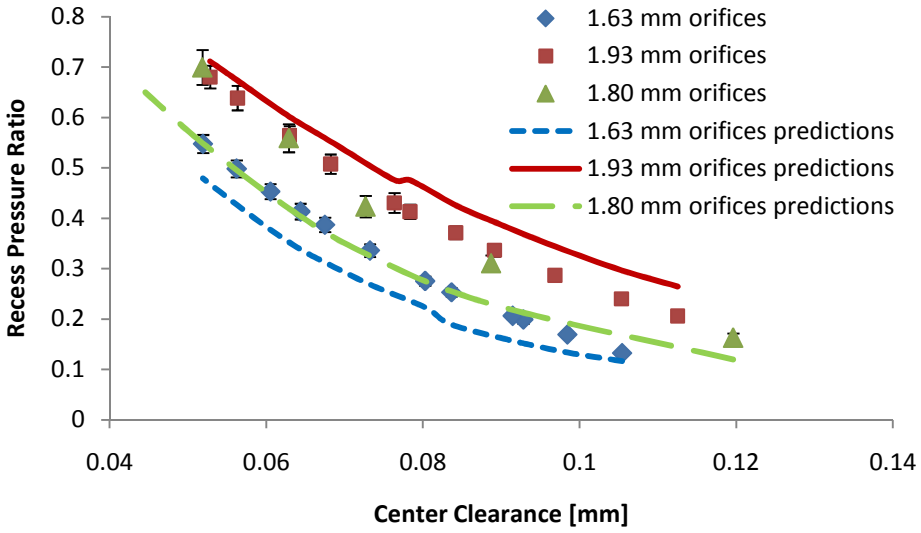

Figure F - 9: Measured and predicted [3] recess pressure ratio versus clearance at 17.24 bar supply and 0 rpm

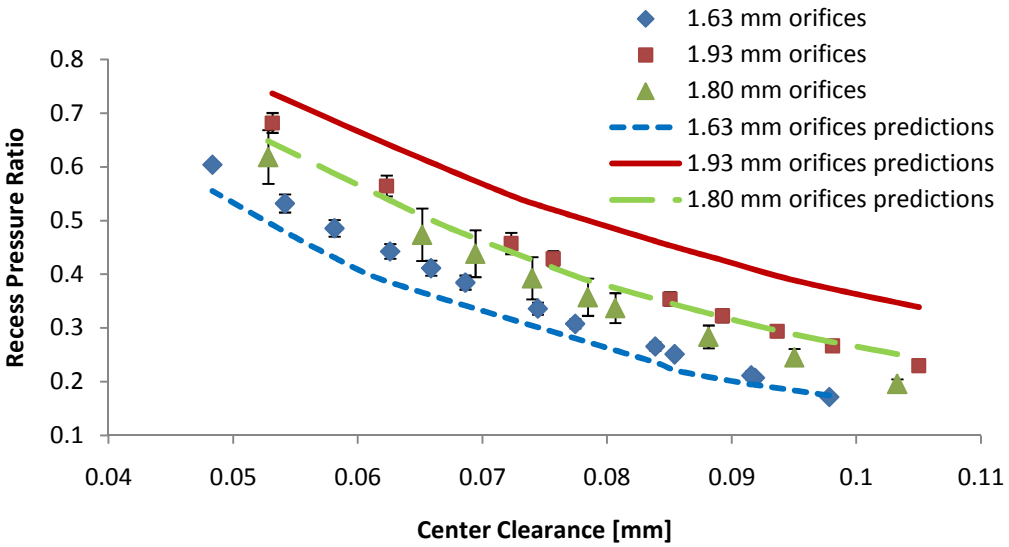

Figure F - 10: Measured and predicted [3] recess pressure ratio versus clearance at 17.24 bar supply and 7.5 krpm

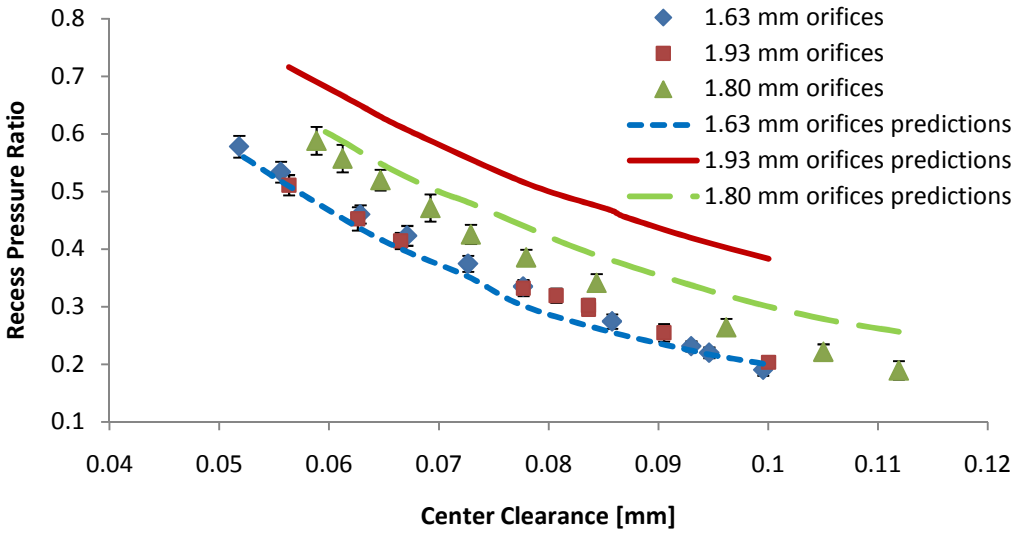

Figure F - 11: Measured and predicted [3] recess pressure ratio versus clearance at 17.24 bar supply and 12.5 krpm

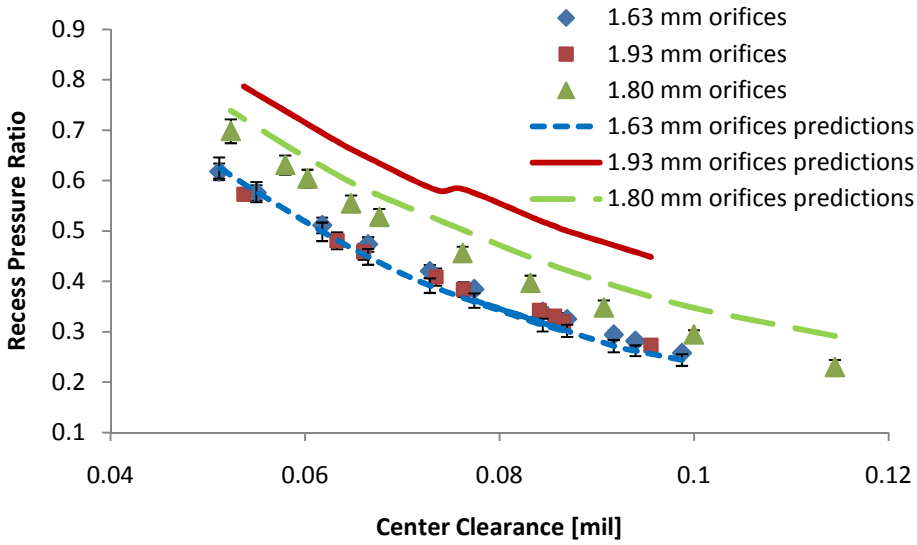

Figure F - 12: Measured and predicted [3] recess pressure ratio versus clearance at 17.24 bar supply and 17.5 krpm

APPENDIX G

INNER RADIUS EXHAUST FLOW RATE FIGURES

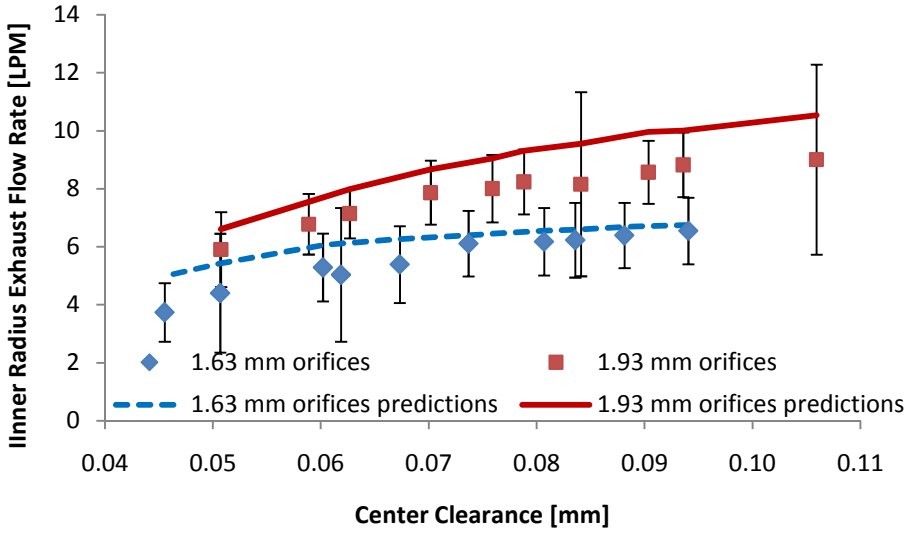

Figure G - 1: Measured and predicted [3] inner radius exhaust flow rate versus center clearance at 5.17 bar and 0 rpm

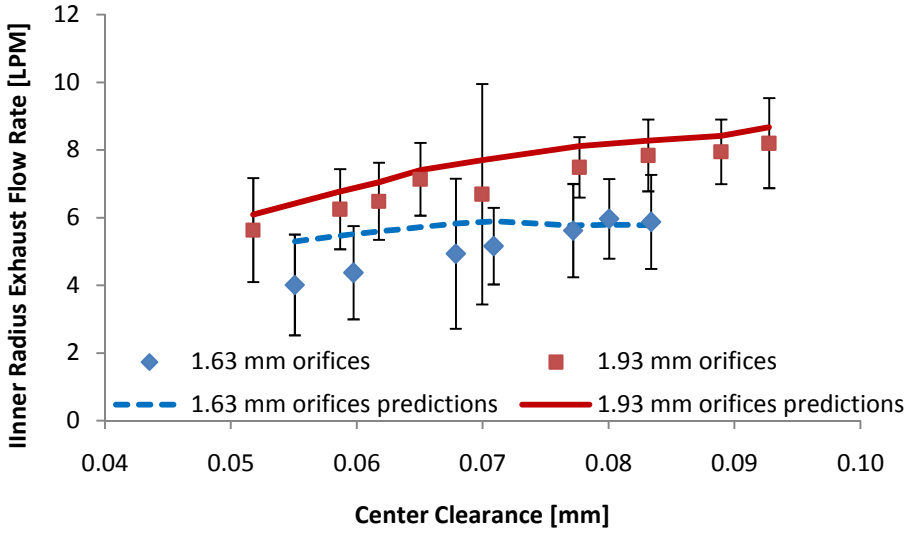

Figure G - 2: Measured and predicted [3] inner radius exhaust flow rate versus center clearance at 5.17 bar and 7.5 krpm

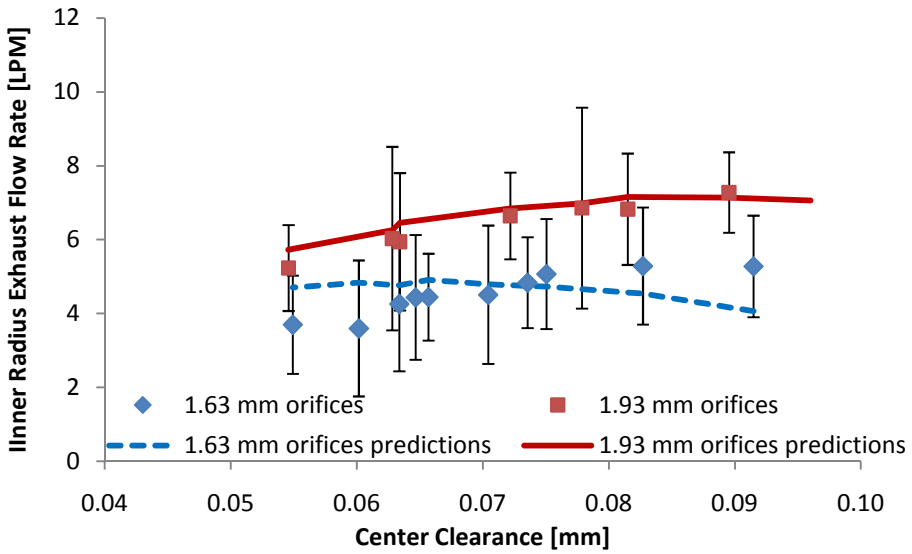

Figure G - 3: Measured and predicted [3] inner radius exhaust flow rate versus center clearance at 5.17 bar and 12.5 krpm

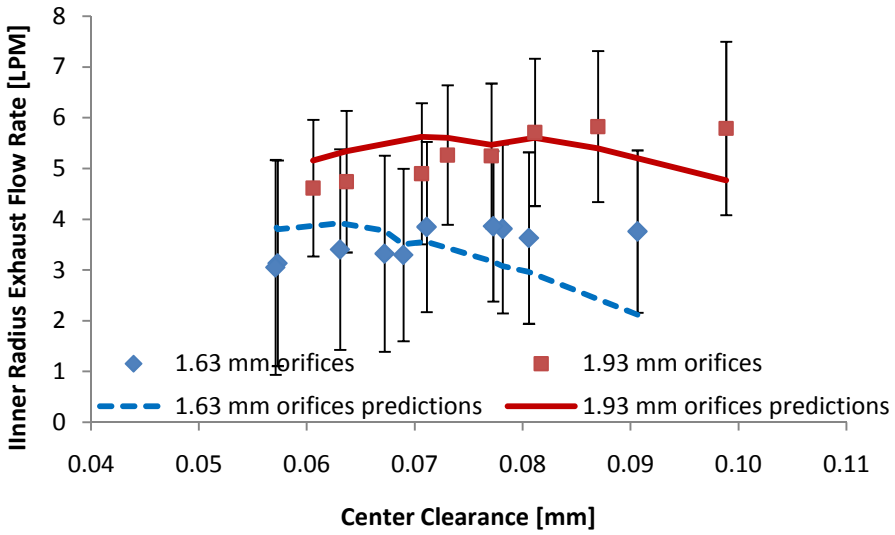

Figure G - 4: Measured and predicted [3] inner radius exhaust flow rate versus center clearance at 5.17 bar and 17.5 krpm

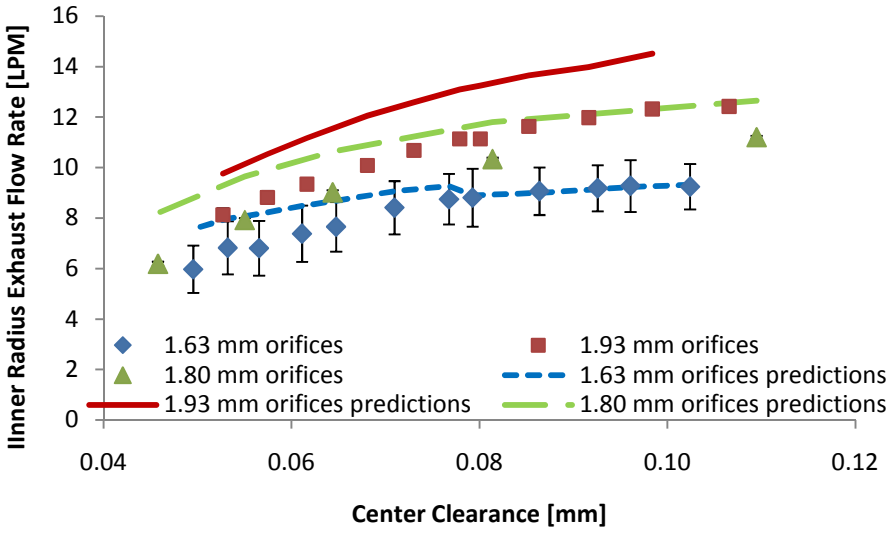

Figure G - 5: Measured and predicted [3] inner radius exhaust flow rate versus center clearance at 10.34 bar and 0 rpm

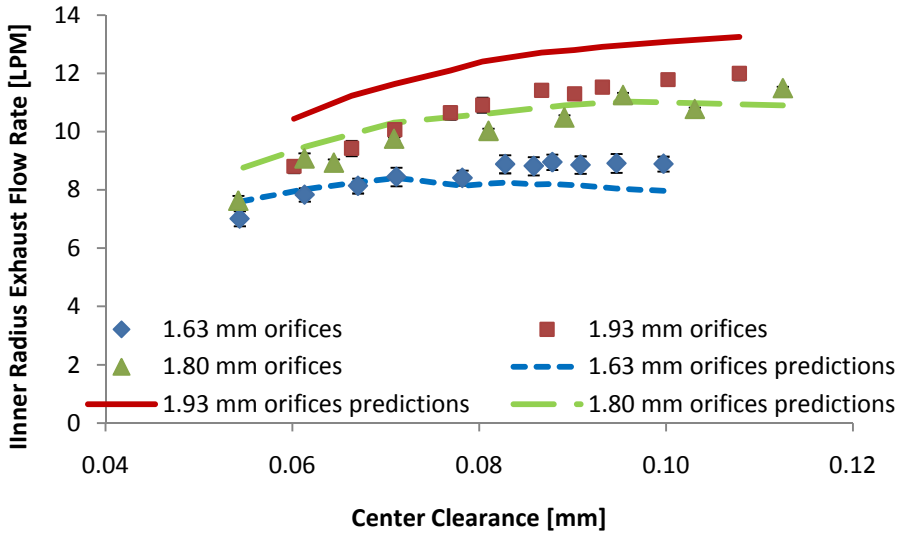

Figure G - 6: Measured and predicted [3] inner radius exhaust flow rate versus center clearance at 10.34 bar and 7.5 krpm

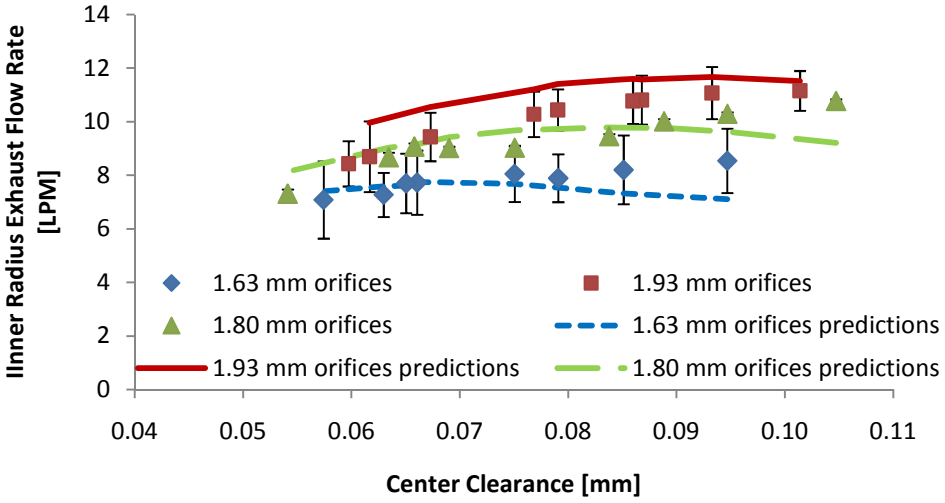

Figure G - 7: Measured and predicted [3] inner radius exhaust flow rate versus center clearance at 10.34 bar and 12.5 krpm

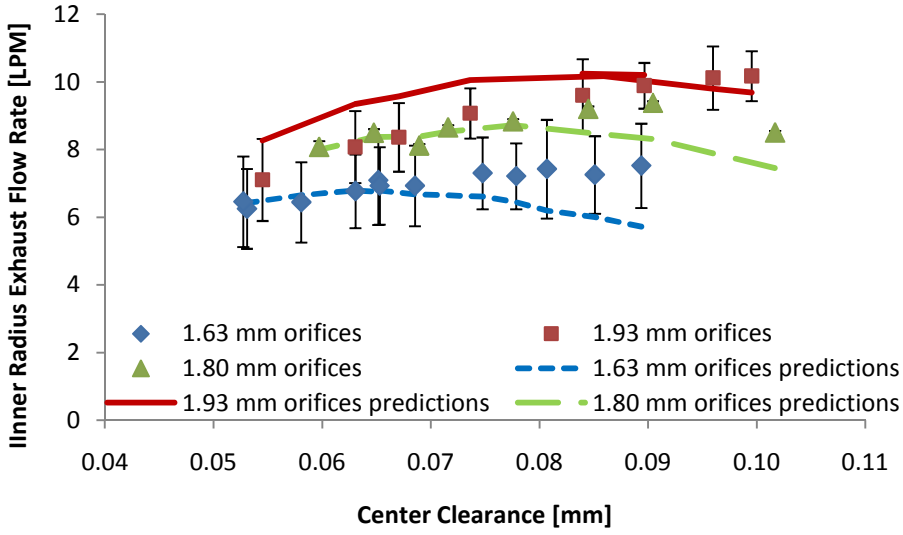

Figure G - 8: Measured and predicted [3] inner radius exhaust flow rate versus center clearance at 10.34 bar and 17.5 krpm

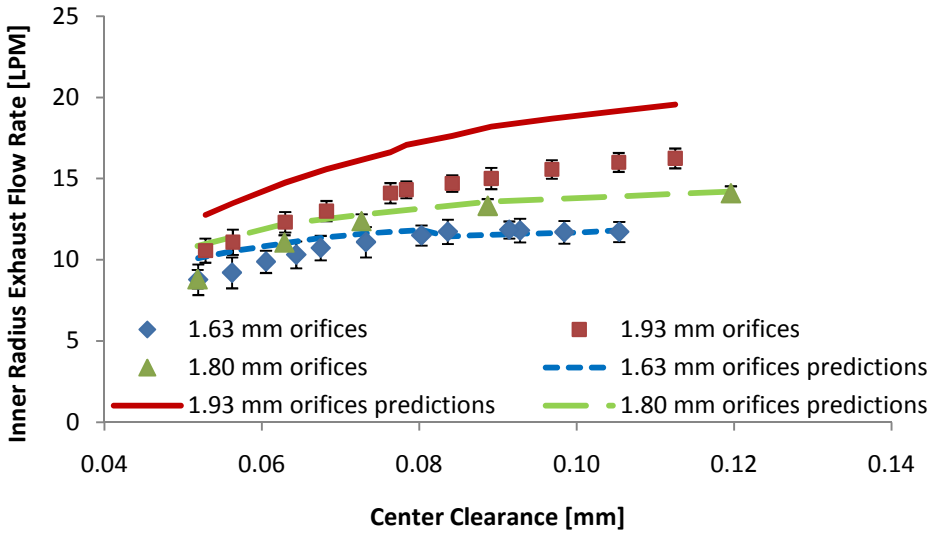

Figure G - 9: Measured and predicted [3] inner radius exhaust flow rate versus center clearance at 17.24 bar and 0 rpm

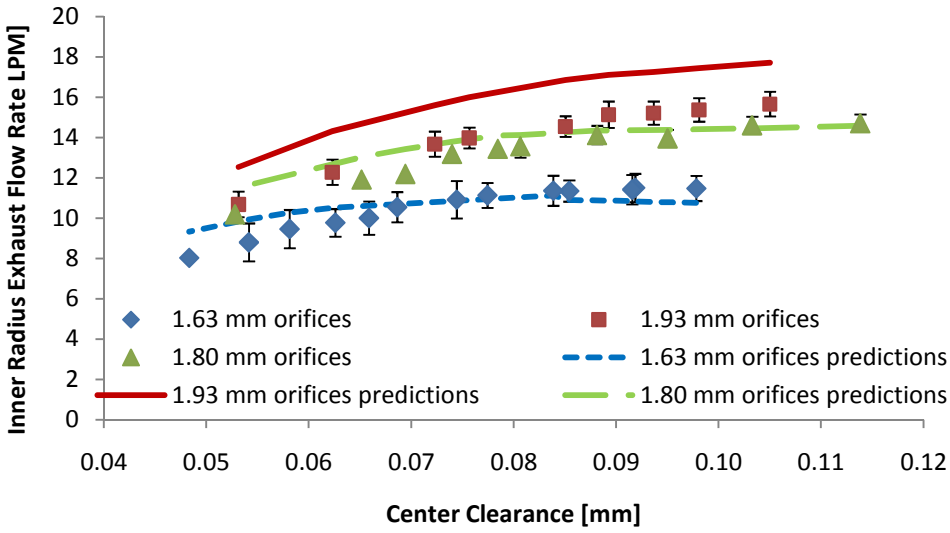

Figure G - 10: Measured and predicted [3] inner radius exhaust flow rate versus center clearance at 17.24 bar and 7.5 krpm

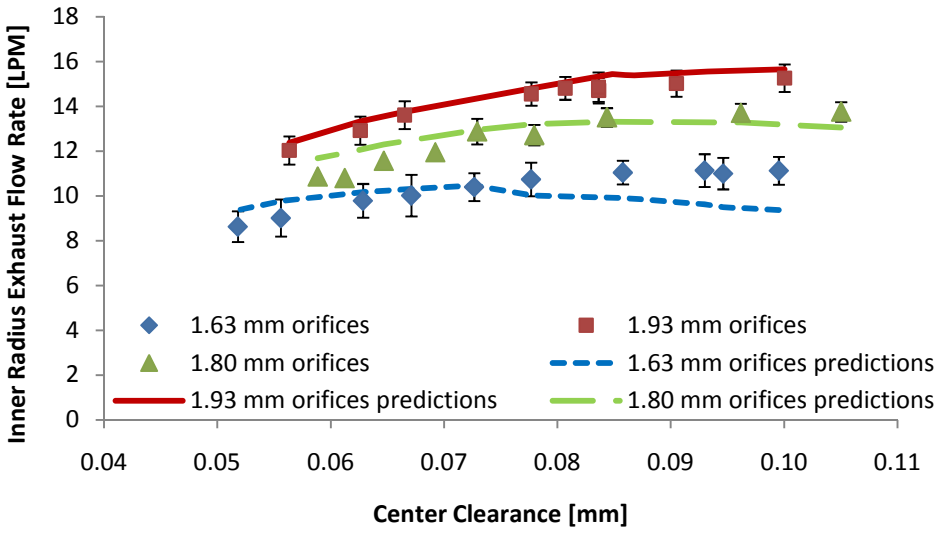

Figure G - 11: Measured and predicted [3] inner radius exhaust flow rate versus center clearance at 17.24 bar and 12.5 krpm

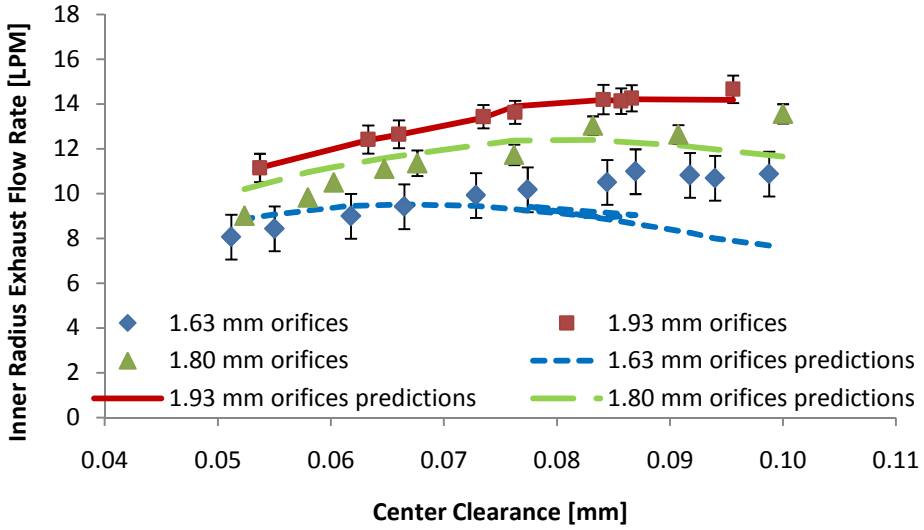

Figure G - 12: Measured and predicted [3] inner radius exhaust flow rate versus center clearance at 17.24 bar and 17.5 krpm

APPENDIX H

CENTER CLEARANCE FIGURES

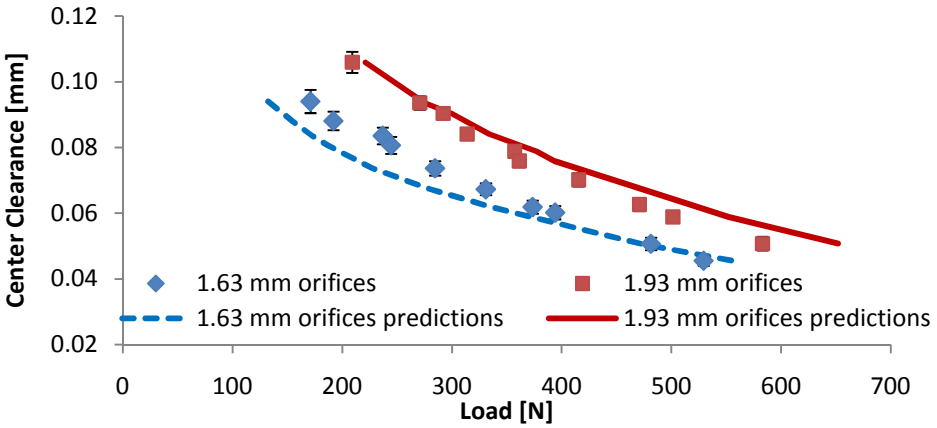

Figure H - 1: Measured and predicted [3] center clearance versus load at 5.17 bar supply and 0 rpm

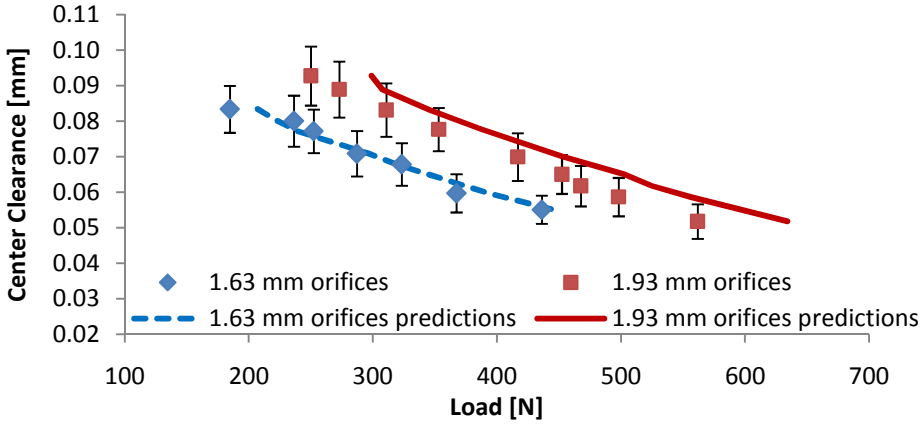

Figure H - 2: Measured and predicted [3] center clearance versus load at 5.17 bar supply and 7.5 krpm

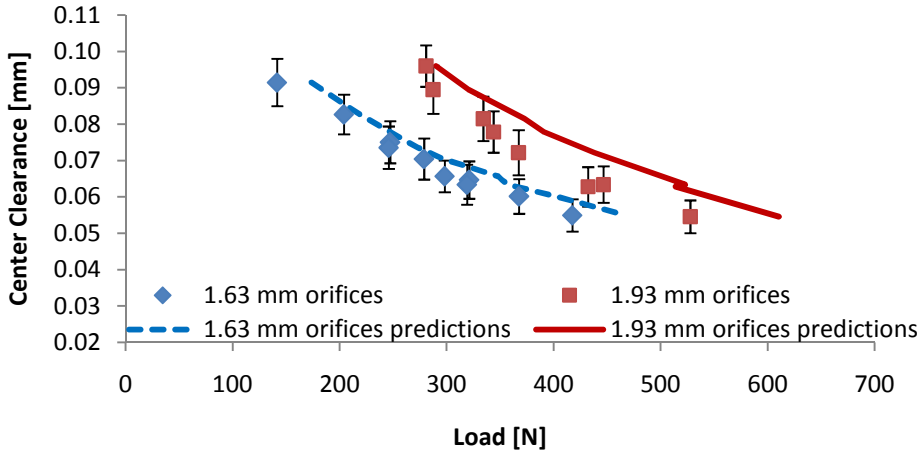

Figure H - 3: Measured and predicted [3] center clearance versus load at 5.17 bar supply and 12.5 krpm

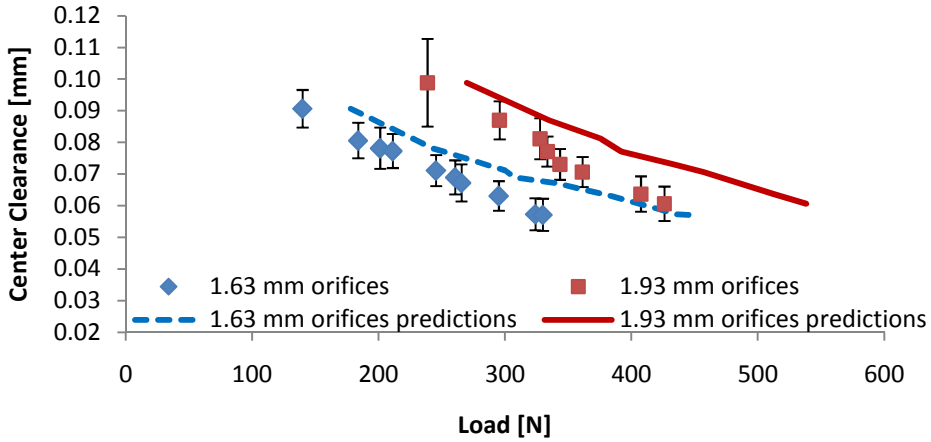

Figure H - 4: Measured and predicted [3] center clearance versus load at 5.17 bar supply and 17.5 krpm

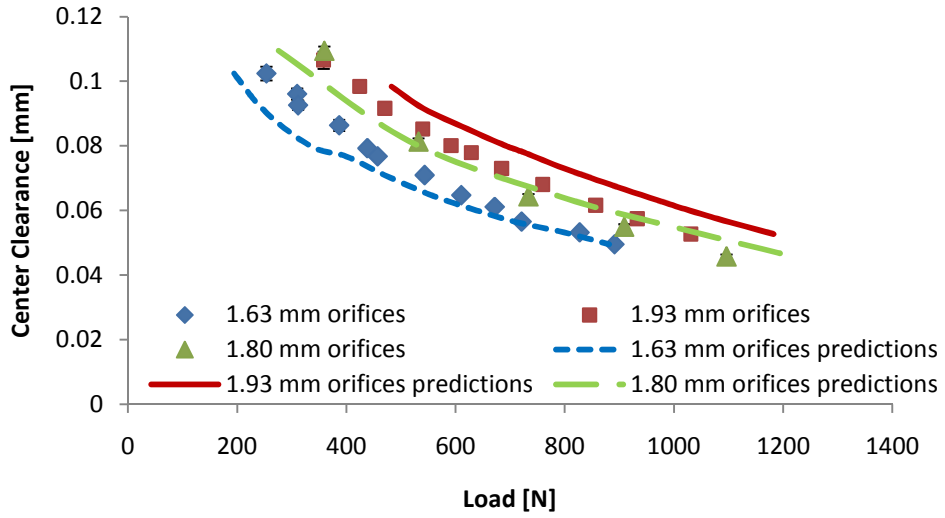

Figure H - 5: Measured and predicted [3] center clearance versus load at 10.34 bar supply and 0 rpm

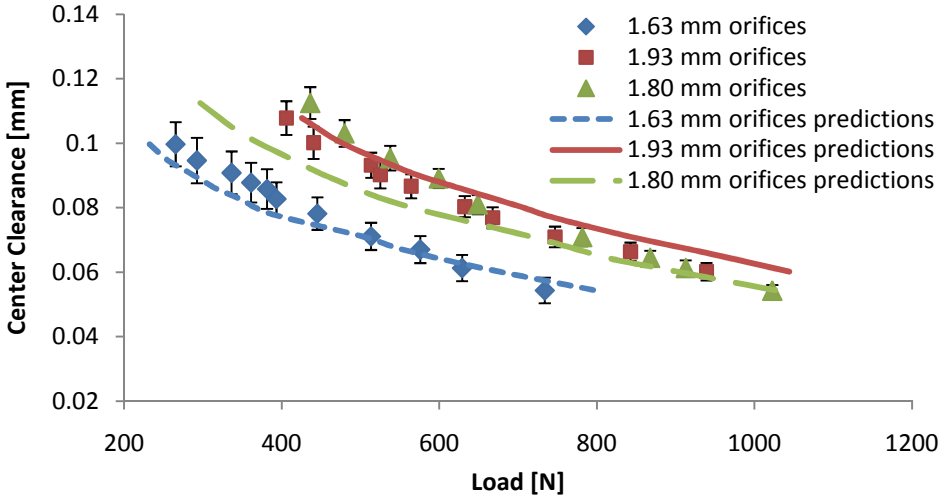

Figure H - 6: Measured and predicted [3] center clearance versus load at 10.34 bar supply and 7.5 krpm

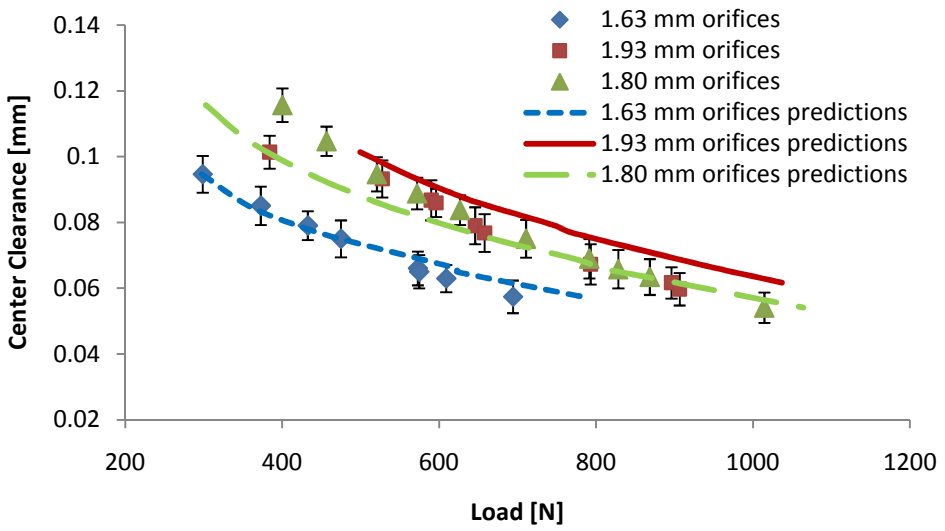

Figure H - 7: Measured and predicted [3] center clearance versus load at 10.34 bar supply and 12.5 krpm

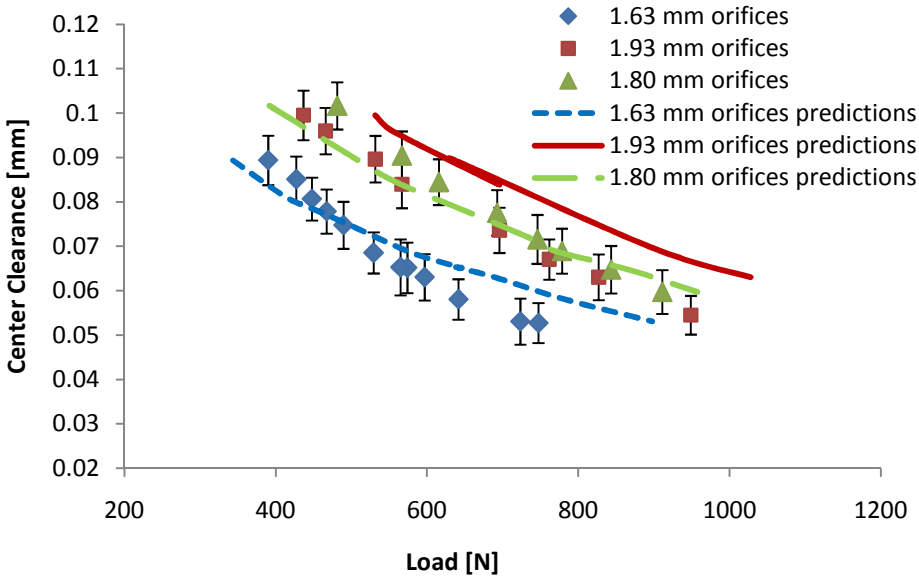

Figure H - 8: Measured and predicted [3] center clearance versus load at 10.34 bar supply and 17.5 krpm

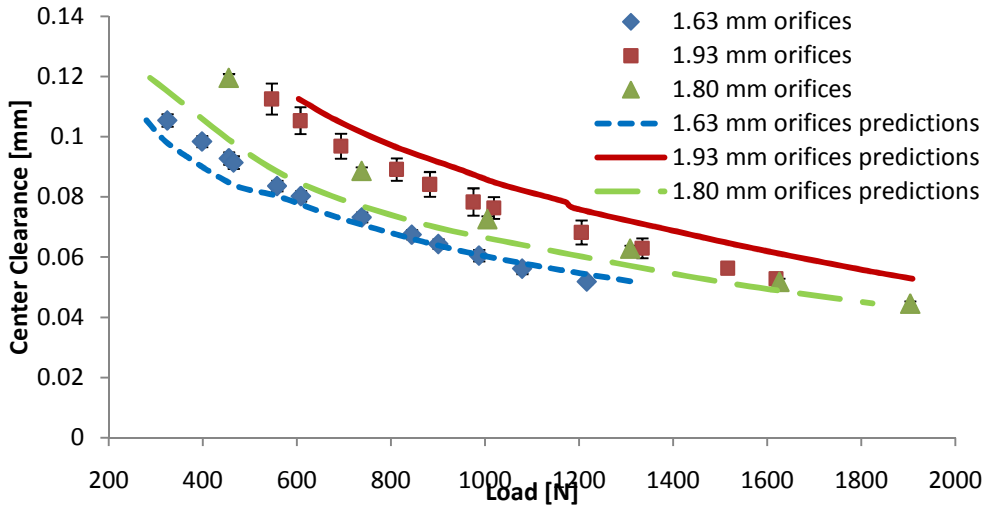

Figure H - 9: Measured and predicted [3] center clearance versus load at 17.24bar supply and 0 rpm

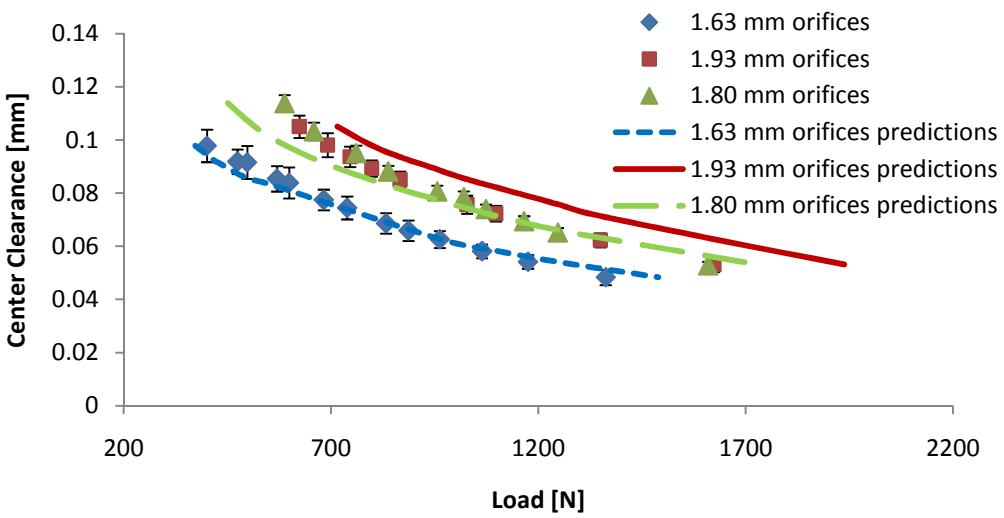

Figure H - 10: Measured and predicted [3] center clearance versus load at 17.24bar supply and 7.5 krpm

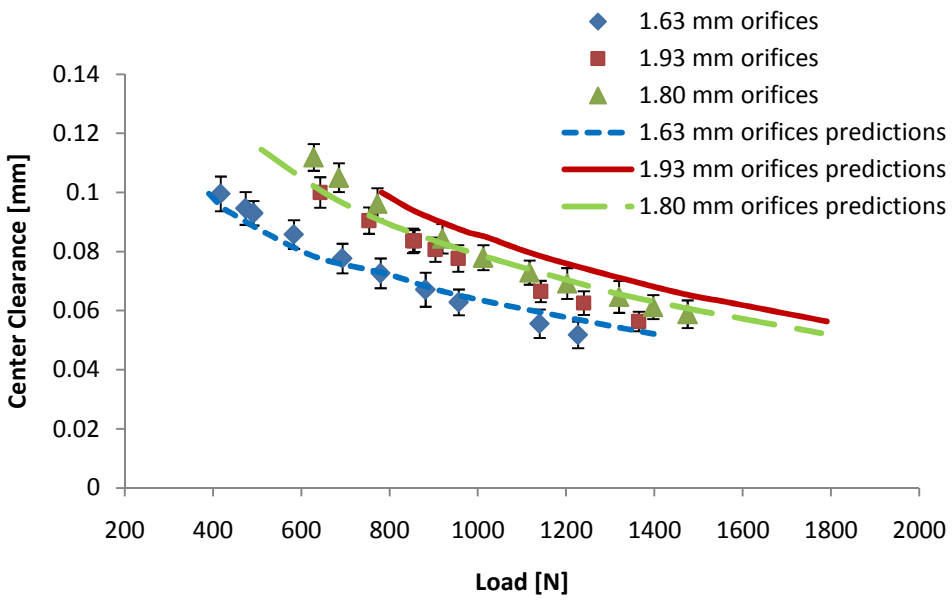

Figure H - 11: Measured and predicted [3] center clearance versus load at 17.24bar supply and 12.5 krpm

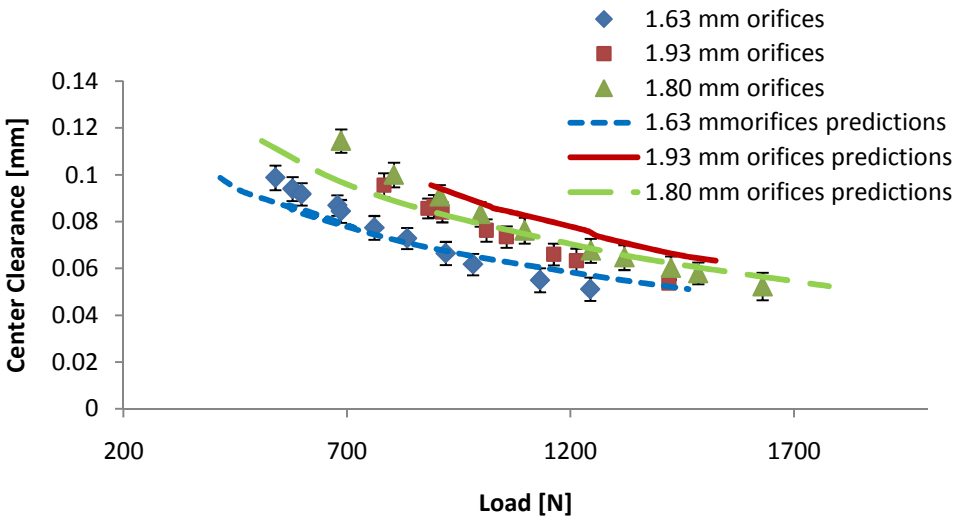

Figure H - 12: Measured and predicted [3] center clearance versus load at 17.24bar supply and 12.5 krpm

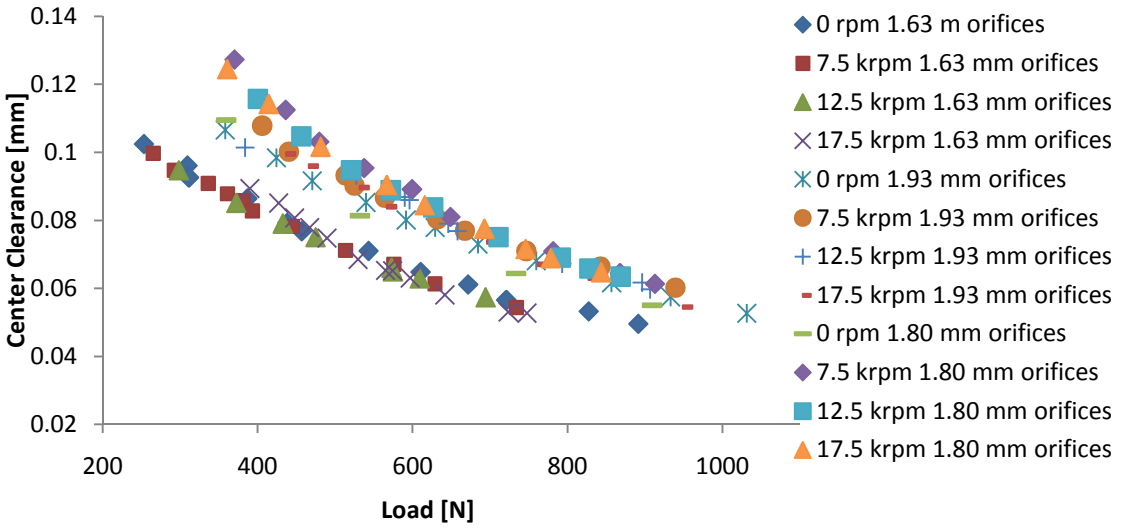

Figure H - 13: Center clearance versus load at 10.34 bar supply and all speeds for all three orifice diameters

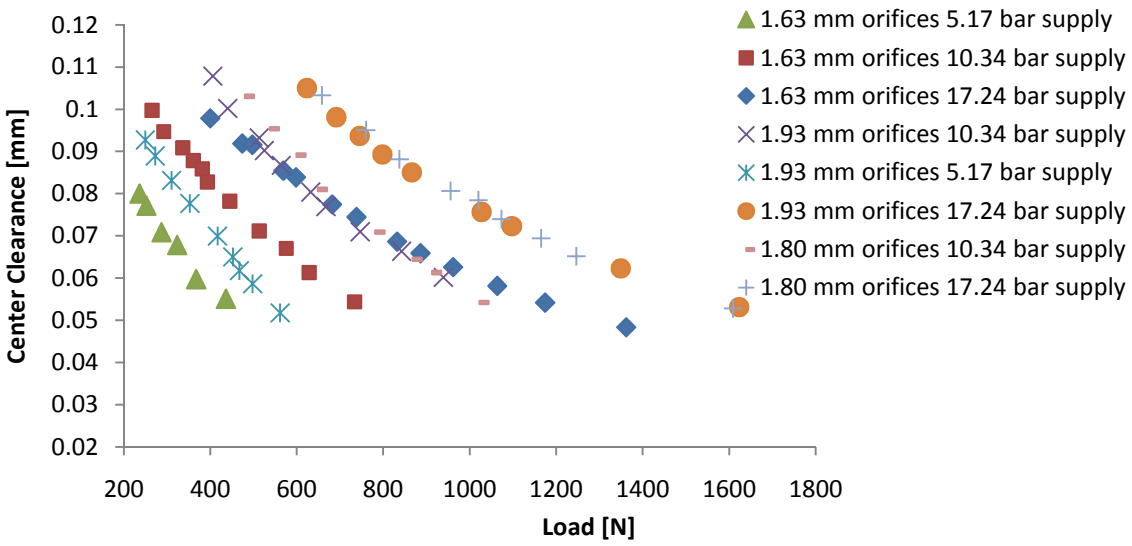

Figure H - 14: Center Clearance versus load at 7.5 krpm and all supply pressures for all three orifice diameters

APPENDIX I

ESTIMATED AXIAL STIFFNESS FIGURES

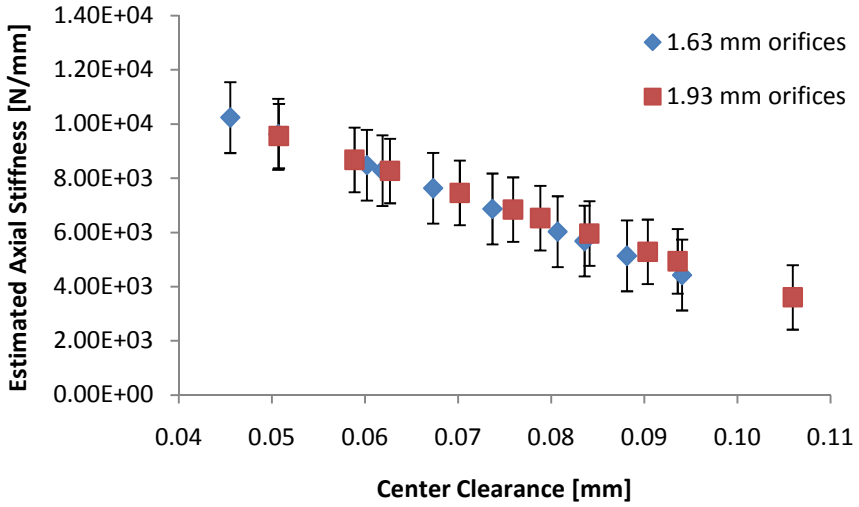

Figure I - 1: Estimated axial stiffness versus clearance at 5.17 bar and 0 rpm

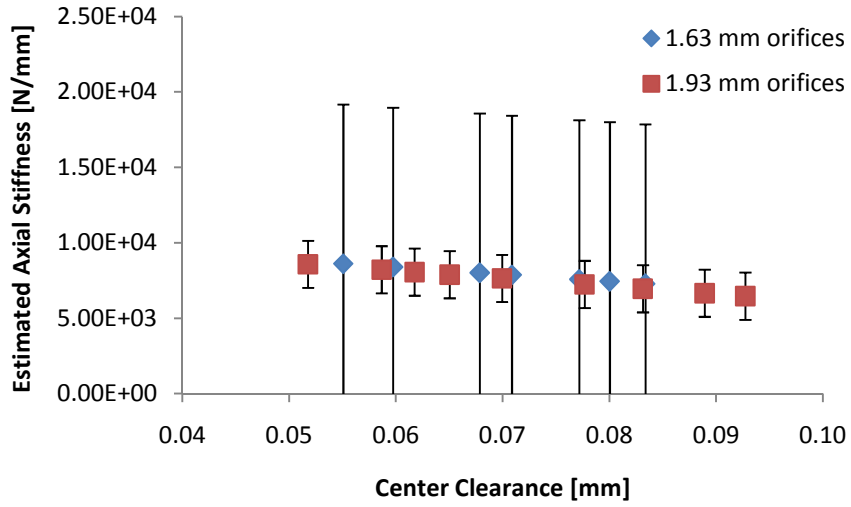

Figure I - 2: Estimated axial stiffness versus clearance at 5.17 bar and 7.5 krpm

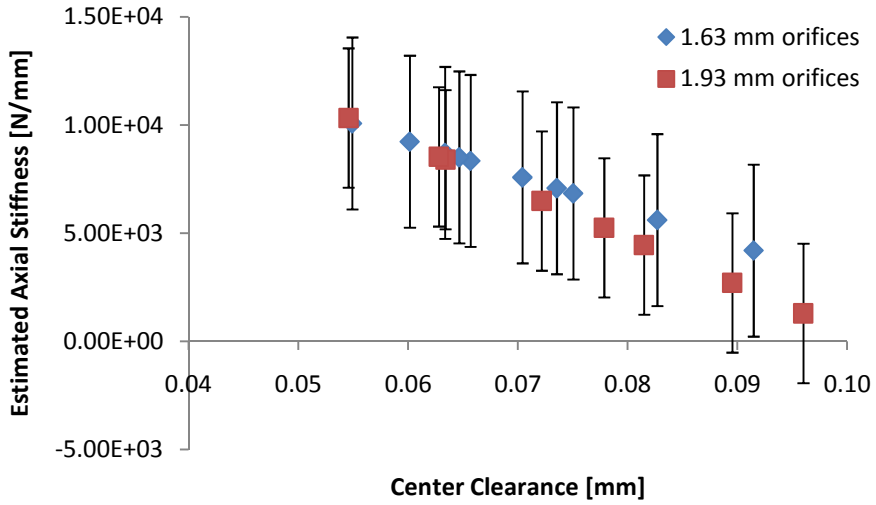

Figure I - 3: Estimated axial stiffness versus clearance at 5.17 bar and 12.5 krpm

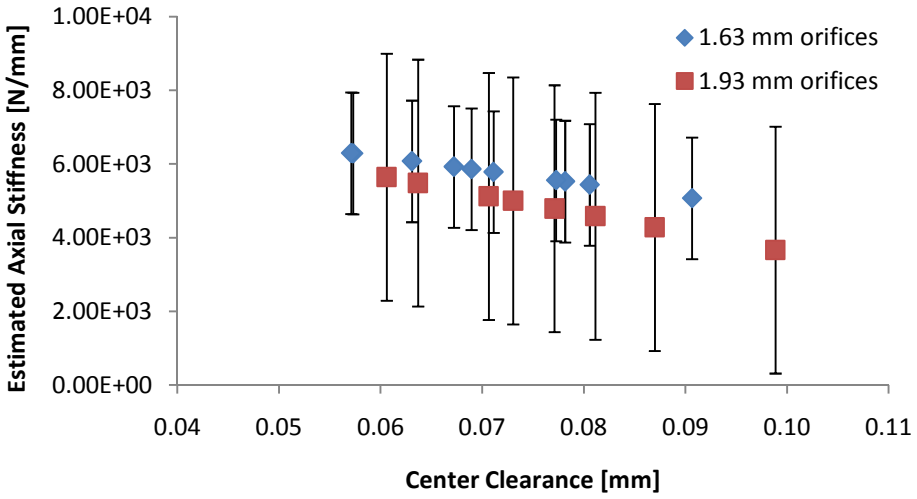

Figure I - 4: Estimated axial stiffness versus clearance at 5.17 bar and 17.5 krpm

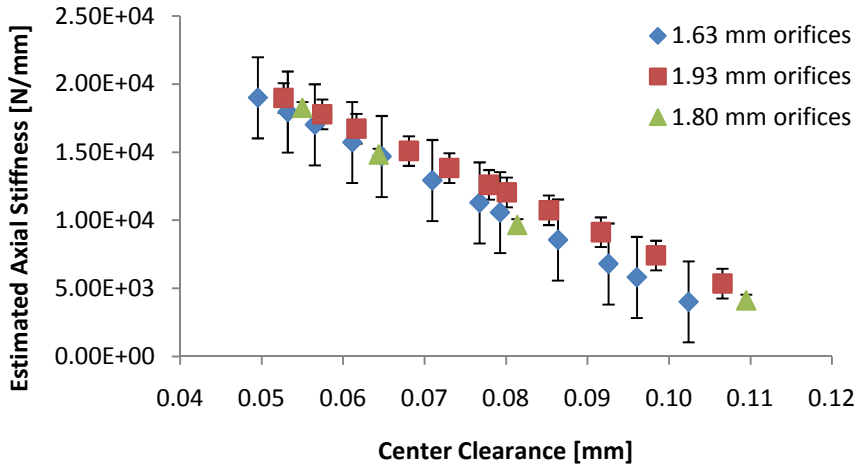

Figure I - 5: Estimated axial stiffness versus clearance at 10.34 bar and 0 rpm

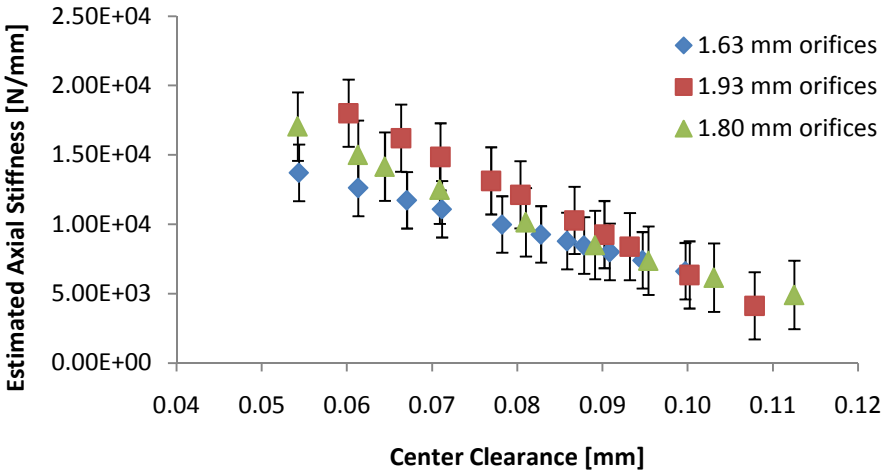

Figure I - 6: Estimated axial stiffness versus clearance at 10.34 bar and 7.5 krpm

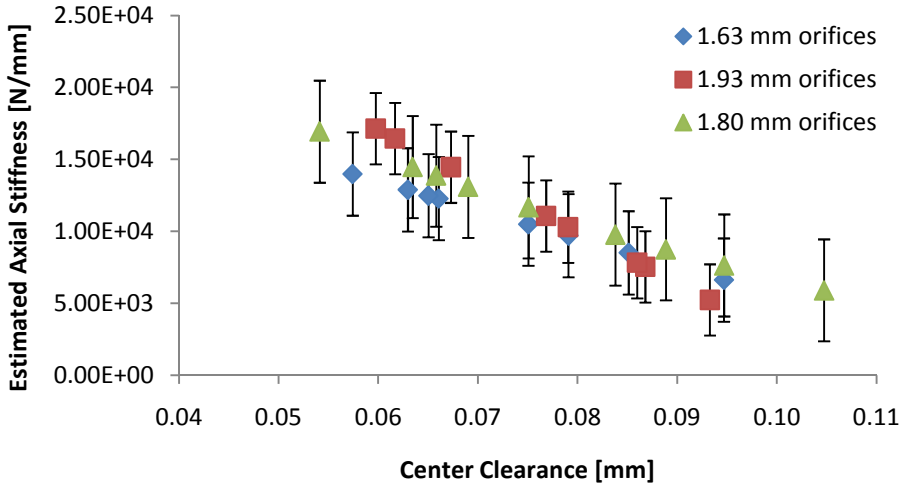

Figure I - 7: Estimated axial stiffness versus clearance at 10.34 bar and 12.5 krpm

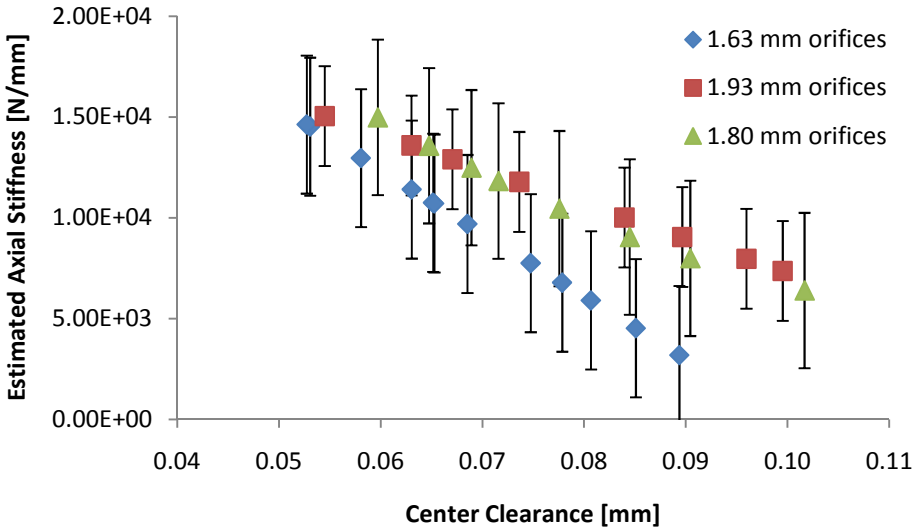

Figure I - 8: Estimated axial stiffness versus clearance at 10.34 bar and 17.5 krpm

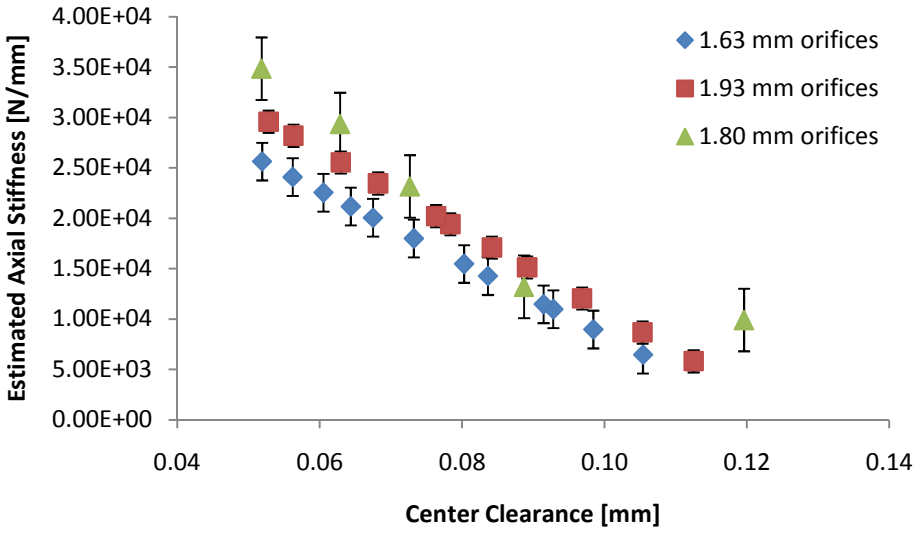

Figure I - 9: Estimated axial stiffness versus clearance at 17.24 bar and 0 rpm

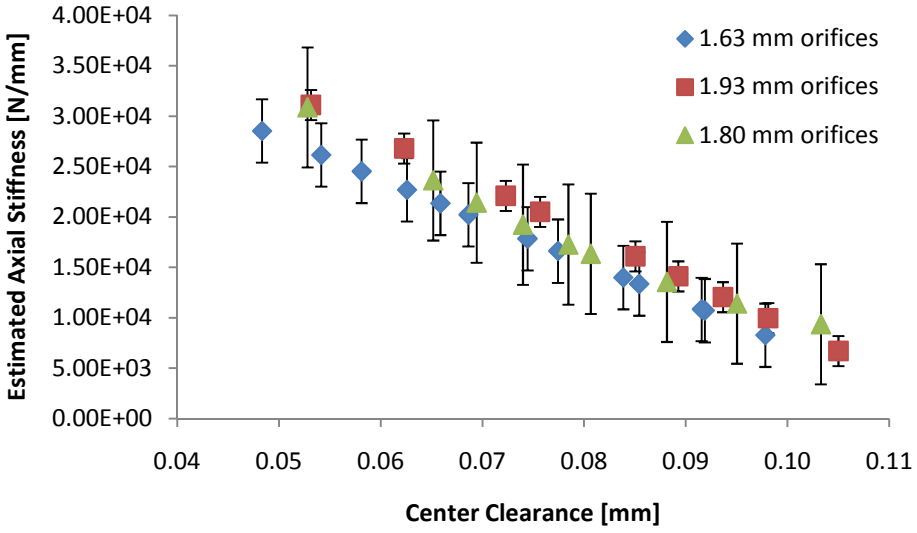

Figure I - 10: Estimated axial stiffness versus clearance at 17.24 bar and 7.5 krpm

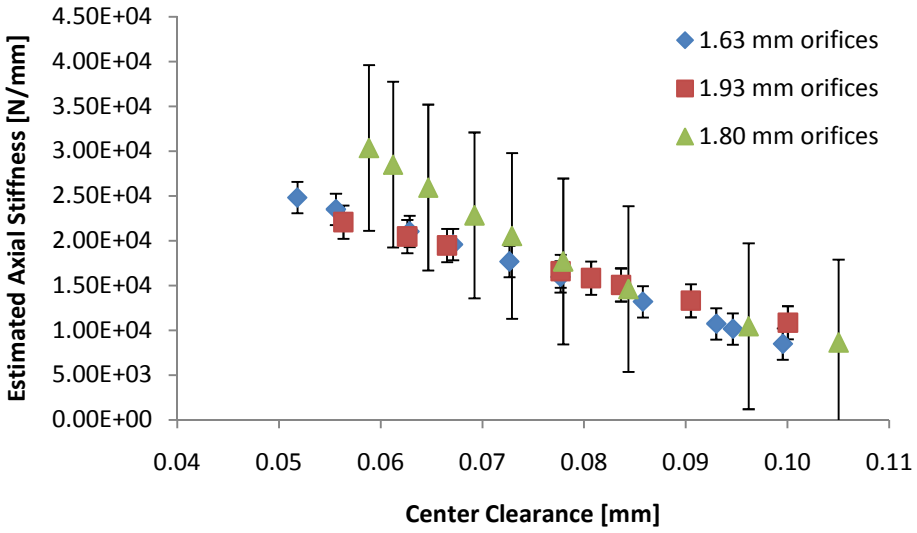

Figure I - 11: Estimated axial stiffness versus clearance at 17.24 bar and 12.5 krpm

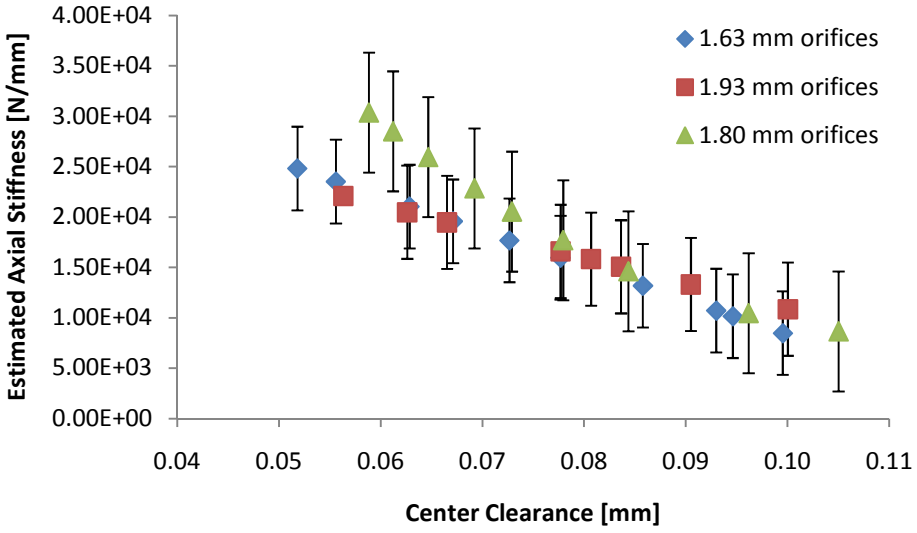

Figure I - 12: Estimated axial stiffness versus clearance at 17.24 bar and 17.5 krpm

VITA

Name: Paul Robert Esser

Address: 7045 Killarney,
Beaumont, TX 77706

Email Address: paul.r.esser@gmail.com

Education: B.S., Engineering – Mechanical Engineering, Texas Christian University, 2006
M.S., Mechanical Engineering, Texas A&M University, 2010